UNIVERSITÀ DEGLI STUDI DI PADOVA

Dipartimento di Fisica e Astronomia “Galileo Galilei”

Master Degree in Astrophysics and Cosmology

Final Dissertation

Initiation mechanisms of the erupting prominences

Thesis supervisor Prof./Dr.
Giovanni Carraro
Thesis co-supervisor Prof./Dr.
Marilena Mierla

Candidate
Letizia Casara

Academic Year 2022/2023

Abstract

Solar prominences are common features of the solar atmosphere. They exhibit unique characteristics that set them apart from the surrounding hot corona, where they are often observed. With temperatures and densities one hundred times cooler and denser than the coronal material, they appear as bright structures at the edge of the sun (above the limb) when observed in the optical or in the extreme ultraviolet (EUV) spectral lines. On the solar disk, they take on a darker appearance, referred to as filaments. These prominences are plasma formations embedded within a magnetic environment above magnetic inversion lines, known as filament channels.

The main aim of this thesis is to provide a comprehensive understanding of these remarkable structures. It begins by introducing the internal structure of the sun, emphasizing the crucial role of its magnetic field and the solar atmosphere where prominences can either remain stable or contribute to large-scale dynamic events such as flares and coronal mass ejections (CMEs). These powerful eruptions can disrupt the interplanetary medium and trigger geomagnetic storms on Earth, impacting both ground-based technology and the space environment. Over the past decade, Space Weather has emerged as a scientific discipline dedicated to predicting solar activity and its effects on our planet. Accurate predictions hinge on identifying systematic precursors, such as instabilities in the filament-channel magnetic field, that signals impending solar eruptions.

This thesis focuses on the observation of solar prominence eruptions and seeks to unravel their initial triggering mechanisms. The study utilizes observations obtained from the He II 304 Å passband of the Full Sun Imager (FSI) telescope aboard the Solar Orbiter during the period between 2021 and 2022. Additionally, the FSI 174 channel was visually consulted to get complementary information. The FSI is an integral component of the Extreme Ultraviolet Imager (EUI) instrument, which comprises two high-resolution imagers (HRIs) along with the FSI, a single mirror telescope boasting a wide field of view and high angular resolution. This advanced instrumentation allows for the capture of unprecedented solar images in two different passbands. Furthermore, images from other instruments were utilized to extract additional information about the solar corona, such as the Atmospheric Imaging Assembly (AIA) instrument onboard the Solar Dynamics Observatory (SDO).

Prominence eruptions undergo three distinct phases: a slow rise phase characterized by a constant velocity, an acceleration phase where the feature begins to speed up, and a propagation phase in which the prominence maintains a constant velocity (differing from the slow rise phase). The study of the early rise and propagation phases of eruptions can provide important information about the forces that impact prominences and their acceleration behaviour as a function of height. To accomplish this, six events with diverse morphologies were selected for analysis. Thanks to the large field of view of the FSI channel, we could observe these events at a high cadence and track them at high altitudes.

Building on the previous work of M. Mierla et al., 2013 [74], the outer edge of the prominence structures were fitted with power-law polynomial functions to extract the best-fitting models characterizing their behavior and to determine the initial time at which the prominences began to accelerate. In addition, exponential and parabolic profiles were investigated as alternative scenarios. The obtained results were highly dependent on the chosen initial time and the specific event under investigation. The majority of the events exhibited a parabolic growth pattern, indicative of a breakout model, while others were inconsistent with the models present in literature. In certain cases, no acceleration was observed, suggesting the involvement of multiple triggering mechanisms rather than a single unified model to fully describe these features.

Contents

Introduction

> *Protubérances: "Ces amas de matière lumineuse ayant une grande vivacité et possédant une activité photogénique très remarquable"*
> *(A. Secchi "Le Soleil", 1877, I. 385 [109])*

The interest in solar prominences traces its roots back to the past, a time when advanced instruments for direct observation of these structures did not exist.
It is believed that the earliest recorded observations of such phenomena can be traced back to as early as 1239 during a solar eclipse, when an unusual "burning hole" was documented in the solar corona [115]. Over time, observations of these phenomena increased, often described as "burning holes" or "red flames", and occasionally misidentified as lunar mountains [125]. The oldest depictions of these observations consist of drawings and paintings, as illustrated in the Figure 1 depicting a solar eclipse in 1842 by a French artist.

Figure 1: Engraving created by Eugene Bouvard during the solar eclipse of 1842 in Digne, France (courtesy of S. Koutchmy). Image adapted from Solar Prominence by Jean-Claude Vial Oddbjørn Engvold [125].

Despite significant advancements in both observational tools and the understanding of these phenomena over the years, many mysteries remain unanswered. As pointed out by Parenti in 2014 [85], contemporary research on solar prominences is driven by numerous unresolved inquiries.

- *Support and Stability*: A particularly captivating aspect of quiescent prominences is their mysterious equilibrium, enabling them to retain mass within the delicate solar corona. Although the magnetic field's pivotal role is well-established, comprehensive observational data are still lacking to pinpoint the specific mechanisms and magnetic configurations responsible for their stability.
- *Mass Movements*: Movements of mass within prominences have the potential to influence their equilibrium, mass maintenance, and replenishment. It's noteworthy that only a handful of models incorporate such observed dynamics.
- *Radiative Losses*: Solar radiation from the surrounding environment has a significant impact on the physical conditions of prominences. Grasping the intricacies of radiative transfer within partially-ionized prominence plasma is essential for constraining radiative losses. During quiescent periods, prominence radiation remains consistent, necessitating an undiscovered heating source to maintain energy equilibrium within the structure.

- *Magnetic Field*: The limited availability of extensive magnetic field measurements within prominences constrains our comprehension of coronal magnetic field physics and its interactions with plasma.

- *Formation and Disappearance*: Prominences can exhibit prolonged stability but may also participate in large-scale dynamic occurrences like flares and Coronal Mass Ejections (CMEs). These substantial eruptions disturb the interplanetary environment and can lead to geomagnetic storms on Earth. Given our modern technology-dependent way of life, solar activity presents a notable concern, particularly for satellites employed in telecommunications and human space endeavors. Over the past decade, the field of *Space Weather* has emerged as a scientific discipline focused on predicting solar activity and its consequences on Earth. Accurately forecasting solar eruptions is of utmost importance, and phenomena such as instabilities in filament-channel magnetic fields may serve as reliable precursors.

This work specifically aims to provide insights into the latter aspect. Eruptive prominences are intricately linked with CMEs, and the mechanisms responsible for triggering these eruptive events are believed to be interconnected. These processes can be attributed primarily to two mechanisms: magnetic reconnection and Magnetohydrodynamic (MHD) instability. However, the precise mechanisms involved remain a topic of ongoing debate. A deeper understanding of these phenomena has the potential to enhance our predictive capabilities and characterization, ultimately improving our ability to mitigate their impacts.

Eruptive prominences and CMEs follow a distinct three-phase kinematic pattern, comprising a gradual ascent at a constant velocity (referred to as the "*slow rise*" phase), a period of acceleration (known as the "*acceleration phase*"), and subsequent deceleration or the maintenance of a constant velocity (referred to as the "*propagation phase*"). The initial stages of this profile, encompassing the slow rise and acceleration, are of particular interest due to their potential to offer valuable insights into the initiation mechanisms of CMEs. As elucidated by Mierla et al. in 2013 [74], utilizing a power-law polynomial to fit the height-time diagram of tracked features in the solar corona and comparing the results with various numerical simulations can provide valuable insights into the mechanisms responsible for destabilization.

Several studies have attempted to accomplish this by employing various mathematical functions to interpolate the curvature in the kinematic profile. For example, Mierla et al., 2013 [74] have used a power-law with five degrees of freedom spanning the entire early phase, whereas Schrijver et al., 2008 [105] have utilized power-law and exponential functions during the acceleration phase. Drawing inspiration from Mierla's work and building upon Schrijver's research, I conducted height measurements for six eruptive prominences using FSI 304 data. Subsequently, I applied various curve-fitting functions to analyze the early phase of the eruption, including a power-law, parabolic, and exponential fits, to the resulting height-time plots. The objective was to extract the onset of the acceleration phase, the most suitable fit parameters and gain a deeper understanding of the initiation mechanisms associated with these phenomena.

Outline of the thesis This thesis comprises four chapters. Chapter 1 provides an introduction to the Sun's characteristics, with a specific focus on solar prominences and the existing literature on models that seek to explain their eruption mechanisms. Chapter 2 delves into the instrumentation used, highlighting the FSI and briefly touching on AIA. It also covers the data's key characteristics and introduces the tools employed for the analysis. Chapter 3 delineates the chosen events for analysis and describes the applied analysis methodology in detail. Chapter 4 presents the results obtained for each event. The last chapter summarizes the conclusions drawn from the present study.

Chapter 1

The Sun and the Solar Prominences

In the upcoming chapter, I will present some fundamental concepts that will enhance our comprehension of the research and the driving factors behind its investigation. Section 1.1 will delve into the structure of the Sun, encompassing its innermost regions all the way to its outermost layers, collectively known as the Sun's atmosphere. In contrast, Section 1.2 will focus on the Sun's magnetic field. It will explore its proposed origins, properties within the solar atmosphere, its connection to key phenomena, and its role in solar activity.
Section 1.3 will be dedicated to the introduction of eruptive phenomena, such as Eruptive Prominences, Flares, and Coronal Mass Ejections, which are primarily attributed to interactions with the Sun's magnetic field. This section will elucidate the interrelationships among these phenomena.
In Section 1.4, we will delve deeply into the subject of prominences and filaments. This section will enumerate their various characteristics, both morphological and spatial, while also delving into the present theories regarding their magnetic configurations.
Finally, in Section 1.5, we will explore the concepts related to the eruption of these phenomena and the mechanisms believed to be involved in this intricate process.

1.1 The structure of the Sun

The Sun is a luminous mass of ionized gas powered by the thermonuclear reaction taking place in its core where the hydrogen is transformed into higher elements. Its internal structure, a sphere of radius $6.96 \cdot 10^8$ m, is characterized by different layers, in order from the centre outwards: the core, the radiative zone, and the convective zone, each characterized by decreasing temperature and density as the radius increases. Extending outward lies the Sun's atmosphere, consisting of several tiers. These encompass the photosphere, the chromosphere, and the enigmatic, intensely heated corona.

1.1.1 Internal structure

The core The *core* of the Sun constitutes approximately 27% of the Sun's overall radius. Recent models suggest that it mainly consists of hydrogen. It boasts the Sun's highest temperature, reaching around 15 million Kelvin, and an incredibly high density of about 150 g/dm^3 (which is ten times denser than lead) due to the immense pressure. These attributes create an ideal environment for nuclear fusion, releasing energy continuously that radiates outward to the surrounding layers through the combination of radiative and convective transport.

The radiative zone When density reaches a certain level, heat is primarily transferred via radiation due to the limited distance photons can travel before getting absorbed. This phenomenon occurs in the "*radiative zone*" extending from the core to roughly 71% of the solar radius. Particles within this stratum remain stable since their temperature is lower than that of the core (approximately 5 million Kelvin). They absorb radiation, temporarily store it, and subsequently re-emit it as new radiation.

The convection zone As the temperature and density decrease further (around 2 million Kelvin or below) the radiative transport becomes less efficient, a new method of energy transport becomes

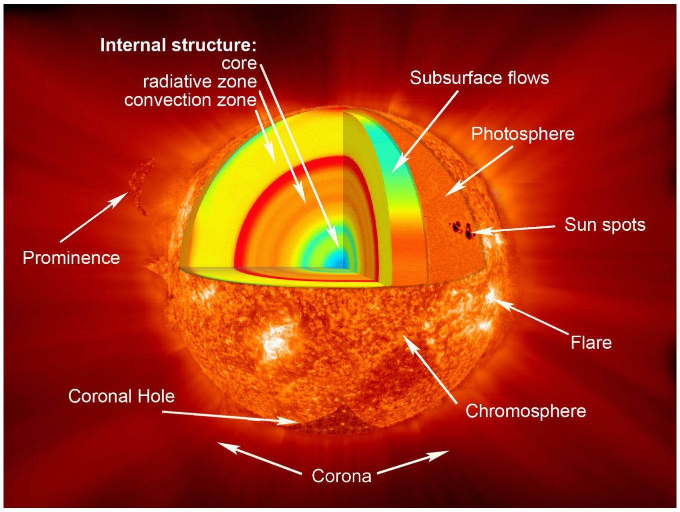

Figure 1.1: The structure of the Sun. ©NASA/Goddard

necessary, marking the boundary between the preceding layer and the "*convection zone*". Atoms in this layer effortlessly absorb energy but don't immediately emit it. These heated particles generates convective motions where warm gas particles rises upward and colder ones descending downward, carrying thermal energy with them through the surface.

The interface separating the radiative zone and the convection zone is called the *tachocline*, signifying two regions within the Sun with distinct rotation patterns. The radiative zone rotates as a solid body, while the convection zone exhibits a differential rotation more akin to the behavior of a fluid. The angular velocity of the Sun in the outermost layers strongly depends on the latitude, see Figure 1.2.

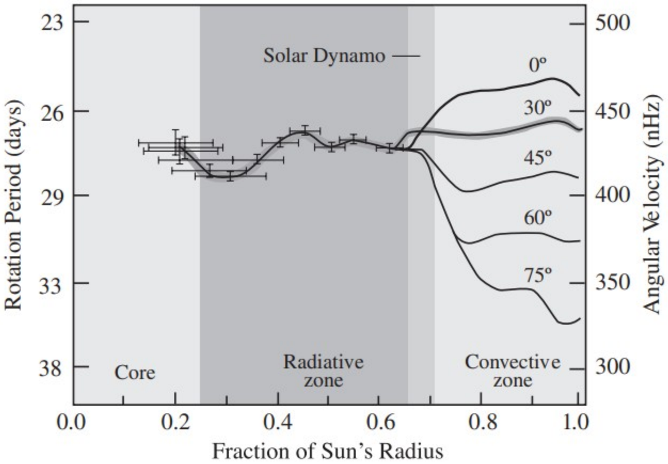

Figure 1.2: Internal rotation of the Sun. This rotational rate is deduced through helioseismology. As for the Sun's outer regions, they display a phenomenon known as differential rotation. This implies that areas at higher solar latitudes experience slower rotation compared to those near the equator [61].

1.1.2 Solar atmosphere

Photosphere At the uppermost section of the convective zone lies a layer known as the *photosphere*, spanning approximately 500 km in thickness. Despite the predominant conveyance of thermal energy through convection, this layer subsequently emits thermal radiation as visible light. Notably, this layer is also recognized as the apparent solar surface. Actually, the Sun consists entirely of gas, resulting in the absence of a solid surface. Nevertheless, this stratum designates an area where the density becomes

so high that is not possible to observe through. The photosphere is what we can observe (employing a suitable filter) from Earth looking at the Sun in the sky.
Upon closer observation, the photosphere exhibits a granular pattern attributed to the presence of granules. These granules result from structured convective motions, forming convection cells that manifest as notably bright areas. Simultaneously, one can also discern darker regions known as sunspots, which will be discussed later on. Temperatures within the photosphere range from 8000 K to 4500 K, decreasing as one moves farther away from the heat source. This temperature gradient results in the generation of absorption lines, referred to as "*Fraunhofer lines*", by the elements and molecules in the outer reaches of the photosphere heated by the innermost layers. These lines are particularly sensitive to the composition of the Sun's atmosphere and offer valuable insights into its constitution.

Chromosphere The *chromosphere*, positioned above the photosphere, extends to a thickness of approximately 1600 km. Within this region, various structures collectively form what is referred to as the chromospheric network. On the solar disk, one can discern dark filaments (referred to as prominences when located at the edges and seen in emission), as well as luminous "Plages" which are areas characterized by intensified magnetic field concentrations surrounding sunspots. Additionally, in the chromosphere one can see spicules, dynamic plasma jets that manifest as brief, dark streaks in $H\alpha$ observations and eject material in the corona at speeds of 20-30 km/s.
While its temperature ranges from 4500 K to 20,000 K, direct observation proves challenging due to its low density, resulting in fewer particles capable of scattering radiation, and the radiant brightness emanating from the photosphere positioned behind it. Notably, the elevated temperature within the chromosphere results in the release of the $H\alpha$ line at 656.28 nm from hydrogen, which falls within the red part of the spectrum, hence the name chromosphere. Additionally, the chromosphere is expected to manifest in emissions from neutral or singly ionized atoms, exemplified by the calcium K line at 393.4 nm (Ca II). However, to view these features, narrowband filters or the occurrence of a total solar eclipse become essential, as they facilitate isolation of the chromospheric characteristics from the radiance of the adjacent photosphere.

Transition region Above the chromosphere, the temperature rises dramatically from 20,000 K to 2 MK in the corona. Between these layers lies the *transition region*, approximately 100 km thick, where the temperature increases to 1 MK. This region, primarily governed by ions that have been ionized a few times, emits predominantly in the ultraviolet region of the electromagnetic spectrum. This ultraviolet region is observable only from space, as Earth's atmosphere absorbs Extreme-Ultraviolet (EUV) wavelengths along with X-rays.

Corona The corona, which is the Sun's largest and hottest region, reaching temperatures of about 2 MK, is incredibly rarefied at a density of 10^{-10} g/cm^3. The reasons behind its immense heat are not yet fully comprehended, making it one of the reasons why it is studied and one of the aims of the *Solar Orbiter* mission. Composed of plasma escaping from the Sun, the corona is observable in X-Rays, EUV, and visible, but in the latter it exhibits a faintness that is a million times less intense than that of the photosphere, and remains 1000 times dimmer than the luminosity of the sky [32].

The corona lends its name to the crown-like appearance that becomes evident during a total solar eclipse. Alternatively, it can be viewed using a coronagraph telescope, an optical instrument which emulates an eclipse obscuring the light from the intense solar disk, allowing for the observation of the cromosphere and the corona. Furthermore, due to its high temperature, the gravity cannot keep the plasma tied to the Sun. As a result, it expands into the interplanetary medium as a continuous stream of particles known as "solar wind".

1.2 The Magnetic Field of the Sun

The Sun's magnetic field is a highly complex phenomenon. In magnetohydrodynamics (MHD) it is described in terms of poloidal and toroidal components. These components play an important role in its structure, origin, maintenance, and amplification. The magnetic field varies across the Sun's surface and exhibits a periodic variability over time, following a quasi-period 11-year cycle. During this cycle temporary features like sunspots, active regions and coronal holes show significant variations, reaching their peak during the maximum phase. The magnetic field undergoes polarity reversal, completing the full cycle in a span of 22 years. Notably, the Sun's magnetic influence extends far beyond its immediate vicinity. The solar wind carries its magnetic field into space, creating the heliosphere, which interacts with the entire Solar System.

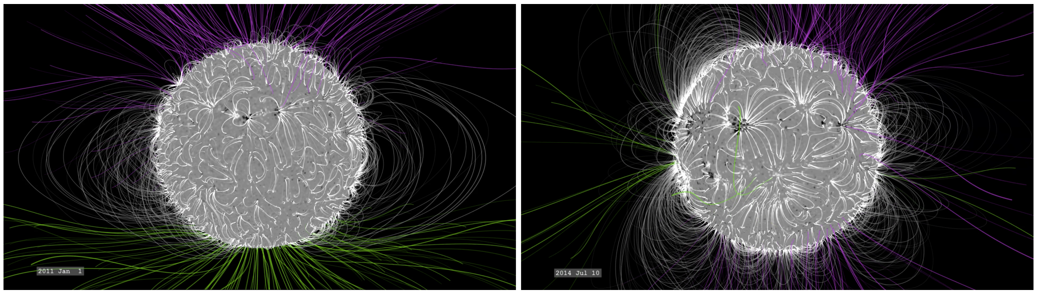

Figure 1.3: This comparison illustrates the varying intricacy of the solar magnetic field between January 2011 (*left*) and July 2014. In January 2011, three years after the solar minimum, the magnetic field retains a relatively straightforward configuration, featuring open field lines primarily concentrated near the polar regions. In contrast, on July 2014, the structure becomes notably more intricate, with a profusion of closed and open field lines extending in various directions. These conditions are particularly conducive to solar eruptions. ©NASA's Goddard Space Flight Center/Bridgman

1.2.1 The Solar Dynamo

The origin of the Sun's magnetic field remains a subject of ongoing debate. The most widely accepted theory is known as the "Solar Dynamo" theory. According to it, the kinetic motion of hot ionized gases flowing inside the Sun generates electric currents, which, in turn, produce magnetic fields. This process is similar to a dynamo, hence the changing magnetic fields create electric currents that help sustain the generation of electricity and the magnetic field itself. The magnetic fields produced by the dynamo process become embedded or "frozen" into the conducting gas, carrying the magnetic fields along with it. This phenomenon is described by Alfven's theorem of flux-freezing [3]. In astronomical systems, the Reynolds number, a measure of fluid flow, is extremely high, making this concept a good approximation for understanding the behavior of the Sun's magnetic fields. The Sun's differential rotation not only causes the plasma to rotate at different speeds but also results in the rotation of magnetic field lines. As a consequence, the magnetic fields line can undergo various transformations such as deformation, folding, stretching and twisting, leading to their amplification [85]. These processes give rise to the two different components of the magnetic field and are connected to other phenomena observed in the Sun's atmosphere.

1.2.2 Magnetic field in the atmosphere

Photosphere. The magnetic field in the photosphere is particularly complex and interacts with the plasma flow leading to the formation of small and larger features, as already mentioned in the Section 1.1.2 . The widest features are *sunspots*, which are cool and dark spots typically measuring about 10,000 km in size. They are associated with strong magnetic fields (typically between 1000 G to 2000 G), usually occurring in pairs with opposite magnetic polarity. These regions of strong magnetic activity are known as *active regions* and are often the source of eruptive phenomena on the Sun visible in the corona, though not always directly linked to sunspots. The number of sunspots increases as we approach the maximum of the solar cycle. At the beginning of the cycle they start to appear at lower latitudes.

The explanation for these features lies in the magnetoconvection theory: Biermann, in 1941, suggested that the lower temperature of sunspots is caused by the magnetic field inhibiting convection, opposing convective motions, a fact also confirmed by MHD simulations. Quoting Choudhuri [26]: "Nature seems to arrive at a partitioning of space between the magnetic field and the convection". In fact, in the Sun's convective zone, the magnetic field is approximated to remain concentrated in specific regions known as flux tubes, with weaker magnetic fields surrounding them. In 1955, Parker proposed the concept of "*magnetic buoyancy*", where under certain assumptions, flux tubes can become buoyant and rise against gravity. The idea is that the pressure gradient between the interior and exterior of the flux tube, where the magnetic field is strong, makes the frozen tube lighter than the surrounding gas, allowing it to rise. This experimental fact makes it possible to explain the occurrence of sunspots and their opposite polarity.

Chromosphere The magnetic field in the chromosphere is typically associated to the extension of these flux tubes rising through the photosphere and reaching the corona.
Its intensity and direction can be inferred from a combination between spectroscopy and polarimetry. The magnetic fields, in prominence for instance, show line emission primarily from scattered photospheric light, creating linear polarization due to Sunlight's directional nature. Magnetic fields alter this polarization, evidenced by fine structure splitting from the Zeeman effect[1] and depolarization through the Hanle effect[2] [85].

Corona The magnetic field of the Corona is thought to be responsible for a wide range of phenomena, between these the erupting phenomena such as Erupting Prominences, Flares and Coronal-Mass Ejections. Its direct measurement through spectroscopy is very difficult due to the negligible line splitting induced by its much weaker magnetic field, thus it requires specialized instruments (e.g., narrow-band spectral filters). The free electrons within the corona travel along the pathways delineated by magnetic field lines, giving rise to a variety of distinct configurations. These encompass: *Helmet streamers,* which are cusp-like structures with an elongated shape which demarcate regions with opposing magnetic polarities on the Sun's surface; *Polar plumes*, which are luminous features detected within the polar coronal holes of the Sun that exhibit that closely resembles that of open magnetic field lines. *Coronal loops*, which can be observed encircling sunspots and within regions of heightened activity on the Sun, see Figure 1.4a. These formations are linked to closed magnetic field lines, which establish connections between various magnetic areas present on the solar surface. *Coronal holes* which manifest as dim zones within the solar corona in Extreme Ultraviolet (EUV) and soft X-ray solar images, see Figure 1.4b. The reason for their dark appearance lies in their comparatively lower temperature and density in comparison to the adjacent plasma. These areas are characterized by unipolar, open magnetic field configurations. This unique magnetic structure facilitates a more unhindered release of the (fast) solar wind into space.

1.2.3 Force free field

Across the expanse of the solar atmosphere, a dynamic interplay emerges between charged particles and the magnetic field. This equilibrium relies in the ratio between magnetic pressure and gas pressure, indicated with the β parameter:

$$\beta = \frac{p}{B^2/8\pi} \tag{1.1}$$

Where p is the pressure of the gas, and B the intensity of the magnetic field. In the case of low β plasma ($\beta \ll 1$), a scenario commonly encountered, the influence of gas pressure is negligible compared to the magnetic pressure. Consequently, the pressure gradient alone cannot counterbalance the magnetic stress. As a result, the magnetic field must undergo an adaptation that leads to the elimination of magnetic stress. A magnetic field satisfying this condition[3] is known as a *force-free field.*.

From Figure 1.5 we see that below and within the photosphere, the gas pressure dominates over magnetic pressure ($\beta > 1$). This permits the magnetic field to be carried along by the motion of the gas. As these swirling gases are ionized and thus capable of conducting electricity, they effectively drag the magnetic field with them. In the lower corona, particularly within active regions the situation is completely opposite ($\beta < 1$). In this context, robust magnetic forces prevail and the magnetic field shapes the structure of the plasma in the corona, leading to the confinement of hot particles within coronal loops. Further out in the corona, the balance shifts again as gas pressure surpasses magnetic pressure. This occurs in regions where the magnetic field weakens in intensity. Consequently, the solar wind becomes the conduit for carrying the Sun's magnetic influence into the expanse of interplanetary space.

---

[1] The phenomenon of spectral line splitting due to the presence of a stationary magnetic field.

[2] A phenomenon where the polarization of light decreases when the atoms emitting the light are exposed to a magnetic field in a specific direction, especially when they have been previously excited by polarized light.

[3] Mathematically $(\boldsymbol{\nabla} \times \boldsymbol{B}) \times \boldsymbol{B} = 0$

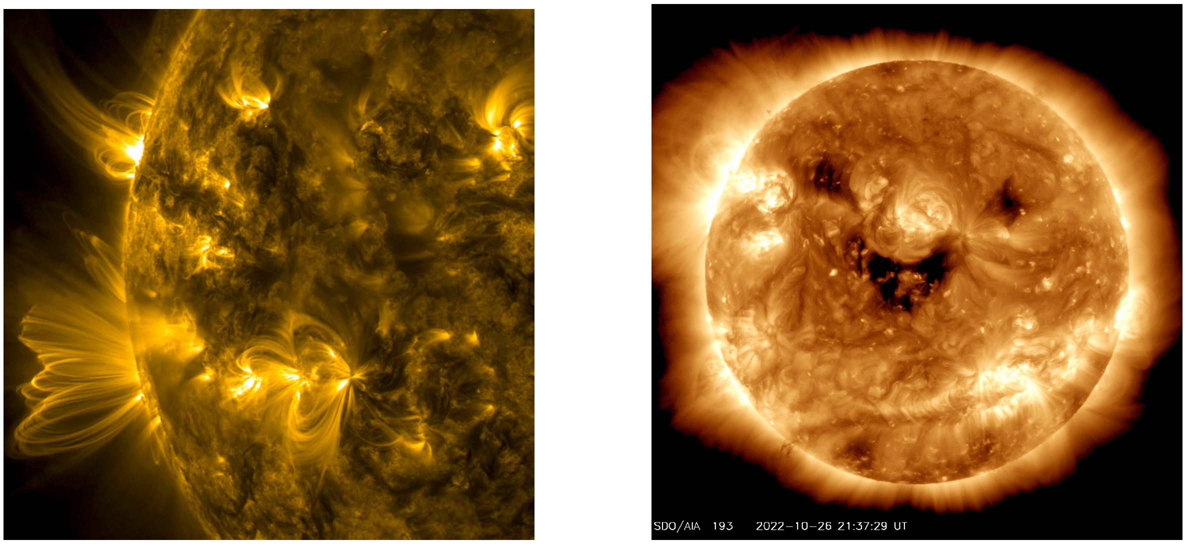

(a) A portion of the Sun characterized by heightened activity captured by SDO/AIA 171 Angstrom. ©NASA/Solar Dynamics Observatory

(b) Coronal Holes. In this picture captured by SDO/AIA at 193 Angstrom, a smiling face seems to emerge due to the configuration of the darker coronal holes in the filters. ©NASA

Figure 1.4: Corona's features. In the *left* image multiple active regions of the Sun marked by several coronal loops. In the *right* three coronal holes are observed.

1.2.4 PFSS model

As previously discussed in Section 1.2.2, obtaining the magnetic field in the solar corona remains challenging. To address this, various methods are employed to extrapolate the magnetic field from the photosphere into the higher layers of the solar atmosphere. Among these methods, the Potential-Field Source-Surface (PFSS) technique is widely employed. The PFSS technique derives the potential magnetic field model for the corona based on Gauss's theorem:

$$\nabla \cdot \boldsymbol{B} = 0 \tag{1.2}$$

This involves expressing the magnetic field as a function of a scalar potential Ψ where:

$$\boldsymbol{B} = -\boldsymbol{\nabla}\Psi \qquad \nabla^2\Psi = 0 \tag{1.3}$$

It assumes the presence of an imaginary sphere with a radius of $R_s = 2.5\ R_\odot$, referred to as the "*source surface*", beyond which all field lines are open and radial. The potential field components originate from both the inner boundary (the photosphere, i.e. $1\ R_\odot$) and the region outside the outer boundary delimited by R_s. See [114] for more details.

The lower-boundary data required for PFSS modeling are sourced from GONG synoptic magnetograms. These full-disk photospheric magnetograms are obtained from GONG's six observation sites and are utilized to derive comprehensive maps of the magnetic field across the entire solar surface. These maps are generated in near-real-time and cover integral Carrington rotations[4] [82].

The upper boundary is defined as an electric current source surface, where the magnetic field lines are constrained to be radial beyond R_s. This upper boundary approximates the impact of the outflowing solar wind on the magnetic field.

The PFSS model offers a reasonable approximation of the coronal magnetic field structure since the majority of the coronal field remains in a state of approximate Maxwell stress equilibrium. Although there may be instances of twisting and shearing in active regions, and the solar wind exerts inertial forces on streamers, neglecting these effects does not severely compromise the model's validity. In practice, the PFSS model demonstrates good agreement with MHD models [82].

---

[4] A system for counting Sun rotations, beginning with rotation number 1 on November 9, 1853, and using an average sunspot rotation period of 27.2753 days as the basis.

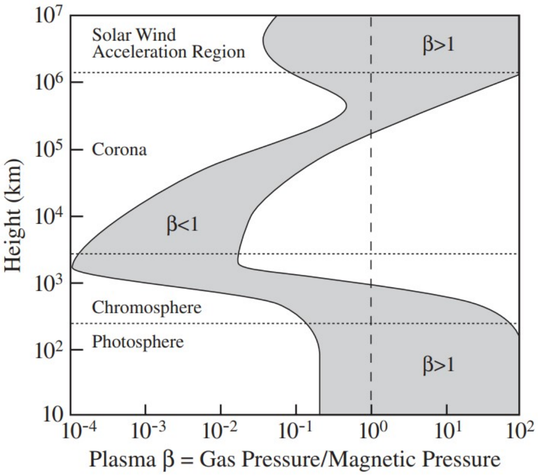

Figure 1.5: The relationship between gas pressure and magnetic pressure (β) as a function of the vertical distance from the photosphere (excluding non-radial structures) [61].

Despite its limitation, valuable insights can still be gleaned from the PFSS solution, such as information regarding changes over time in the global magnetic field's topology [73].

1.2.5 Magnetic Reconnection

I have already mentioned how the magnetic field emerges from its surface and permeates its atmosphere. It is important to note that these magnetic loops outline regions of positive and negative magnetic poles adjacent to each other. As the Sun's plasma continues to flow beneath the surface, these poles can shift positions. When the positive and negative poles slip past each other, it can result in twisting and instability, leading to the increase of the (magnetic) energy stored within the field. This occurs because the magnetic field is described in terms of a magnetic tension and pressure. Similar to the tension imparted to an arrow by a taut bowstring, the magnetic tension resists stretching and twisting increasing the energy of the lines.

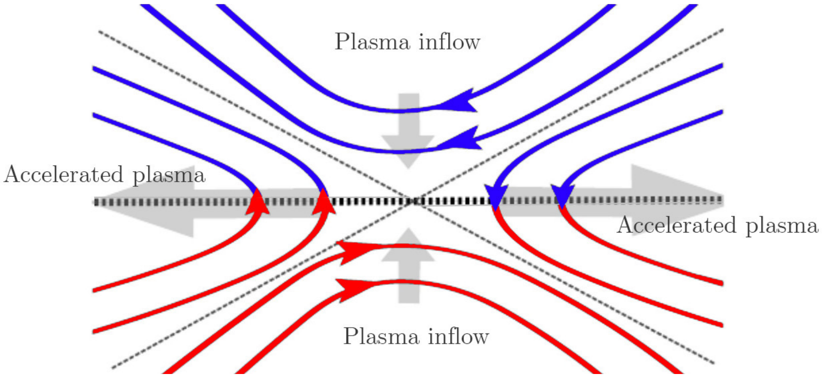

Figure 1.6: Representation of a single X point reconnection, this is a possible evolution of a current sheet. When two magnetic field poles (one blue and one red) converge at the center, they engage in magnetic reconnection, a process that leads to the acceleration of the surrounding plasma. Image adapted from [1].

When these magnetic lines of force make contact, a phenomenon known as *magnetic reconnection* can occur. This event disrupts the magnetic field's topology, releasing stored energy in the form of light and vast energy. The transformation of magnetic energy into kinetic energy propels particles into space. In the framework of MHD, magnetic reconnection is envisioned in fluid environments where resistivity is significant. However, in low-resistivity plasmas like the solar corona, the cutting and merging of magnetic field lines can occur within current sheets, regions where magnetic field gradient is large (e.g between positive and negative poles), due to the substantial gradient term in the hydrodynamics equation. The large gradient makes the resistivity of the fluid important within these regions and there the magnetic field is supposed to decay away. Consequently, the magnetic field weakens, resulting in reduced pressure. This, in turn, prompts plasma from above and below to converge toward the central region as in Figure 1.6, where the magnetic field once again undergoes decay, further attracting plasma.

Simultaneously, outside of these regions, the magnetic field can be considered "frozen" within the plasma, adhering to the assumptions underpinning our description of the Sun's magnetic field.

1.2.6 Observational signatures of the magnetic reconnection

Magnetic reconnection is believed to occur ubiquitously throughout the entire solar corona. Indeed, it is one of the two most widely accepted theories to explain the heating process in the corona. Supporting evidence for this can be found in the studies conducted by Raouafi et al., 2023 [96], and Chitta et al., 2023 [25]. These studies have documented instances of jetting (plasma) activities, observable in various forms, such as spicules, jets, and surges[5].

Furthermore, both before and during a solar eruption, there are occurrences of local brightenings in the Extreme Ultraviolet and Hard X-ray spectra, as well as radio burst emissions. These phenomena are considered as signatures of magnetic reconnection [85]. Others have characterized the observational signatures of magnetic reconnection as the presence of current sheets (e.g., Lin et al., 2005 [64]), the formation of multiple magnetic islands or plasmoids within the current sheet (e.g., Kumar & Cho, 2013 [58]; Patel et al., 2020 [86]), and the occurrence of supra-arcade downflows (Savage et al., 2010 [103]; McKenzie & Savage, 2011 [72]), i.e. void plasma cavities, which occasionally descend through the hot and dense plasma located above well-defined coronal loop arcades, particularly during solar flares.

1.3 Erupting phenomena

The powerful magnetic fields that permeate the atmosphere are closely linked to eruptive phenomena, such as flares, erupting prominces and CMEs that can occur within it, extending into space and eventually reaching our planet. This can initiate geomagnetic storms and affect the space weather of the rest of our solar system.

The significance of these occurrences becomes evident when we consider that despite being 150 million kilometers away, the disruptive effects of solar eruptions are still noticeable. The powerful radiation emitted by robust solar flares can traverse the distance to Earth in approximately 8 minutes, altering our atmosphere, interrupting long-range radio communications, and influencing the trajectories of satellites. Additionally, highly energetic particles accelerated during the flare process, moving nearly as swiftly as light, have the potential to jeopardize unshielded astronauts or even damage satellite electronics [61]. Thus, the exploration of these phenomena, their origins, and the potential for prediction has garnered growing attention in recent times, giving rise to the establishment of a field called "*Space Weather*". In today's technology-dependent society, this discipline has become indispensable.

Eruptive prominences, solar flares, and CMEs represent some of the most significant solar events that impact space weather. Detailed discussions about prominences can be found in Section 1.4, while the remaining events will be briefly covered below.

1.3.1 Solar Flares

Solar flares manifest as sudden and intense bursts of astonishing power, unparalleled in scale on Earth, constituting the most substantial explosions within the solar system. In a matter of minutes, the disruption propagates along tightly concentrated magnetic fields, advancing at the speed of light and releasing energy equivalent to millions of hydrogen bombs with a force of 100 megatons each, all detonating concurrently [61]. These extraordinary explosive surges become more frequent and intense as the count of sunspots rises. While their presence can be detected through radio waves, the bulk of their energy becomes apparent through X-ray and Extreme-Ultraviolet wavelengths.

Since the Earth's atmosphere absorbs this radiation, astronomers employ telescopes situated in outer

---

[5] Cool and dense ejections that are commonly observed in spectral lines associated with the chromosphere.

space to observe it. Given that the Sun's X-rays contribute to the formation of the ionosphere, it's perhaps unsurprising that X-rays emanating from solar flares have the potential to modify the ionosphere and disrupt its ability to reflect radio waves. For instance, this scenario can lead to substantial disruptions in aviation operations that depend on Global Navigation Satellite System (GNSS). The GNSS radio signals emitted by satellites, need to traverse this layer and are exceptionally vulnerable to interference during severe disruptions. As a result, unexpected discrepancies in both position and timing can emerge at the user receiver level. In the most extreme cases, the GNSS connection might be entirely severed [112].

1.3.2 Coronal Mass Ejections

CMEs are colossal magnetic bubbles that surge away from the Sun with speeds surpassing 1,000 kilometers per second, expanding to dimensions larger than that of the Sun in a matter of hours. These emissions carry billions of tons of matter into space, generating intense shockwaves and propelling vast quantities of energetic particles throughout interplanetary space observable typically in X-Rays and EUV (but also in visible light). The ones originating near the solar disk's center as viewed from Earth, manifest in coronagraph images as a ring or halo encircling the occulting disk.
A typical CME consists of three parts: the bright core, dark cavity and the bright front. An exhaustive description of this structure goes beyond the scope of this work, but it is useful to note that the bright core is the remnant of an eruptive prominence [124].

1.4 Solar Pominences

Solar prominences or filaments are regions in the solar atmosphere that contain relatively cool gas surrounded by the much hotter corona. The filament material, primarily composed of ionized plasma (mainly hydrogen and helium, like the rest of the Sun), exhibits temperatures characteristic of the chromosphere, immersed in the hotter corona. This region that separates the chromospheric material from the corona is referred to as the Prominence-Corona-Transition Region (PCTR). When observed on the solar disk, they are called filaments, and having high density makes them optically thick to certain wavelengths. As a result, they appear dark in hydrogen-alpha or extreme-ultraviolet images such as Hα 6562.8 Å (from the chromosphere) or in He II 304 Å, from the corona, contrasting against the bright background, the photosphere. This is where the distinction between prominences and filaments lies: when viewed at the edge or limb of the Sun, they can be observed in emission against the less-intense background, and that's what are referred to as prominences. In this study, we will use the terms "filament" and "prominence" interchangeably.

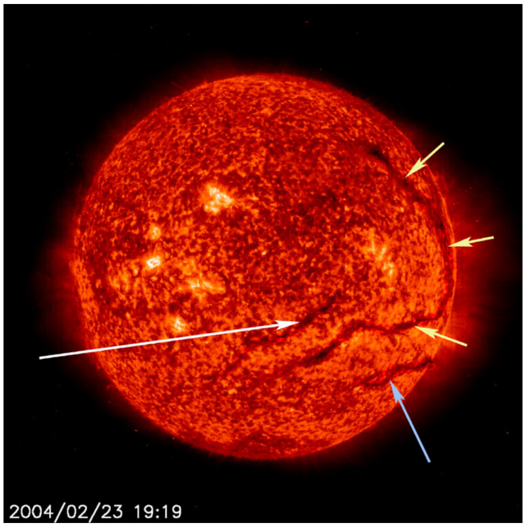

(a) Three filaments on the disk. ©NASA/ESA

(b) A frame extracted from a movie depicting an early prominence eruption captured by SDO/AIA. The footage is sourced from `http://sdo.gsfc.nasa.gov/gallery/main.php?v=item&id=1`. Provided by SDO (NASA) in collaboration with the AIA consortium.

1.4.1 Morphology

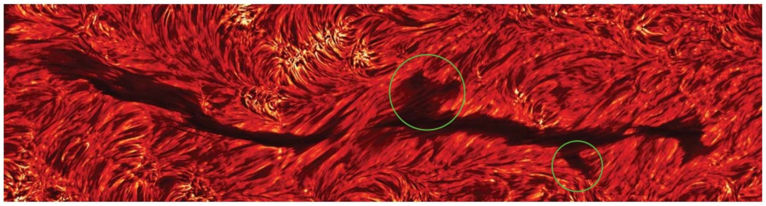

Figure 1.8: A high-resolution $H\alpha$ image of a filament captured on October 6, 2004, using the Dutch Open Telescope (DOT). The barbs are indicated by green circles [85].

The filament structure comprises a central spine, barbs, and two distinct ends, as described in Mackay et al.'s work [69]. When observed on the solar disk, as shown in Figure 1.8, these features become evident - the spine, a narrow structure aligned with the filament channel, and the barbs extending laterally from the spine as well as the ends (or legs). Each of these structures is observed to be composed of thin loops or slender thread-like elements of widths of about 200 km [69].

However, when observed at the solar limb, prominences exhibit a different appearance. In some cases the prominence consists of a collection of nearly horizontal threads or elongated blobs, most likely aligned with the local magnetic field. In other cases, the prominence consists of a collection of quasi-vertical threads or it may also appear to have more complex morphology, including arcades. The variation in appearance could be attributed to the filament's orientation relative to our line of sight. For instance, when observing the filament laterally (perpendicular to our line of sight), we primarily perceive its end parts, which may seem more vertical in our view. On other hand, when we view the filament from an opposite perspective, looking along its main axis (spine), we predominantly observe the arrangement of its underlying horizontal components, creating the impression of a flatter structure [85].

1.4.2 Location

Regarding the location, Moore et al. in 1989 [75], pointed out that filaments are found within sheared magnetic fields positioned above Polarity Inversion Lines (PILs). These PILs separate regions of opposite polarities in the photospheric magnetic field, where the radial component of the magnetic field changes sign. This configuration is confined to the *filament channel* that surrounds the PIL and extends upward into the corona, believed to be the magnetic structure that contains the filament plasma. The verification of this can be achieved by observing how chromospheric *fibrils*, slender elongated plasma structures visible in the solar chromosphere within and around magnetized regions [28], align themselves with the neutral configuration near a filament channel. Additionally, threads sometimes align with the prominence *spine* indicating a highly sheared magnetic field along the PILs[6]. This highly sheared configuration appears to play a role in prominence eruptions, which will be discussed in Section 1.5.

The properties and morphology of prominences (and their eruption) are closely related to the environment in which they originate. This correlation arises from the fact that the width, length, and shape of filaments are closely related to the extension of the neutral lines, although they may not cover the entire length of the lines. The extension of the PIL depends on the strength and distribution of the local magnetic field, resulting in a strong connection between filaments and the local magnetic field. PILs are prevalent throughout the Sun, especially during the solar cycle's maximum period, and filaments follow a similar distribution.

However, filaments are primarily found in three main locations: along the border of polar coronal holes (CHs), which is referred to as the *polar crown*; between active regions or surrounding them, known as intermediate filaments; and inside active regions [85].

---

[6] Actually, as pointed out by Mackay et al., 2010 [69], in several works it was observed that they are not necessary aligned with the structural component of the filament to which they belong but follow the local magnetic field.

1.4.3 Classification

It is quite common today to divide prominences into: Quiescent, Intermediate and Active Region prominences. Active Region (AR) filaments appear relatively compact, with typical lengths of about 30,000 km, and are often connected to opposite polarity sunspots. The AR filaments lead to the most powerful events, typically associated with flares. On other hand, Quiescent Filaments (QF) are typically wider, stretching across up to half a solar radius, with typical lengths up to 300,000 km and longer lifetimes lasting several months. These quiescent filaments are also connected with more extensive eruptions, but less powerful than the eruptions in the ARs [61]. Intermediate filaments is employed when it's not feasible to categorize them as either quiescent or active region. Beyond this classification, prominences and filaments do not exhibit uniform shapes and are characterized by high variability, which makes their classification challenging. Over the years, several sub-classifications have been proposed (e.g., Pettit, 1932 [89]; Zirin, 1988 [133]). In the data analysis for this study, I will employ a sub-classification system that aligns with the observed shapes of the prominences. Examples of this classification can be observed in Figure 1.9. In the upper-left panel of Figure 1.9, a loop-like prominence can be observed, while in the upper-right image, we can observe a fan-like eruption. Moving to the lower-left panel, a twisted eruption is shown, and in the lower-right image a jet-like eruption.

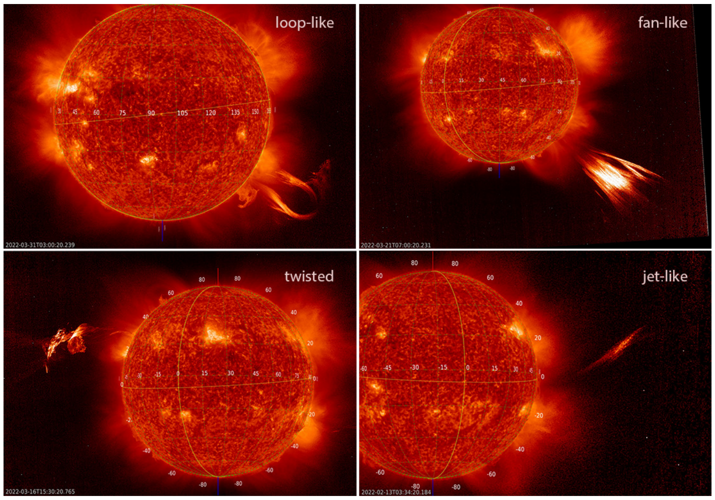

Figure 1.9: Prominences exhibiting different morphologies.

1.4.4 Formation

Filament formation is typically a gradual process that unfolds over the course of several days, especially when the structure is located at a considerable distance from an active region. To initiate filament formation, two key elements are essential: the establishment of a specific magnetic configuration capable of supporting the dense plasma within the filament and the surrounding corona, and the presence of a mechanism that gradually fills the channel with plasma.

Understanding the origin of the magnetic field (whether it originates from the photosphere, chromosphere, or corona) is closely intertwined with understanding how the filament channel becomes populated with plasma. Different models offer explanations for this process. The first category of models suggests that chromospheric plasma is directly injected into an existing filament-channel magnetic field. In contrast, other models propose that chromospheric mass is lifted along with the emergence of a flux rope or is transported into the corona through reconnection processes occurring at the photospheric or chromospheric layers. A third class of models suggests that chromospheric material is heated and transformed into coronal plasma, which subsequently condenses to form the distinct cool filament structure [85]. The following sections delve into the various magnetic configurations that have been suggested to provide support for the filament.

1.4.5 Magnetic configurations

The intricate arrangement of the magnetic field surrounding prominences is observed to be non-potential, indicating that it cannot be simply described using a basic scalar potential. However, a comprehensive understanding of this structure is still lacking. Current models primarily focus on the field's configuration, disregarding the processes that led to its formation. Kippenhahn and Schlüter, 1957 [56], illustrated how a magnetic field with localized dips, (i.e. where field lines are horizontally oriented and curve upward) can uphold cool plasma against gravitational forces. This can occur even in a potential field, such as when the underlying photospheric magnetic sources exhibit a quadrupolar structure. However, the magnetic fields within filament channels are neither potential nor static, as they encompass substantial electric currents.

Dips within non-potential magnetic fields can manifest due to various factors [69]. One scenario involves the weight of the prominence plasma distorting the field, resulting in the creation of magnetic dips. Conversely, dips might persist in the absence of prominence plasma, signifying that their presence is not solely due to the weight of the prominence itself.

According to these models, it's probable that the plasma within filaments is situated in proximity to the dips of the magnetic field lines. In cases where the plasma β is less than 1, the electric currents are inclined to flow almost parallel to the field lines, leading to a state of approximate magnetic force balance. Such force-balanced configurations can still exhibit dips in the magnetic field lines, even when the underlying magnetic field on the photospheric surface is dipolar. In fact, several researchers have proposed that filaments find support from nearly force-free *flux ropes* positioned horizontally above the PIL (e.g., Kuperus and Raadu, 1974 [59]; Pneuman, 1983 [91]; van Ballegooijen and Martens, 1989 [122]; Priest et al., 1989 [95]; Rust and Kumar, 1994 [101]; Aulanier and Démoulin, 1998 [10]; Chae et al. 2001, [20]; Gibson and Fan, 2006 [34]). Alternative force-balanced arrangements with dips, such as the *sheared arcade*, have also been explored as potential descriptions of the magnetic structure within filament channels (Antiochos et al., 1994 [7]; DeVore and Antiochos, 2000 [30]; Aulanier et al., 2006 [11]).

Magnetic Flux Rope (MFR)

The flux rope configuration is a coiled magnetic flux tube, where the majority of internal magnetic field lines wrap around a central axial field line that runs along the length of the tube, see Figure 1.10. MFRs are characterized by the presence of key features: a magnetic axis, a current channel, and a twist that extends across the entire length of the magnetic axis. They are categorized based on their twist number, denoted as N, which represents the number of turns from end to end. They can range from being "lightly twisted" when N is less than 1, up to "highly twisted" when N exceeds 2. It's worth noting that MFRs may not always exhibit uniform twist, but the defining characteristic of an MFR is that the degree of twisting within it significantly exceeds the degree of shearing. (A twist value around one is necessary for the formation of dips within the MFR [87]). Various mechanisms have been proposed to generate flux ropes, including twisting motions occurring at the photosphere (as described by Priest et al. in 1989 [95]), reconnection between sheared field lines (as suggested by van Ballegooijen and Martens in 1989 [122]), and the emergence of pre-twisted magnetic fields from beneath the photosphere (as outlined by Rust and Kumar in 1994 [101]).

Sheared Magnetic Arcade (SMA)

This magnetic configuration consists of a collection of field lines (or bundles of flux) that intersect a PIL while having an orientation that diverges from the local perpendicular direction to the PIL. The formation of a "sheared magnetic arcade" can arise through different processes. These include the shearing motions of the photospheric footpoints localized around the PILs, as indicated by studies by Antiochos et al., 1994 [7]; DeVore and Antiochos, 2000 [30]; Aulanier et al., 2006 [11]. Another formation mechanism involves the emergence of the upper portion of a flux rope or the influence of large-scale vertical motions. This magnetic configuration has been explored through numerical simulation [30]. This initially involved a basic bipole configuration embedded within a broader-scale dipolar magnetic field background. In this this simulation setup, strong footpoint motions occur in a parallel direction to the PIL and are confined to a narrow region on each side. These opposing flows drag the innermost part of the bipole into an area with a weaker magnetic field above, resulting in elongated field lines that protrude upward at their less restricted ends, creating dips. As this stressed

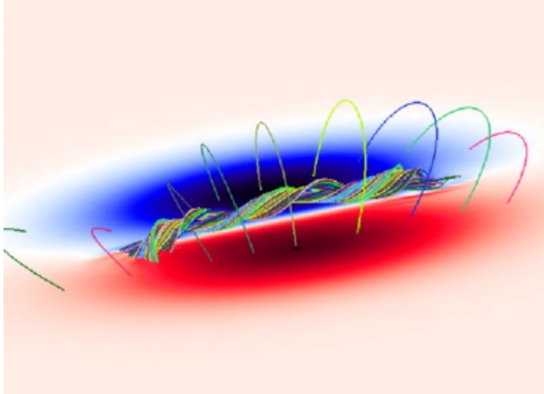

Figure 1.10: Flux rope configuration. The blue and red region represents the two different polarity region. The image is taken from Amari et al. 2003 [6].

system gradually relaxes, a range of field-line trajectories materialize. Some dipped field lines cross the PIL at an angle, leading to inverse polarity compared to the initial bipole configuration. Meanwhile, others undergo reconnection in the solar corona, giving rise to weakly twisted field lines. In DeVore and Antiochos, 2000 [30] we can visualize the process, refer to Figure 1.11.

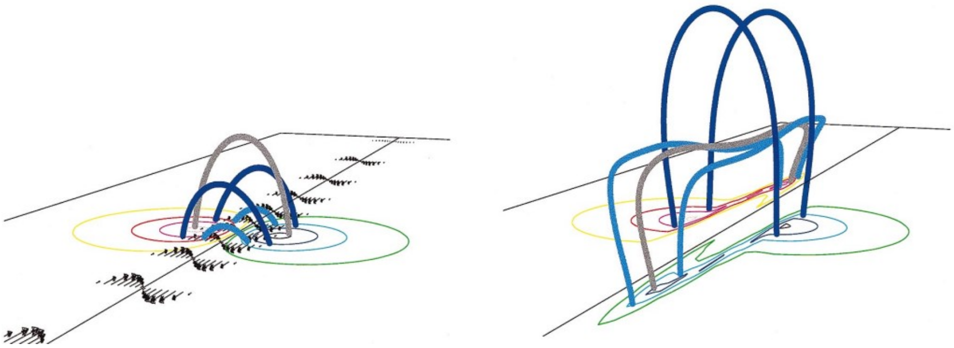

Figure 1.11: Sheared-arcade configuration. The left panels display the perspectives of the initial conditions, while the right panels depict the ultimate outcomes for minor footpoint shifts in the prominence model. On the lower surface, color contours represent lines of constant of the z component of the magnetic field B_z, while the thick loops signify specific magnetic field lines. In the left panels, black arrows indicate the direction and relative magnitudes of the applied footpoint displacements. The image is taken from DeVore et al., 2000 [30].

1.4.6 Eruptive prominences

As the magnetic field, originating at the base of the convection zone, emerges into the corona, it can collide with pre-existing magnetic fields, leading to the formation of layers of electric currents or even current sheets in the highly conductive coronal plasma. On the other hand, various photospheric motions, including differential rotation and various convection processes at different scales (supergranular, mesogranular, and granular) persistently pull the footpoints of all magnetic field lines, causing them to move in both organized and random patterns. This process results in the gradual buildup of a highly stressed coronal magnetic field [38]. Consequently, Poynting flux is constantly injected into the corona, and magnetic energy is consequently accumulated over time. As the magnetic field accumulates energy, the flux tube can undergo expansion and untwisting, eventually reaching a critical level of instability. Thus, it has the potential to expand, resulting in either a twisted arched magnetic flux rope or a uniform untwisted one.

An erupting prominence typically undergoes a multi-phase kinematic evolution. It is characterized by three different stages, the slow rise phase in which the height of the prominence increases with constant velocity, the acceleration phase, in which the prominence accelerates and at the end of the acceleration phase is the propagation phase (not always observable) in which the prominence is moving with an approximately constant velocity (Zhang and Dere 2006 [131]; Liu and Su 2021 [65]). Different kinematic characteristics indicate that different physical processes dominate in these phases. For example, Lorentz forces are dominant during the acceleration phase, while during the propagation phase the Lorentz force is comparable to the gravitational and drag forces (e.g., Temmer et al. 2011 [117]; Mierla et al., 2013 [74]; Majumdar et al., 2020 [70]).

However, the filament does not always erupt, sometimes the magnetic field simply relaxes without leading to the formation of a rising flux rope, in this case we speak of *failed eruption*. Consequently, the initial low-lying magnetic channel above and along the magnetic neutral line is restored, and the filament reforms at the same location.

1.4.7 Relation between flares, eruptive prominences and CMEs

All forms of solar activity seem to be linked to the sudden release of stored magnetic energy. However, the precise relationship among these phenomena remains uncertain. Several studies tried to explore the extent of this connection, the linkage has been documented to vary from as low as 3 % (Aschwanden et al., 2009 [9]) to as high as 90% (Gopalswamy et al., 2003 [45]). This wide-ranging variation can be attributed to disparities in analytical criteria, including the selection of events, which may not invariably exhibit all these phenomena simultaneously, variations in observation height within the field of view, and differences in temperature coverage [85].

In particular, there is a strong correlation between CMEs and eruptive prominences. In cases of CMEs with bright cores, it is evident that the material from eruptive prominences is present within these cores (House et al., 1981 [48]). However, as pointed out by Filippov et al., 2008 [37], there are also instances of ejections without bright cores or events where it is challenging to identify the supposed prominence eruption or vanishing filament. On the other hand, there are filament eruption which are not linked to CMEs. This typically occurs during “confined” eruptions when the filament doesn’t extend too far but instead stabilizes at a certain height in a new equilibrium position (e.g., Töröok, 2005 [120])

Despite the diverse visual manifestations, these phenomena are widely thought to stem from identical underlying physical processes involving the disruption of the coronal magnetic field. Notably, in the most extensive eruptions, such as eruptive flares, it is typical for all three phenomena to be simultaneously observed [120]. Nevertheless, the precise models needed to comprehensively describe these phenomena remain a subject of ongoing deliberation which will be discuss in the following section.

1.4.8 Deflections

Eruptive prominences, as well as CMEs, are naturally expected to spread outward in a radial pattern from the Sun. This is due to the spherical shape of the Sun and the resulting forces on the ejected plasma, including gravitational force, the Lorentz force, and the pressure gradient. It is also believed that the solar wind plays a role in influencing the spread of these phenomena. However, it is important to note that these forces may not be uniform across the entire surface of the Sun, and there can be additional forces affecting the motion of prominences and CMEs, causing deviations from purely radial propagation. Several authors have indicated that open magnetic-field lines from CHs can act as magnetic walls causing the CMEs to deflect away from these structures (see, e.g., Cremades, Bothmer, and Tripathi, 2006 [27]; Panasenco et al., 2013 [84]; Cécere et al., 2020 [19]; Sieyra et al., 2020 [111]). Specifically, Panasenco et al., 2013 [84] proposed that the existence of a CH introduces asymmetric global forces influencing the CME, causing the eruption to propagate non-radially. Moreover, several authors established that strong magnetic fields emanating from active regions where CMEs originate can also influence CME deflection (e.g., Möstl et al., 2015 [77]; Wang et al., 2015 [126]; Kay, Opher, and Evans, 2015 [55]). This deflection is proportional to some of the characteristics of the prominence as discussed by several authors in literature (e.g., Möstl et al., 2015 [77]; Wang et al., 2015 [126]; Kay, Opher, and Evans, 2015 [55]). The extent of this deflection is inversely related to the speed and the mass of the CME. During periods of solar minimum, slower and more expansive CMEs have a tendency to deflect toward the equator, while faster and narrower CMEs encounter less deflection and, in some instances, move radially away from their originating active region. In addition, several studies pointed out that also the total area of nearby CHs has a significant impact on CMEs deflections at low coronal height (Cremades et al., 2006 [27]), as well as the magnetic field intensity (Gopalswamy et al., 2009 [44]).

On the other hand, it is widely recognized that CMEs travel directly toward regions characterized by lower magnetic energy levels. These regions include the Heliospheric Current Sheets (HCSs), Helmet Streamers (HSs), and Pseudostreamers (PSs), which serve as attractors in such scenarios (e.g. Liewer et al. 2015 [63], Yang et al. 2018 [130], Cécere et al. 2020 [19]). The HCSs are described as a sprawling surface permeating the entire heliosphere where the magnetic field of the Sun transitions from positive (north) and negative (south) polarity. Within this region, there exists a minor electrical current, roughly measuring 10^{-10} A/m^2 [80]. HSs and PSs are distinct types of coronal streamers: the former delineates the boundaries between coronal regions with opposing polarity, while the latter demarcates the boundaries between coronal regions with the same polarity [127].

In addition, several studies pointed out that the total area of nearby CHs has a significant impact on CMEs deflections at low coronal height (Cremades et al., 2006 [27]), as well as the magnetic field intensity (Gopalswamy et al., 2009 [44]).

1.5 Eruption mechanisms

Various eruption models propose distinct triggering mechanisms accountable for the discharge of energy during an eruptive prominence (and/or CMEs), following the accumulation of enough magnetic energy to a critical threshold. In particular, the release of energy can stem from instabilities that invoke ideal or resistive processes. The former belongs to a category of force-free models that try to explain eruptions exclusively through the lens of an ideal MHD process, without necessitating any dissipation or dispersion of the magnetic field to function (and the conservation of the magnetic topology). While it is natural for a dissipative process like magnetic reconnection to occur, it is assumed that it does not contribute to the eruption of the field and the ideal process is the main responsible. The latter typically involves dissipative processes, such as the magnetic reconnection, where the sudden release of energy is thought to be a possible trigger for the eruptions. In the following we will explore the main mechanisms for the eruptions. Numerous theoretical models have been suggested to account for the sudden initiation and early progression of solar eruptions (refer to Forbes, 2000 [38] for an overview). In this context, our attention is directed toward the models below, however it is much more plausible that there is not a single mechanism responsible for triggering the eruption. Instead, it is probably the outcome of interactions between various processes.

Before introducing the various models proposed to describe initiation mechanisms, I will briefly describe the discussion brought by Aly and Sturrock in 1991, which questioned the practical feasibility of some of the models I am going to expound.

The Aly-Sturrock constraint

CMEs are thought to occur when closed magnetic field lines stretch out into interplanetary space. However, in the past, it was commonly assumed that before the eruptions began, the closed field lines had already become open driven by a loss of equilibrium or some form of instability. As suggested by Barnes and Sturrock in 1972 [13], Pneuman in 1981 [90], and Low in 1994 [66]. In 1991, Aly [4] and Sturrock [113] postulated that if all magnetic field lines were directly connected to the solar surface, the total energy of any force-free magnetic field couldn't exceed that of an open field with the same flux distribution on the solar surface. This concept was later termed the "*Aly–Sturrock*" constraint, suggesting that models explaining eruptive mechanisms might face limitations within the ideal MHD framework. Furthermore, Antiochos et al. in 1994 [7], proposed that even in three dimensions, the Aly-Sturrock energy limit could persist and potentially hinder the eruption of a single arcade, even with reconnection, as observed in the tether-cutting scenario discussed by Moore & Roumeliotis in 1992 [76]. However, even within the ideal MHD framework, various methods exist to circumvent the Aly–Sturrock constraint, allowing the initial magnetic field to possess higher energy than an open field. This suggests that the transition from the initial closed field to an open field is energetically possible, leading to eruptions driven by ideal MHD processes. For more details, you can refer to Chen et al. 2011 [22].

1.5.1 Resistive processes

Referring to the mechanisms involving dissipative processes, the first introduced is the tether-cutting model. Initially proposed by Moore and Roumeliotis in 1992 [76], it aims to explain eruption mechanisms in bipolar sheared systems. The magnetic field around PILs is observed to be notably sheared. This strongly sheared core field is covered by a less-sheared envelope magnetic arcade above the neutral field line. If the shear increases, it can lead to the formation of a current sheet beneath the filament and to magnetic reconnection. The onset of magnetic reconnection pushes up the filament, stretching the restraining arcade loops. This process generates a broad current sheet above the PIL, which has the potential to trigger a CME and produce a two-ribbon flare near the solar surface.
Similar mechanisms proposed as trigger mechanisms for CMEs are magnetic flux cancellation, see van Ballegooijen and Martens in 1989 [122], and shearing motions (e.g., Aly, 1990 [5]). However, in the 1990s, doubts regarding the feasibility of these processes emerged, giving rise to what was previously mentioned as the "*Aly-Sturrock constraint*".

Break-out model

The break-out model was devised by Antiochos et al., in 1999 [8] to overcome the Aly–Sturrock constraint. In this model, the initial magnetic configuration adopts a quadrupolar structure with a null point situated above the central flux system. The concept involves imagining that a CME is triggered due to substantial shear concentrated along the equatorial neutral line, causing the innermost flux within the central arcade to open up. Their study demonstrated that the final state, where the central flux system becomes fully open, possesses a total magnetic energy lower than that of the initial state. This finding suggests that partially opening a closed magnetic configuration is energetically viable.

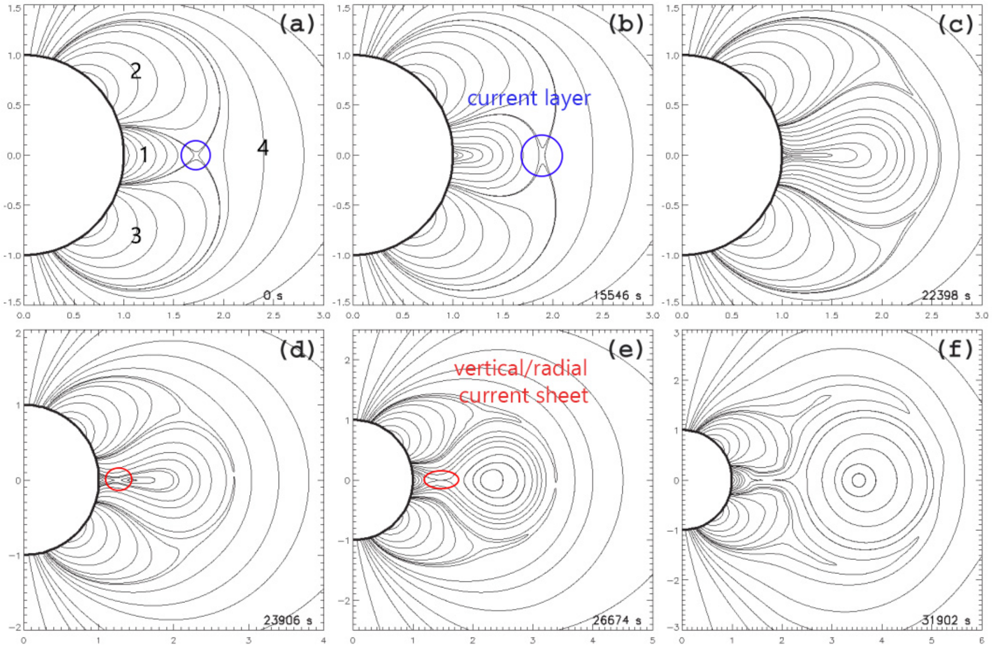

Figure 1.12: Meridional representations of magnetic field lines during the magnetic breakout eruption sequence simulation. The axis units are denoted in $R_\odot$, and the simulation time elapsed is displayed at the lower right corner of each panel. Image adapted from Lynch et al., 2004 [68].

The evolution of this configuration is illustrated in the figure 1.12 from Lynch et al., 2004 [68]. The quadrupolar topology is depicted by four distinct flux systems shown in Figure 1.12a: a central arcade positioned above the equator (1), two arcades associated with neutral lines at 45 °angles (2-3), and a global dipole (4). Two separatrix surfaces define the boundaries between these various flux systems, with a null point located at the equatorial intersection of these separatrices, as depicted in the encircled area. As the central flux system undergoes shear motions, it extends upward, causing the X-type null point to transform into a current layer (Figure 1.12b). If we disregard gas pressure and resistivity, this current layer collapses into an infinitely thin current sheet, impeding the upward movement of the central flux system. When considering gas pressure and resistivity, the current sheet undergoes magnetic reconnection due to anomalous resistivity or other non-ideal effects [22]. This reconnection process eliminates the constraint imposed by the higher magnetic loops, ultimately triggering the eruption of the core field, which is why it is referred to as "breakout" reconnection.

Comparing Figures 1.12b and 1.12c, it becomes evident that reconnection redistributes some of the restraining overlying flux to the side lobes. This loss of restraining field leads to a noticeable increase in the rate of outward expansion. As the central flux system ascends, a radial current sheet forms beneath it, as shown in Figures 1.12d and 1.12e. The reconnection within this radial current sheet, referred to as "flare" reconnection, results in the abrupt formation and ejection of a flux rope into the heliosphere, as illustrated in Figure 1.12f. The MHD simulation results of this eruption process were compared to observed CME features (Lynch et al., 2004 [68]), revealing that the height-time profile observed in the simulation data closely resembles a **parabolic profile**.

1.5.2 MHD instability

As the time scale for the gradual accumulation of magnetic energy in the solar corona is quite lengthy, in contrast to the rapid onset of events like flares and filament eruptions, Gold and Hoyle [43], as early as the 1960s, postulated that the triggering mechanism for releasing this energy must be associated with some form of instability. The fundamental concept is as follows: while the coronal magnetic field undergoes continuous evolution due to photospheric motions and flux emergence, it follows a quasi-static path, both in ideal and non-ideal conditions. However, there may come a point in its evolution where the equilibrium becomes unstable (i.e., instability) or where no nearby equilibrium state exists anymore (i.e., loss of equilibrium). The pre-CME is situated in an inherently unstable equilibrium and initiates its eruption in the solar corona, where disturbances are widespread.

Helical Kink instability

Solar eruptions often exhibit characteristics of a loop-shaped magnetic flux system with fixed footpoints at the coronal base and signs of magnetic twist [120]. Additionally, during the eruption, filaments frequently develop a distinct helical axis shape, which is a distinctive mark of an helical kink instability in a twisted magnetic flux rope (see Figure 1.13). The instability arises when the level of twist, indicating the winding of field lines around the axis of the flux rope, surpasses a critical threshold as pointed out in Hood & Priest, 1981 [47]. It is important to note that this early work did not account for the potential stabilizing effect of the external magnetic field that overlies the twisted flux tube. Such an effect was explored in MHD numerical simulations, as in the work of Török and Kliem, 2005 [120]. According to these authors, if the magnetic arcade above the twisted flux tube gradually weakens with height, the kink instability would be suppressed after its initial development, resulting in what is known as a "failed eruption", as observed by Ji et al., 2003 [51]. Conversely, if the overlying magnetic field decays rapidly, the kink instability would lead to an eruptive coronal mass ejection. Török and Kliem used numerical simulations to replicate the process. They began with an initial condition of a magnetic flux rope in a force-free equilibrium, represented as an arched, line-tied, and twisted structure. The flux rope

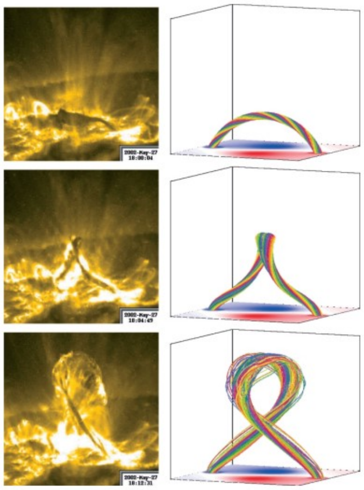

Figure 1.13: On the *left* TRACE 195 Å images capturing the confined filament eruption that occurred on May 27, 2002. On the *right*, magnetic field lines delineate the core of the flux rope undergoing kink instability. Image from Török and Kliem 2005 [120].

was modeled as the upper section of a toroidal ring current,
partly submerged below the photosphere. To ensure a finite twist throughout the system, they included a fictitious subphotospheric line current at the toroidal symmetry axis. Then, they modified the model by replacing the line current with subphotospheric dipoles, resulting in an equilibrium with a finite twist throughout the system, but with the magnetic field above the flux rope decreasing significantly faster with height than in the original model. This modification allowed them to simulate an eruptive event (a CME). In both scenarios, the observations revealed a slow-rise phase with a constant velocity, followed by an **exponential** growth phase in addition to the propagation phase.

Torus instability

A toroidal current ring's instability against expansion occurs when the external potential field decays rapidly enough with increasing radius, i.e. $\delta \ln B/\delta \ln r > 3/2$ (Bateman, 1978 [14]). This concept was later extended by Chen in 1989 [21] to study the dynamics of flux ropes in CMEs and was termed the torus instability" by Kliem and Török in 2006 [57].

In this type of instability, the force responsible for accelerating the ejecta is the hoop force or Lorentz-self force, arising from the curvature of a current-carrying flux rope (e.g., Titov and Démoulin 1999 [119]). In 2006, Török investigated the expansion instability of a toroidal current ring analytically in a low-beta magnetized plasma. The analysis considered only the hoop force and the stabilizing force from the external magnetic field, neglecting factors such as gravity, pressure, external toroidal fields, and any changes in the minor radius direction. The omission of pressure effects is justified since this instability primarily applies to low-beta plasmas, where the conversion of stored magnetic energy can drive significant expansion. The study revealed that **the expansion begins nearly exponentially**, following a $\sinh(t)$ function, which closely resembles a pure exponential growth.

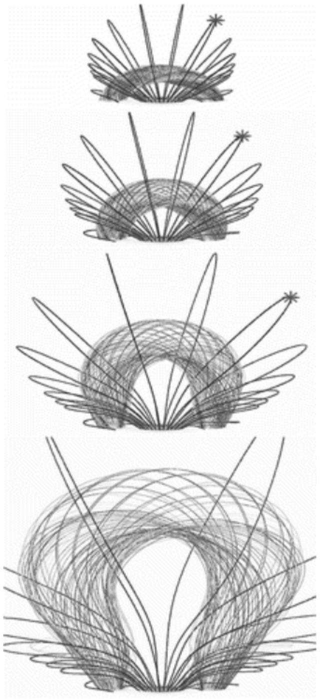

Figure 1.14: Side view of a torus instability simulation. The illustration displays torus field lines situated within a flux surface positioned at half the minor torus radius. Additionally, it presents representative field lines for the overlying magnetic field. Image from Schrijver et al. 2008 [105].

Schrijver et al. in 2008 [105], pointed out that the $\sinh(t)$ profile obtained analytically for the torus instability by Kliem and Török (2006) relies on the simplifying assumption that the external poloidal field varies with the major torus radius R as $B \propto R^{-n}$, with a constant decay index n. This assumption holds true only when the displacement from the equilibrium position remains infinitesimally small. In the same article the authors observed two events that appeared consistent with a torus instability, characterized by the expansion of a primary loop that approaches a toroidal shape. However, their results did not align with existing results in literature. Instead, they found that a power-law with $m = 3$ provided the best fit for their height-time profile. Thus, they conducted numerical MHD simulations of the torus instability to explore its evolution for finite displacements. These simulations closely resembled those of kinking flux ropes in Török and Kliem, 2005 [120], described before, and utilized the flux rope equilibrium by Titov and Démoulin (1999) [119] as the initial condition. For further details about the simulations, please refer to Schrijver et al. 2008 [105] and Török and Kliem, 2005 [120]. For some parameter settings, the exponential expansion held true for several initial radii of the current ring, while for others, a power-law-like expansion with exponents scattering around $m = 3$ was observed. This variation was linked to the influence of the initial velocity on the rise profile in these MHD simulations.

Catastrophe model

As demonstrated by MHD numerical simulations (e.g., Török and Kliem, 2005 [120]), linear instability analysis often has the limitation of not providing insights into the nonlinear development (Priest, 2007 [92]). Early efforts focused on exploring the potential for these processes, specifically the "catastrophe" of the magnetic system [22]. Building on the work of van Tend and Kuperus (1978) [123]; Priest and Forbes (1990) [93], developed a model to investigate the equilibrium of a line current filament within the background coronal magnetic field. It was observed that as the filament current or twist increased to a critical value, the flux rope exhibited catastrophic behaviour. In other words, the flux rope had the potential to pass from a lower energy level to a higher one (both resistive or ideal). The energy release in these processes is dependent on the background magnetic field, as indicated by Forbes, 1994 [41]. Thus, it may be insufficient to drive an eruption. However, the higher state involves a current sheet, and there reconnection can lead to the rapid eruption of the filament.
Priest et al., 2002 [94] expanded on the catastrophe model in a 2D context. In their scenario, converging photospheric flow or flux emergence results in the formation of a sheared arcade field containing a flux rope, enabling the formation of a prominence. The vertical section of the flux rope is illustrated in Figure 1.15, where the photospheric field sources are initially set at $x = \pm\lambda$, where λ is a parameter which describes the distance between the photospheric sources. As the magnetic configuration changes, the photospheric sources move closer together, causing the flux rope's height to gradually decrease while the magnetic energy increases until a catastrophic point is reached. Subsequently, the prominence erupts and, in an ideal scenario, approaches a new equilibrium represented by the dashed line in figure. However, if reconnection takes place, it occurs during the eruption in a current sheet below the prominence, allowing the eruption to continue catastrophically, provided that the reconnection rate is sufficiently fast. The rapid reconnection leads to releasing more energy and allowing the flux rope to escape, propelled upwards by the imbalance that develops between the magnetic compression and tension forces acting on it (van Tend and Kuperus, 1978 [123]; Martens and Kuin, 1989 [71]; van Ballegooijen and Martens, 1989 [122]). Without reconnection, all the kinetic energy released by the loss of equilibrium dissipates (or may eventually lead to oscillations between the lower equilibrium and the catastrophe one). However, in the presence of reconnection, the flux rope continues to move upward indefinitely, although its upward motion may slow once it exceeds the upper equilibrium. Before the formation of the current sheet, it can be demonstrated that the height of the prominence is proportional to time t up to a power law with an exponent of 5/2, i.e. $h(t) \propto t^{2.5}$, indicating early behaviour following the loss of equilibrium.

The primary limitation of the flux-rope model, as discussed above, is its two-dimensional nature. This simplification makes it easier for eruptions to occur because the ends of the flux rope are not anchored to the photosphere, as they would be in a three-dimensional model. It appears unlikely that additional anchorage could completely prevent an eruption. A reason is that in three dimensions, the flux rope can be kink unstable, facilitating an eruption. Therefore, Amari et al., 2003 [6] performed a 3D MHD simulations where the converging motion is imposed at the bottom boundary. They found that the flux rope always goes up (instead of decreasing before the catastrophe appears as discussed in Forbes & Priest, 1995 [40]; and Priest & Forbes, 2002 [94]); and demonstrated that this magnetic configuration cannot maintain equilibrium and releases a significant amount of magnetic energy during its disruption.

1.5.3 Other triggers mechanisms

The models described above were just a sample of the different trigger mechanisms which have been well studied in the literature. However, there are still additional mechanisms whose impact on solar eruptions remains poorly investigated [22]. One such mechanism is the *mass drainage*, which occurs when a portion of filament material descends to the chromosphere. In such cases, the filament loses its equilibrium due to the excess Lorentz force. This phenomenon was investigated by Fan and Low in 2003 [36], and Wu et al. in 2004 [128], and it has been identified in some eruption events, as reported by Zhou et al. in 2006 [132], and Seaton et al., 2010 [108].

Another mechanism is the *sympathetic effect*, a phenomenon where solar events like Moreton waves[7], EUV waves, or CMEs can trigger the oscillation or eruption of a distant filament. This effect can occur due to various factors, such as reconnection inflow beneath an erupting CME or the displacement of

---

[7] The chromospheric indication of an large-scale shock wave in the solar corona.

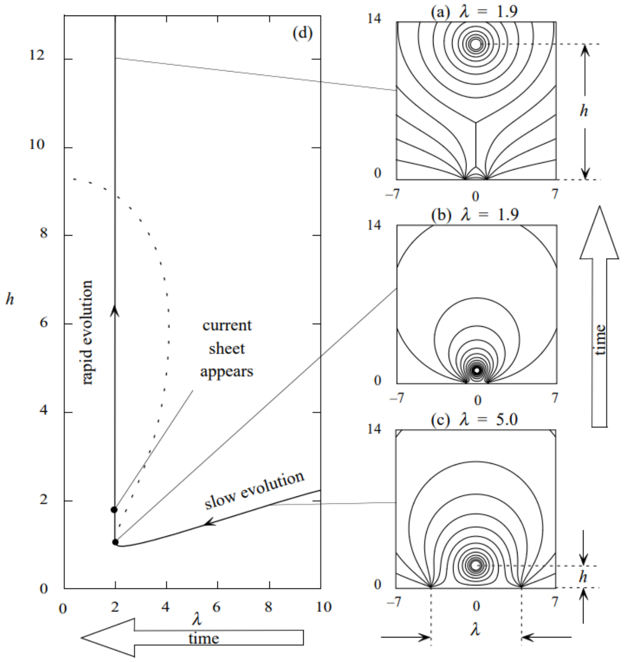

Figure 1.15: The catastrophe model for the eruption of an arcade containing a flux rope is illustrated. The three panels on the right depict the 2D field configuration at different time points, with the earliest time represented in the bottom panel (c). Over time, there is a gradual reduction in the separation between the photospheric sources, as depicted in panel (b), ultimately leading to an eruption, as shown in panel (a). On the left the height (h) of the flux rope is plotted as a function of λ, where the dashed curve represents the ideal-MHD equilibria that exist in the absence of reconnection (d) [94].

the background magnetic field caused by the CME itself, leading to the loss of equilibrium in nearby filaments (see Eto et al., 2002 [33]; Okamoto et al., 2004 [83]; Ballester, 2006 [12]; and Cheng et al., 2005 [23]). Additionally, the *solar wind* can play a significant role. The CME source region often has a closed magnetic configuration that is bounded by open magnetic fields, where the solar wind is accelerated from a nearly static state to several hundred km/s. It is possible that the CME source region may be pushed or influenced by the solar wind through drag forces, as discussed by Forbes et al., in 2006 [39].

1.5.4 Planetary Tides impact on Solar Activity

As mentioned earlier, solar activity is closely intertwined with fluctuations in its magnetic field. These magnetic field changes, spanning from the tachocline to the corona throughout the extensive solar atmosphere, are primarily attributed to the effects of solar differential rotation.
Since the discovery of the solar cycle in the late 19th century, researchers have periodically suggested a potential connection between planetary movements and solar activity. This hypothesis proposes that alterations in the solar magnetic field, leading to phenomena like sunspots, could be influenced by the gravitational forces exerted by planets. For example, in 2007, Hung [50] observed a significant correlation between the longitudes of major solar flares and the positions of specific planets in their orbits (Mercury, Venus, Earth, and Jupiter). Furthermore, there appeared to be an approximately 11-year cyclic alignment among these planets, which aimed to explain the sunspot cycle.

Nonetheless, as discussed by Seker in 2013 [110], this hypothesis remains a topic of debate. In particular, many statistical studies exploring the potential relationship between planets and solar activity have relied on the sunspot-number index as a straightforward proxy for solar activity. However, the sunspot-number index, which counts all visible sunspots regardless of their emergence timing, may not be the most suitable metric for investigating the origins of sunspots. For a deeper understanding of sunspot formation, it would be more logical to focus solely on newly emerging sunspots and cease counting them as they rotate with the Sun.

The hypothesis underlying this approach was that if planetary tides did influence sunspots, one would expect most sunspots to form near tidal peak regions, such as the longitudes of tidal planets or their antipodal positions. However, the results indicated that sunspot locations in the photosphere were not significantly correlated with the positions of tidal planets (e.g., Schuster, 1991 [106]), and their force strenght (Seker, 2013 [110]).
Indeed, various studies have attempted to calculate the influence of tidal forces from planets such as Earth, Mercury, Venus, and Jupiter on the Sun (Seker, 2013 [110]), as well as considering all the planets in the solar system (Liu Fu Gang, 2013 [42]). However, these forces seem to be too weak to significantly impact solar activity. Specifically, it has been found that the acceleration of the solar surface resulting from solar tidal forces is only one-twenty-thousandth of that resulting from changes in the Sun's rotation rate [42].

On a different note, an increase in solar flares has often been observed in coincidence with planetary alignments (Hung, 2007 [50]; Bertolucci et al., 2017 [15]; Petrakou 2021 [88]). Thus, as highlighted in a recent article by Scafetta and Bianchini in 2022 [104], there may be a connection between solar activity and planetary motion that could help resolve some unresolved issues in solar physics. However, they also pointed out that the acceleration of the solar surface resulting from solar tidal forces is small compared to that resulting from changes in the Sun's rotation rate. As a result, changes in solar tidal forces may not be as significant as fluctuations in the Sun's rotation rate, making it challenging to establish a clear correlation with solar eruptive phenomena. Based on the information presented above, establishing a correlation appears to be challenging and unlikely.

Chapter 2

Instrumentation and Data

The images presented in this thesis are from one of the ten instruments aboard Solar Orbiter (SolO, [78]). The ESA Solar Orbiter mission was launched on the 10th February 2020 with the aim of answering some of the open questions concerning the behavior of the Sun. The mission is characterized by an highly elliptical orbit reaching the closest approach to the Sun at 45 million km. In this way it tries to investigate the connections between the Sun and the outer solar atmosphere, the Heliosphere. This requires a close-up view of the Sun and observation of the solar wind before it becomes disrupted.

The primary instrument used in this analysis is EUI from SolO, its details are presented in Section 2.1. During the analysis also images from the AIA telescope onboard the Solar Dynamics Observatory (SDO) were incorporated. Thus, it will be briefly described in Section 2.2. A description of the data used on this work is provided in 2.3. Furthermore, in Section 2.4, I will offer an overview of the tools employed, such as jHelioviewer, for visualizing the data, and the STEREO Science Center tool to extract additional information regarding the positions of SDO and SolO at the times of the observations.

2.1 Extreme Ultraviolet Imager

The *Extreme Ultraviolet Imager* (EUI) consists of a collection of remote-sensing telescopes designed to capture high-resolution images of solar atmosphere structures spanning from the chromosphere to the corona. This set of instruments includes three telescopes sensitive to extreme ultraviolet wavelenghts. Two High Resolution Imagers (HRI) with exceptional resolution, one operating in the $Ly\alpha$ wavelength at 121.6 nm, and another in the extreme ultraviolet (EUV) at 174 Å. These imagers are respectively referred to as "HRI Ly-α" and "HRI EUV". The third, the Full-Sun Imager (FSI) is a wide field imager for observing the entire solar disk. It operates in the EUV passbands alternately at 174 and 304 Å known as "FSI 174/304". In all the units, the image formation is accomplished through a mirror-telescope operating at nearly normal incidence. The optical surfaces are equipped with specialized EUV multilayered coatings to achieve high EUV reflectivity and bandpass filters to reject visible and infrared radiation. In this dissertation the FSI 304 channel was used primarily and the FSI 174 was used for the description of the overall corona.

2.1.1 EUI components

The EUI instrument consists of two units, namely the Optical Bench System (OBS) and the Common Electronics Box (CEB), presented in Figure 2.1, which are interconnected via a connecting harness. The OBS houses the three telescopes, including mirrors, cameras, a filter wheel, filters, and a door mechanism subsystem. On the other hand, the CEB manages the coordination of instrument operations and handles the processing and compression of collected data. Photons are collected by a CMOS Active Pixel Sensors (APS) with a resolution of 3072x3072 pixels, where each pixel measures 10 µm. However, for the HRI channels, the sensors are windowed to 2048x2048 illuminated pixels. The APS is configured in a front-sided arrangement with an imager intensifier for the HRI-Lya channel, while a backside thinned configuration is utilized for the HRI-EUV and FSI channels. These detectors transform UV photons into electrical charges, subsequently amplified and digitized via an

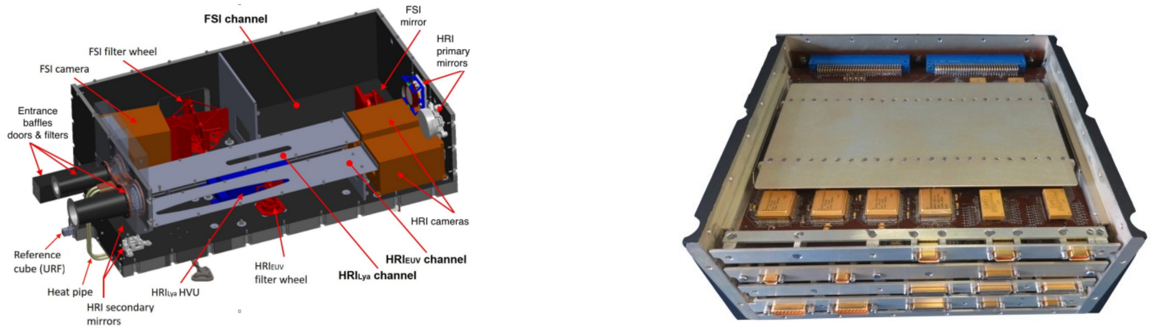

Figure 2.1: Schematic representation of the OBS (*left*) and the CEB units (*right*). Images from Rochus et al. 2020 [98].

A/D converter. The resultant signal in Digital Number (DN) for each detector pixel is directly linked to the exposure duration and the solar radiation within the particular bandpass, accounting for the pixel's limited viewing angle. Subsequently, the signal is converted into digital units by the front-end camera electronics and stored in the CEB.

2.1.2 FSI

The Full-Sun Imager aims to capture images of both the cold and hot layers of the solar atmosphere throughout the mission orbit. The quiescent and large-scale corona can be observed using the 174 Å bandpass, which primarily captures the emission lines of iron (Fe IX/X) formed at temperatures around 1 MK. The lower transition region instead can be imaged using the 304 Å passband, which is dominated by the helium (He II) emission formed at a temperature around or lower than 0.08 MK. The 304 passband also contains a number of weaker coronal lines, most prominently the Si XI line at 303.33 Å formed at temperatures of around 2 MK (Delaboudinière 1999 [29]; Labrosse and McGlinchey 2012 [60]).

The telescope aperture size of 0.5 cm enables the acquisition of acceptable signal-to-noise ratios with exposure times ranging from 1 to 10 seconds, with an angular resolution of 10 arcsec. [97]

One of the most important feature of this instrument is the Luxel Corporation filter. It is made of a layer of 150 nm of aluminum and is located behind the entrance pupil. It is supported by a 0.4 mm pitch hexagonal mesh grid and is designed to only allow EUV light to pass through the telescope while eliminating infrared and visibile light which may interfere with the EUV collection flux [98].

This allows high image cadence, facilitating observations of solar eruptive events such as erupting prominences, CMEs and flares. FSI is a single off-axis mirror, known as a Herschelian[1] telescope, which forms an image through a hexagonal entrance pupil.

The single mirror configuration was the only way to achieve the desired FoV of 3.8° × 3.8° with the allocated volume [98]. A schematic representation of the components of FSI is presented in Figure (2.2).

In classical multi-wavelength EUV telescopes, a common approach involves employing distinct multi-layer coatings on different segments of the primary and secondary mirror with a selector mask positioned at the front of the instrument (e.g. SOHO/EIT [29]; TRACE [46]; STEREO/EUVI [129]; SDO/AIA, [62]). This setup allows for independent channels, offering flexibility in selecting desired wavebands increasing the number of entrance pupils. In contrast, FSI adopts a

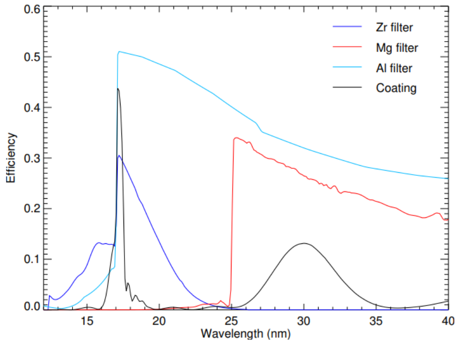

Figure 2.3: The multi-layer coating reflects two bands centered on 17.4 nm and 30.4 nm. Zirconium and magnesium filters are placed near the focal plane to select the wavelengths. The entrance aluminium filter allows both wavelengths to pass through. Images from Rochus et al. 2020 [98].

---

[1] A type of off-axis reflector telescope with just a primary mirror that reflects toward one side.

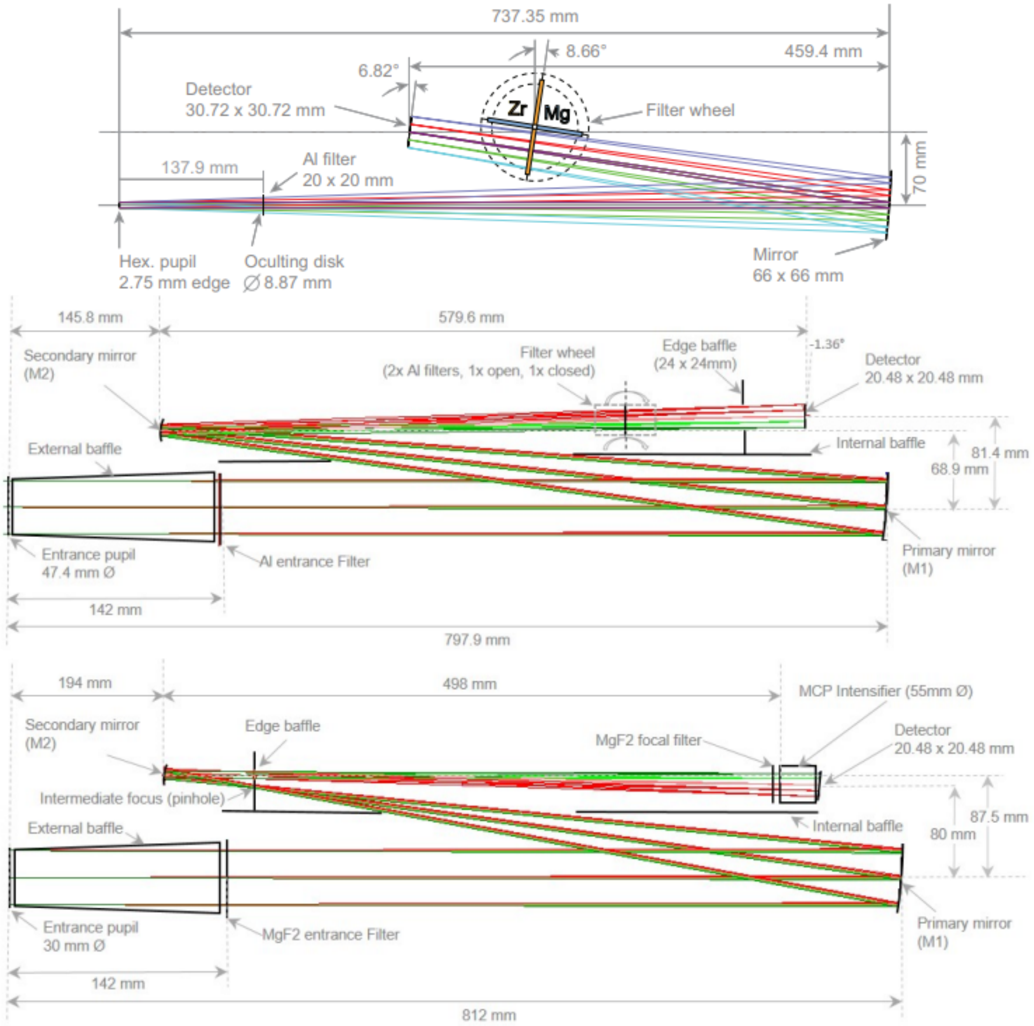

Figure 2.2: Optical scheme with the positions and coordinates of the main components of the FSI (*top*), HRI_{EUV} (*centre*) and HRI_{Lya} (*bottom*). Image from Rochus et al. 2020 [98].

single entrance pupil to minimize the instrument's heat load. Spectral selection in FSI is achieved through a combination of a multi-layer coating that reflects two bands and two types of filters that isolate each band. Referring to Figure 2.3, the multi-layer coating (represented by the black curve) reflects two bands centered on 174 Å and 304 Å . To select the 174 Å pass-band, an Al/Zr/Al (52 nm aluminium/96 nm zirconium/52 nm aluminium) filter is employed. On the other hand, the 304 Å pass-band is selected using an Al/Mg/Al (80 nm aluminium/322 nm magnesium/80 nm aluminium) filter mounted on a filter wheel near the focal plane. To address the fragility and potential development of pinholes in thin metallic filters over time, the filter wheel is designed to accommodate two filters of each kind [97].

During the later stages of development, it was decided to incorporate a mechanism for blocking direct solar disc light. This was achieved by adding a knife-edge occulting disc to the door mechanism located in front of the entrance filter. The occulting disc is specifically designed to be used when the distance from the Sun is greater than 0.34 au, which aligns with the remote sensing windows centered around the highest solar latitude points of the orbits. However, at shorter distances, the stray-light level is expected to be sufficiently low throughout the entire field of view (FoV), rendering the occulting disc unnecessary. To enhance its occulting capabilities, the vignetting cutoff is set at 0.777 degrees. As the distance from the solar limb varies along the orbit, the occulting effect increases, from 0.49 at the edge of the FOV reaching 0.75 in the corners [98].

2.1.3 HRIs

As already mentioned, EUI contains also two High Resolution Imagers which share a similar two-mirror optical structure, as shown in Figure 2.2. With its field of view of 1000 arcsec^2 is able to capture detailed images of the chromosphere, and the active corona of the Sun. To achieve this, two specific bandpasses have been selected. The Lyα at 1216 Å is the hydrogen transition (HI) which captures the emissions from the upper solar chromosphere at temperatures around 30,000 K. The 174 Å wavelength captures the emissions from the corona at around 1 MK.

The two channels are not described in detail as they were not used in the present analysis. In the Figure 2.4 it is possible to observe the difference between the images recorded by the FSI and HRI telescopes.

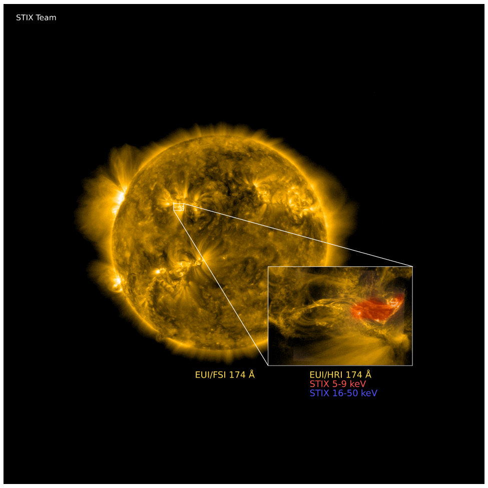

Figure 2.4: The difference in the way the EUI/FSI and the EUI/HRI are observing the Sun in the 174 Å wavelength. In addition, images from the Spectrometer/Telescope for Imaging X-rays (STIX) in two energy ranges are shown. STIX is another instrument aboard Solar Orbiter. ©ESA & NASA/Solar Orbiter/EUI & STIX Teams

2.2 Atmospheric Imaging Assembly

Since its launch on February 11, 2010, the Solar Dynamics Observatory (SDO, [62]) has been dedicated to investigating the origin and behavior of solar activity and its influence on space weather. SDO's instruments collect data on various aspects of the Sun, including its interior, atmosphere, magnetic field, and energy emissions, contributing significantly to our comprehension of our neighboring star. SDO comprises three telescopes, each with a specific focus:

- The Helioseismic and Magnetic Imager (HMI) examines the ripples and magnetic field properties on the Sun's visible surface (photosphere) by utilizing various colors or wavelengths.
- The Extreme Ultraviolet Variability Experiment (EVE) enhances our understanding of the Sun's extreme ultraviolet irradiance with superior spectral resolution, temporal frequency, accuracy, and precision compared to previous missions.
- The Atmospheric Imaging Assembly (AIA) offers continuous full-disk observations of the solar chromosphere and corona primarily in extreme ultraviolet wavelengths.

AIA was specifically designed to explore the origin and structure of the Sun's dynamic magnetic field and its corresponding coronal response. It has played a crucial role in enhancing our comprehension of the processes governing solar activity and the ways in which the Sun's energy is accumulated and discharged into the heliosphere and space.
It supplies multiple high-resolution full-disk images of the corona and the transition region up to 0.5 $R_\odot$ above the solar limb. These images feature a spatial resolution of 1.5 arcsec and a temporal resolution

of 12 seconds. AIA is equipped with four Cassegrain[2] telescopes that employ normal-incidence, multilayer-coated optics to provide narrow-band imaging in seven distinct extreme ultraviolet bandpasses centered on specific spectral lines. These include Fe XVIII (94 Å), Fe VIII, XXI (both at 131 Å), Fe IX (171 Å), Fe XII, XXIV (both at 193 Å), Fe XIV (211 Å), He II (304 Å), and Fe XVI (335 Å). One telescope observes C IV (near 1600 Å) and the nearby continuum (1700 Å) and features a visible light filter for precise alignment with images from other telescopes. In this study, our primary emphasis was directed towards the helium wavelength at 304 Å providing us with supplementary insights when observing the prominence eruption from an alternative perspective. Additionally, I made use of the iron-12 (Fe XII) emission at 193 Å to deduce details concerning regions in the corona with intermediate temperatures, approximately 1 MK. This specific wavelength is particularly adept at mapping coronal holes.

2.3 Data

The events analysed in this work were observed by the EUI/FSI 304 instrument aboard Solar Orbiter. In this section, I provide an overview of the data utilized in this study, giving details on their format, products, access and how to retrieve information to their selection.

2.3.1 Data format

The data presented in this work are in FITS format. The Flexible Image Transport System (FITS) is an openly accepted standard that defines a digital file format suitable for the storage, transmission, and processing of data, whether in the form of multi-dimensional arrays (such as a 2D image) or tables. This is the standard archival data format for astronomical data sets. Thus, the FITS format offers numerous advantages, from its capacity to store vast amounts of data to its fast accessibility through the keywords. Moreover, it is easily adaptable to any programming language.

Every FITS file comprises one or more headers containing ASCII card images[3] with keyword and value pairs, which are interspersed among data blocks and provides several information about the size, coordinates, binary data format, free-form comments, history of the data, etc... for each observation.

2.3.2 Data products

The access to the EUI data is permitted by the EUI Consortium's open data policy[4]. Regular reprocessing of the complete data archive is conducted to incorporate the ongoing enhancements in instrument comprehension and calibration optimization. Every data release contains three different levels of processing compliant with the standard agreed by the Solar Orbiter instruments in the Modelling and Data Analysis Working Group (Rouillard et al., 2020 [100]).

- Level 0: "Raw" Data. The data is extracted and decompressed, then saved in FITS files that contain minimal metadata, reflecting only the information present in the science telemetry packets.

- Level 1: "Engineering" Data. This is uncalibrated data saved in FITS files with comprehensive metadata adhering to the Solar Orbiter L1 standard.

- Level 2: "Calibrated" Data. This constitutes high-quality scientific data stored in FITS files, accompanied by metadata that adheres to the Solar Orbiter standard for L2. This data product has been meticulously calibrated and rectified for all instrument-related imperfections that were acknowledged by the EUI consortium during the data product's production.

- Level 3: "Visualization" data or Higher-level data. All EUI images will undergo processing as JPEG 2000 images to facilitate visualization through the JHelioviewer tool which is described in Section 2.4.1.

---

[2] Optical device typically consisting of two mirrors, a concave and parabolic primary mirror, called objective, and a hyperbolic convex secondary mirror.

[3] A "card image" is a conventional term referring to a character string, typically 80 characters long.

[4] `https://www.sidc.be/EUI/data-analysis`

In this research work, I utilized level 3 data from both EUI and AIA, which were sourced from JHelioviewer.

2.3.3 Data access

EUI FITS files can be accessed through multiple avenues. The most recent releases can be obtained via the webpage at `https://www.sidc.be/EUI/data/`. On this page, there is an image catalog available in the form of an SQLite database containing metadata for all L1 and L2 FITS files. Each image file corresponds to a row in the database, and each FITS keyword corresponds to a column in the database.
Additionally, EUI data can be accessed through virtual observatories, such as the Virtual Solar Observatory (VSO, [81]). Specifically, EUI data is accessible through the Solarnet Virtual Observatory[5] (SVO), which provides versatile data access options, including a web client, an IDL client, a Python client, and a RESTful API (an interface through which two computer systems securely exchange information over the internet).
Then, jHelioviewer is another tool to access to the data. The L3 images are intended to be viewed using this tool, which enables access to the header information of the FITS files. Further information is provided in Section 2.4.1.

2.3.4 Data selection

The EUI website from ROB/Solar Influences Data Analysis Center[6] (SIDC) contains a Solar Eruption list from where it is possible to retrieve information like date and time of the eruption in the Coordinated Universal Time (UTC), the instrument that observed the eruption (FSI 304 and/or FSI 174), position angle of the eruption (North-West, South-East ...), and a brief description of the event (large prominence eruption, jet-like prominence eruption etc.). Therefore, the EUI team at the Royal Observatory of Belgium provided me with a summary list of all the observations taken by EUI. From the metadata.db file (SQLite) available on the webpage `https://www.sidc.be/EUI/data/`, one can search the information needed, like cadence, which represents the interval between frames (the frequency at which the instrument captures observations), image type (solar image, dark image...), detector (FSI, HRI..) etc. The studied events are described in more detail in the following sections. The images are all obtained through the jHelioviewer tool.

2.4 Tools employed

In this section, I discuss the tools that were used in this data analysis. JHelioviewer was used for the visualization of the data as previously mentioned. On the other hand, the STEREO Science Center web tool played a crucial role in spacecraft localization, enabling us to compare observations from various spacecraft.

2.4.1 JHelioviewer

Helioviewer serves as a solar data visualization tool founded upon the JPEG 2000 compression standard, forming an integral aspect of the openly available ESA/NASA Helioviewer Project [79]. The JPEG 2000 compression enables efficient browsing across both spatial and temporal dimensions. jHelioviewer allows to view FITS data from various space missions (SDO, SOHO, SolO...) and attempt to ricreate a three-dimensional visualization from the Sun projection onto the plane of observation. In this work I used the ortographic projection for which all the projection lines are orthogonal to the projection plane, in this way the distance between points remains constant.
In the following I will discuss some of the features provided with jHelioviewer tool. For more details see Muller et al., 2017 [79].

---

[5] `https://solarnet.oma.be/`.

[6] `https://www.sidc.be/EUI/solar-eruptions`.

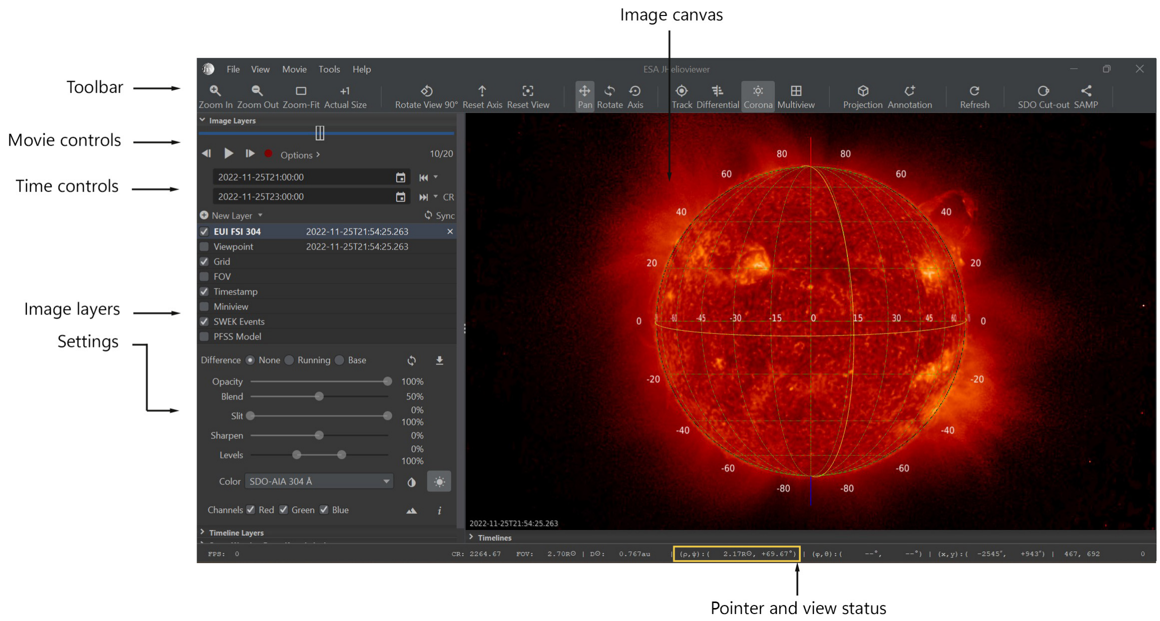

Figure 2.5: JHELIOVIEWER USER INTERFACE. The description is provided in the figure and in the text. The yellow box highlights the quantities extracted from jHelioviewer in the measurement procedure.

User interface Figure 2.5 provides an overview of the JHelioviewer user interface. The left side hosts all display controls and layer managers for the data displayed. On the right the image data (and eventually modelled magnetic field lines) is rendered on the main panel, the image canvas.
In the left panel, one can see the "Image Layers" which also contains the movie control. In this panel it is possible to select the time range in which I want to observe the Sun and add a new layer on the image canvas with the desired observation and cadence. For instance, in the Figure 2.5 is shown the FSI 304 on November 25th 2022, 21:54 UTC. The cadence of this data set is six minutes. From the same panel it is also possible to select other options. For example, it is possible to upload other observations from different instruments or channels, the timestamp and the PFSS model (see Section 1.2.4).

Real-time image processing JHelioviewer provides also some basic functionality as image sharpening, adjustments in brightness and contrast, modification of layer opacity, and the application of color tables. These are executed through OpenGL Shading Language (GLSL) operations, all of which are processed on the computer's graphics processing unit (GPU). This capability empowers users to make real-time changes to any of these settings, even while displaying multi-layer, high-resolution videos at frame rates exceeding 30 fps. Therefore it is possible to enhance the off-disk corona (sun button enhanced in Figure 2.5), and to invert the color table (drop button). These two features were particularly useful during the measurement procedure.

Position indicators The measurements were computed pointing the feature under study in the image canvas and right-clicking. In this way it is possible to copy and past the time and position indicators, such as: time (UTC) of the frame under study, the distance of the measured feature from the Sun's center, in solar radii, and the position angle of the measured feature, in degrees (ρ, Ψ). In addition it is possible also to extract information about the longitude and the latitude on the solar surface (φ, θ), the Cartesian coordinates (x, y), etc.

Creation and presentation of differential movies In JHelioviewer, every layer can be exhibited in one of three difference image modes: "No difference images", "Running difference", or "Base difference". By default, "No difference images" displays the standard image, which can make it challenging to identify time-dependent phenomena with subtle intensity variations. In numerous instances, it is more effective to discern such phenomena by examining movies composed of difference images. Each of these difference images illustrates the contrast between the original image and another image. This additional image can either be the previous one in the time series (referred to as "running difference") or a fixed reference image (referred to as "base difference"). In Figure 2.6, the three different modes are shown for the FSI 304 channel. Complementary, the FSI 174 channel (no difference) is also provided.

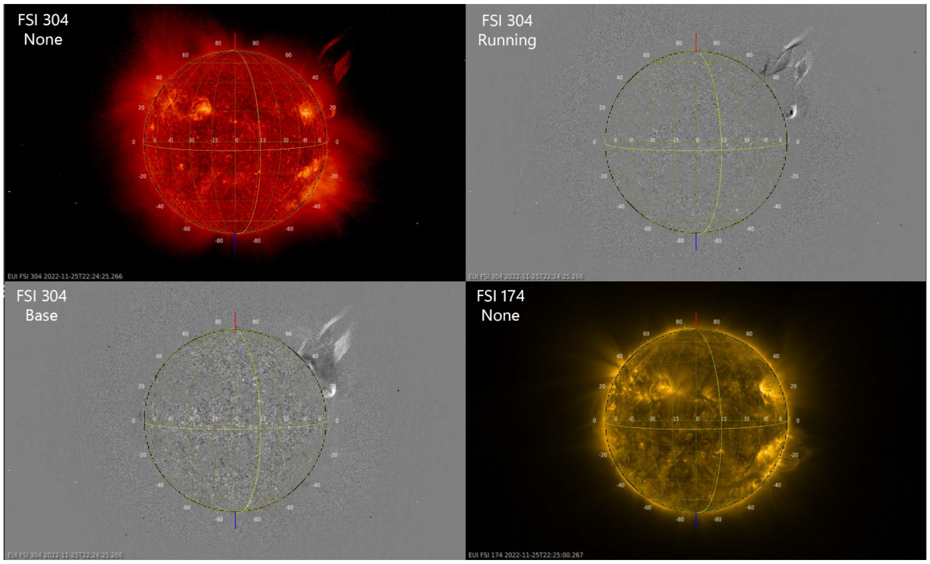

Figure 2.6: JHELIOVIEWER IMAGING MODES. Screenshots of the difference imaging functionality and the different channels. Images from 2022-11-25.

Image information It is possible to access the image information, i.e. the header of the FITS file, from the *i* button in the image panel, circled in Figure 2.7. This information is organized in three different columns (keyword, value and comment) and provides a large amount of information about the observations as: the instrument, the detector and the channel; the position of the spacecraft and the time of the observation; the size of the image and of the pixels, etc.

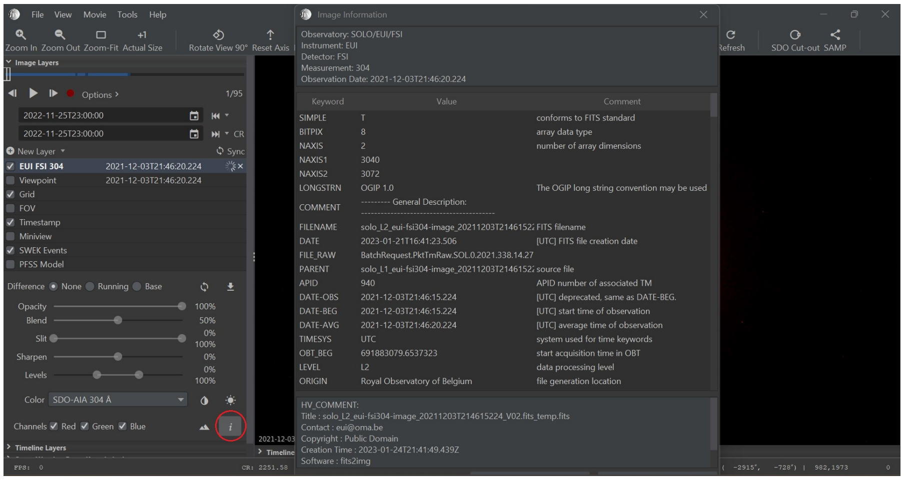

Observatory: SOLO/EUI/FSI
Instrument: EUI
Detector: FSI
Measurement: 304
Observation Date: 2021-12-03T21:46:20.224

Keyword	Value	Comment
SIMPLE	T	conforms to FITS standard
BITPIX	8	array data type
NAXIS	2	number of array dimensions
NAXIS1	3040	
NAXIS2	3072	
LONGSTRN	OGIP 1.0	The OGIP long string convention may be used
COMMENT	--------- General Description: --	
FILENAME	solo_L2_eui-fsi304-image_20211203T2146152	FITS filename
DATE	2023-01-21T16:41:23.506	[UTC] FITS file creation date
FILE_RAW	BatchRequest.PktTmRaw.SOL.0.2021.338.14.27	
PARENT	solo_L1_eui-fsi304-image_20211203T2146152	source file
APID	940	APID number of associated TM
DATE-OBS	2021-12-03T21:46:15.224	[UTC] deprecated, same as DATE-BEG.
DATE-BEG	2021-12-03T21:46:15.224	[UTC] start time of observation
DATE-AVG	2021-12-03T21:46:20.224	[UTC] average time of observation
TIMESYS	UTC	system used for time keywords
OBT_BEG	691883079.6537323	start acquisition time in OBT
LEVEL	L2	data processing level
ORIGIN	Royal Observatory of Belgium	file generation location

HV_COMMENT:
Title : solo_L2_eui-fsi304-image_20211203T214615224_V02.fits_temp.fits
Contact : eui@oma.be
Copyright : Public Domain
Creation Time : 2023-01-24T21:41:49.439Z
Software : fits2img

Figure 2.7: JHELIOVIEWER IMAGE INFORMATION. The image information is accessible through the i button encircled in figure.

2.4.2 STEREO Science Center

The STEREO Science Center (SSC) website offers a valuable tool for extracting data regarding the positions of the spacecraft from various space missions over a specific time. I utilized this web tool, which can be accessed via the following URL: `https://stereo-ssc.nascom.nasa.gov/cgi-bin/make_where_gif`, to determine the angular separation between SolO and SDO. This information was essential for comparing the images captured by the telescopes aboard these two distinct spacecraft, namely EUI and AIA.

The tool not only visualizes the orbits of the selected spacecraft but also provides additional details such as the Heliocentric distance in astronomical unit (AU), the coordinates in the Heliocentric Inertial (HCI) system, the Carrington coordinates, and more. For more details on different coordinate systems for solar image data refer to the paper of Thompson 2006 [118]. Given that SDO follows an inclined geosynchronous orbit around Earth, we can derive the angular separation between the two spacecraft by referencing it to the angular separation between SolO and Earth. An example of the result is provided in Figure 2.8.

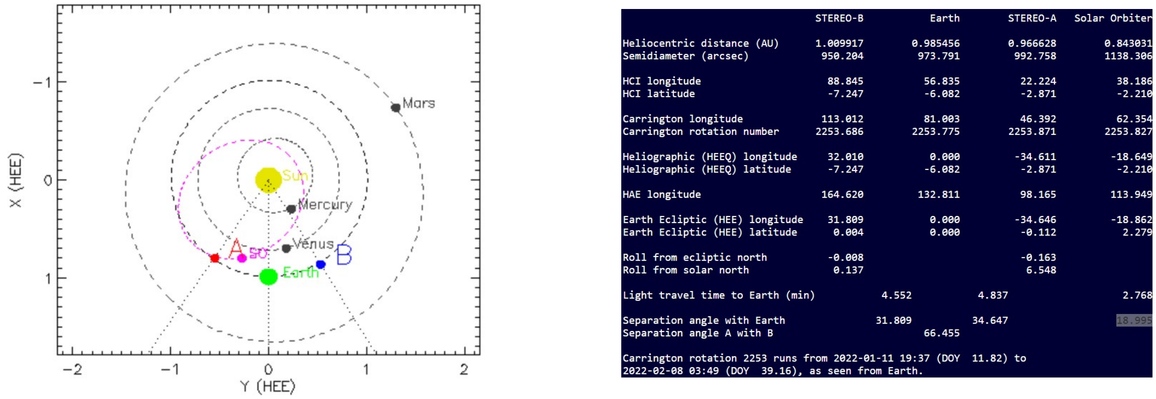

```
                                STEREO-B           Earth        STEREO-A   Solar Orbiter

Heliocentric distance (AU)      1.009917        0.985456        0.966628        0.843031
Semidiameter (arcsec)            950.204         973.791         992.758        1138.306

HCI longitude                     88.845          56.835          22.224          38.186
HCI latitude                      -7.247          -6.082          -2.871          -2.210

Carrington longitude             113.012          81.003          46.392          62.354
Carrington rotation number      2253.686        2253.775        2253.871        2253.827

Heliographic (HEEQ) longitude     32.010           0.000         -34.611         -18.649
Heliographic (HEEQ) latitude      -7.247          -6.082          -2.871          -2.210

HAE longitude                    164.620         132.811          98.165         113.949

Earth Ecliptic (HEE) longitude    31.809           0.000         -34.646         -18.862
Earth Ecliptic (HEE) latitude      0.004           0.000          -0.112           2.279

Roll from ecliptic north          -0.008                          -0.163
Roll from solar north              0.137                           6.548

Light travel time to Earth (min)           4.552           4.837                   2.768

Separation angle with Earth               31.809          34.647                  18.995
Separation angle A with B                         66.455

Carrington rotation 2253 runs from 2022-01-11 19:37 (DOY  11.82) to
2022-02-08 03:49 (DOY  39.16), as seen from Earth.
```

Figure 2.8: SSC example on February 2nd, 2022 at 00:10 UTC. At the top, you can see a visual representation of the orbits of the STEREO A and B spacecraft (marked as red dot A and blue dot B), as well as the Solar Orbiter (indicated as a fuchsia dot SO), all in relation to their positions relative to Earth (green point) and to the Sun (yellow centre point). Additionally, the orbits of others planets, as Venus, Mercury, and Mars are depicted. The axis represents the Earth Ecliptic (HEE) longitude (X) and latitude (Y) in degrees. In the lower image, various information are provided. The angular separation between Earth and SolO is highlighted.

Chapter 3

Data analysis

In this study, I aim to build upon the previous work conducted by Schrijver et al., 2008 [105], and Mierla et al., 2013 [74]. Specifically, the primary objective is to investigate the mechanisms responsible for the destabilization of erupting prominences. To achieve this, I seek to fit the most suitable model to the early phase of the eruption, which allows to discern the underlying eruption mechanism.
Schrijver et al., 2008 [105] conducted a study where they examined two near-limb filament destabilization events associated with CMEs on June 16, 2005, and July 27, 2005. They employed high-resolution, high-cadence observations from the *Transition Region and Coronal Explorer* (TRACE; [46]) in conjunction with coronagraphic observations from Mauna Loa Solar Observatory (MLSO) and the Solar & Heliospheric Observatory (SOHO, [17]). Their approach involved tracking the outlines of the top segments of the eruptive prominences and certain overlying loops. Their findings revealed that the heights of the filaments above the solar limb during their rapid acceleration phases could be best characterized by a height-time relationship represented as $h(t) \propto t^m$, with the exponent m being approximately equal to or slightly above 3 for both events. These profiles deviated from previously published results and models. Notably, they demonstrated that these height-time profiles could be well approximated by numerical simulations of torus instability when a significant initial velocity perturbation was applied to the developing instability.
Subsequently, Mierla et al. in 2013 [74] analyzed an event observed on April 13, 2010, using data from the SWAP instrument on the Project for On Board Autonomy (PROBA2, [107]) and from the two EUVI telescopes on the Solar Terrestrial Relations Observatory (STEREO, [49]). They tracked the reconstructed point at the top of the erupting prominence observed from these three telescopes. The height data was fitted with both a power-law polynomial function (with 5 degrees of freedom) and a cubic smoothing spline (with 10 degrees of freedom) to derive the speed and the acceleration. Both functions indicated a smooth and continuous increase in acceleration with height, with the power-law yielding an exponent m of approximately 6. Their conclusion was that the prominence was not immediately accelerated by local reconnection but was instead swept away as part of a large-scale relaxation of the coronal magnetic field.

The conclusions drawn from these studies demonstrated how interpolating data using a free coefficient power law can provide valuable insights into the mechanisms and forces driving prominence eruptions. Consequently, the procedure employed in this work will closely follow this approach. I will commence presenting the events selected for this study, Section 3.1. Then, I will introduce the measurement procedure and the statistical data processing in Section 3.2. I will also address the assumptions made regarding height measurements and propagation of the prominence in Section 3.3. Section 3.4 will detail the fitting procedure, including the functions utilized to model the initial phase of the eruption and the subsequent exclusion of the propagation phase. Finally, I will briefly discuss the calculation of pertinent kinematic quantities, such as prominence velocity and acceleration in Section 3.5.

3.1 Selected events

For this study I selected six prominence eruptions observed at high cadence by the FSI 304 instrument, in order to have sufficient images (or data points) for the analysis. The data (images) were acquired at cadences varying from 2 to 6 minutes, contingent upon the specific event.

I focused on prominences having loop-like morphology, as it was easier to follow the leading point. In this way I was sure that the same point of the prominence was tracked in successive images. Hence, the attention was primarily on regular events with a radial growth pattern. Larger, irregular events were excluded from the initial stage of the study. These regular events can be seen in Figure 3.1a, 3.1b, 3.1f.

Figures 3.1c and 3.1d show also a loop-like morphology with a leg of the prominence that seems to be in the backside of the Sun, and also a jet-like prominence eruption was studied (see Figure 3.1e). Events in Figure 3.1d and 3.1e exhibit a non-radial propagation.

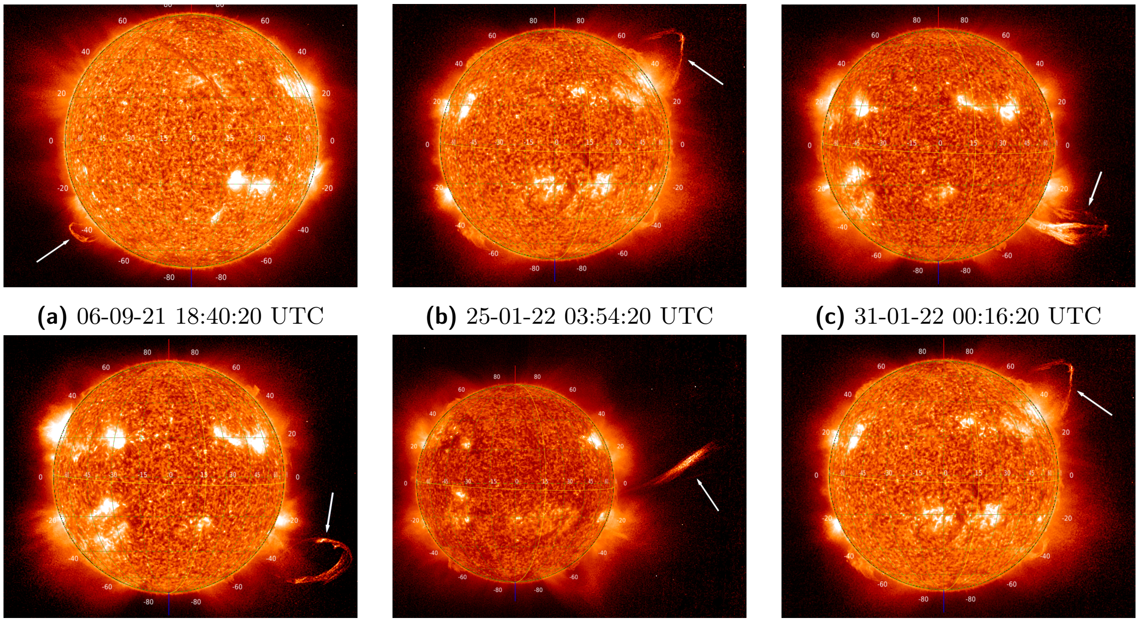

(a) 06-09-21 18:40:20 UTC **(b)** 25-01-22 03:54:20 UTC **(c)** 31-01-22 00:16:20 UTC

(d) 02-02-22 02:30:20 UTC **(e)** 13-02-22 03:06:20 UTC **(f)** 25-11-22 22:00:25 UTC

Figure 3.1: Selected prominences eruptions observed at the limb, shown in chronological order. The images are from EUI's FSI channel 304 on the Solar Orbiter and are viewed via the jHelioviewer software [79].

3.2 Measurement procedure

Once the events were selected, I tracked the tip of each event (prominence) in successive images provided by JHelioviewer. Starting from the last visible point of the prominence I worked backwards taking the measurements of the radial distance of the leading point from the center of the Sun. First, I inspected visually the evolution of the prominence while erupting and then I started the measurement from the last visible point of the prominence back in time. Tracking points in this manner was found to be more convenient, primarily because the final point tends to be the most challenging to discern. This difficulty often arises due to the presence of noise at the outer edges of the image field of view, among other factors. The majority of the tracked prominences followed a radial direction of propagation (i.e. they moved on a line connecting the center of the Sun and the leading point of the prominence). The distance was measured in solar radii ($R_\odot$) from the Sun center and it is referred to as "*height*". Furthermore, we gauged the position angle, representing the angle in degrees (measured counterclockwise) between the Sun's North direction and the aforementioned leading point. In the following we will refer to it as "θ ". Subsequently, to account for measurement uncertainties, the procedure was repeated under identical conditions, with the aim of re-measuring the same point as before three times. The mean value was computed by utilizing the three data sets for both height and angular position. Further explanation regarding this choice is provided in the subsequent subsection.

3.2.1 Uncertainties of repeatable measurements

When you can repeat the same measurement multiple times, the range of values you obtain offers a valuable indicator of the uncertainty in your measurements. Repeated measurements do not always reveal uncertainties, though. For instance, if we measure the distance between two points using a ruler and the instrument is not correctly calibrated (let's assume that the ruler is stretched and it removes 5% to the measured length), then all measurements taken with it will be 5% too short, and no amount of repetition (with the same instrument) will uncover this deficiency. Errors of this kind, which affect all measurements uniformly (and skews the results in the same direction), are referred to be *systematic* and can be challenging to identify.

Regarding the same example, another source of uncertainty arises when we need to interpolate between scale markings, and in this case, the direction of the effect will be *random.* If we repeat the measurement multiple times, we will sometimes overestimate and sometimes underestimate it.
As already mentioned, not all types of experimental uncertainty can be assessed through statistical analysis based on repeated measurements. In the book "An introduction to error analysis" of John R. Taylor [116], he classifies uncertainties into two categories based on: *random uncertainties*, which can be statistically analyzed, and *systematic uncertainties*, which cannot. Almost all measurements are subject to both these types of errors.

In general three measurements of the same quantity are not enough for statistical analyses, but it can be shown that this small number assesses the suitability of the model selected for the object of the study[1]. In this work, since the experimental conditions remain constant, and the measuring instrument remains unchanged (I exclusively used FSI 304), the systematic error will affect all measurements in a uniform manner or alter them in a consistent fashion. Thus, it is impossible to measure this type of error directly, as it necessitates comparison with a result obtained by repeating the same experiment under identical conditions using a more precise instrument or a different method.

If we disregard the influence of systematic errors (or manage to reduce them), we should be able to detect the remaining source of uncertainty, which is random, by repeating the measurement several times. Often, the best estimate is the **average** of the N values x_i obtained from the measurements:

$$\langle x \rangle = \frac{\sum_{i=1}^{N} x_i}{N} \tag{3.1}$$

An estimate of the average uncertainty of the measurements can be calculated as following. Given the mean, the difference between an individual measurement and the mean value, $d_i = \langle x \rangle - x_i$ (deviation) indicates how much that particular measurement differs from the average. These deviations have varying magnitudes and signs for each measurement. And at the same time, due to their random nature, the average of these deviations equals zero. To overcome this issue and estimate an average uncertainty, it is common practice to square all the deviations (resulting in a set of positive numbers) and then calculate their average. Taking the square root of this average yields a quantity with the same units as the mean, known as the *standard deviation* (or root mean square, RMS) of the measurements. In this work, I employed the *sample standard deviation* with N-1 instead of N in the average, as the alternative definition for RMS:

$$\sigma_{dvs} = \sqrt{\frac{\sum_{i=1}^{N} (x_i - \langle x \rangle)^2}{N-1}} \tag{3.2}$$

Pointing error calculation The measurements of the prominence height and angular position were performed with jHelioviewer by pointing a specific region of the prominence and by following it in successive images while it propagates outward. The measurement method inevitably introduces uncertainties due to the resolution limitation of the instrument. We refer to it as a '*pointing error*'. In order to resolve a feature in solar images at least two adjacent pixels are needed. The dimension of the pixel can be evaluated by using the keywords CDELT1, CDELT2 and RSUN_ARC available

---

[1] Increasing the number of repetitions the results are quite similar.

in the FITS file header. These values are provided through JHelioviewer. CDELT1 and CDELT2 are the X and Y dimensions of one pixel in arcseconds. They have the same value as the pixel is a square. RSUN_ARC is the apparent radius of the Sun in arcseconds. In order to convert the dimension of a pixel from arcseconds to kilometers, the dimension of the pixel was multiplied with the ratio between the value of a solar radius in kilometers and RSUN_ARC. The value of the solar radius in kilometers (RSUN_REF) was also taken from the FITS header information. In this work the spatial resolution is set to 2 pixels, this is due to the large scale nature of the features under measurement, which is not possible to be resolved in only one pixel, but needs at least two. At this point the dimension of the pixel must be evaluated in km. In order to convert the dimension of a pixel from arcseconds to kilometers, the dimension of the pixel was divided by the radius of the Sun in arcseconds and multiplied by the value of a solar radius in kilometers[2].

$$\sigma_{pnt} = 2 \cdot \text{CDELT1} \quad \frac{695700}{\text{RSUN\_ARC}} \qquad [\text{km}] \tag{3.3}$$

Thus, the uncertainties associated with the averaged values were determined by taking into account both the standard deviation of the repeated measurements and the so-called pointing error. The standard deviation of the iterations σ_{dvs} should accommodate fluctuations in the measurements. The pointing error σ_{pnt} represents the uncertainty introduced to address the limited resolution of the large-scale features being analyzed.
Therefore the uncertainties on the averaged values were calculated as:

$$\sigma = \sqrt{\sigma_{dvs}^2 + \sigma_{pnt}^2} \tag{3.4}$$

where I am making the assumption that the uncertainties are uncorrelated and follow a standard normal distribution.

3.3 Assumptions

The mentioned procedure relies on a number of assumptions:

1 The prominence is moving radially;

2 The prominence is exactly in the plane of the sky (POS) of the observer to minimise the projection effects;

3 The rotation of the Sun does not affect our measurements.

The prominences selected for this study were in or very close to the POS. The way this small deviation from POS affects the measurements is described in Section 3.3.2. While the majority of the events were propagating radially (i.e. constant position angle), there were a couple which were moving non-radially and this is described in Section 3.3.1. The way the solar rotation affects the measurements is described in Section 3.3.3. Therefore, the two main assumptions involved in this work are that the prominence is moving radially and in the plane of the sky (i.e. the image plane containing the limb of the Sun as seen from Solar Orbiter perspective). This means that the measured height (i.e. the distance of the feature from the solar center) directly corresponds to its real height. However, if the prominence deviates from the POS, the quantity measured is not the actual "real height", a term we will employ throughout this section to refer to the factual elevation of the prominence. This will be discussed in the next section.

3.3.1 Radial propagation

A case of a prominence moving in the POS and deflected from its radial direction by an angle δ is depicted in Figure 3.2. This situation often occurs because of the lateral forces acting during the prominence eruption. The surrounding corona has a big influence on the prominence direction of propagation. For more details refer to Section 1.4.8.

---

[2] Radius of the Sun in kilometers 'RSUN_REF' is extracted from the FITS header, through jHelioviewer.

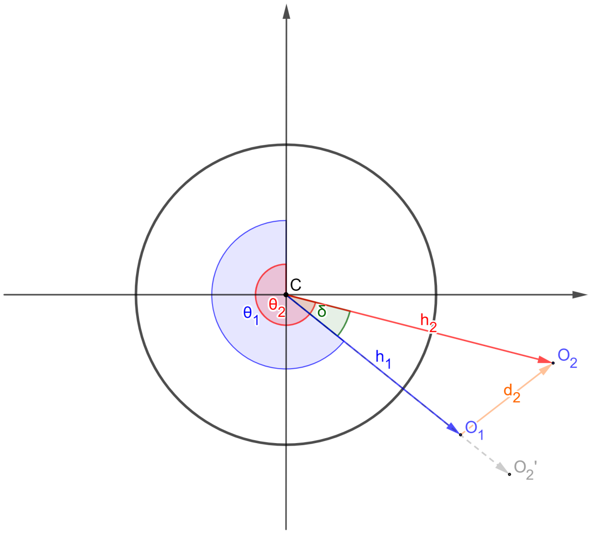

Figure 3.2: Visualization of the measured quantities. The height measured in jHelioviewer is represented by a vector h_i, where i is the index of the feature under study, and θ_i the position angle. Additionally, δ, the angle between two consecutive measured points, and d_i, the depiction of the two successive points shows a clear deflection (or deviation) from the radial propagation direction. O_2' represents the ideal situation in which the prominence propagates radially.

3.3.2 Projection effect

In this study I selected events propagating in a plane not far away from the POS (i.e. limb events) in order to minimise the projection effects. This decision also helps reduce uncertainties associated with measuring the height of the erupting prominence.

In Figure 3.3, I depict the measurement scenario for an event positioned behind the solar limb at a specific angle φ. When measuring the height of the prominence, what we are actually assessing is its projection within the plane of sky. Consequently, the parameter h represents the projection of its real height, designated as h_{real}, assuming that the angle remains constant throughout its propagation. The value of h_{real} can be determined through trigonometric calculations as follows:

$$h_{real} = \frac{h}{cos(\varphi)} \tag{3.5}$$

At this point, we can calculate the percent error, i.e. the relative error multiplied by 100, according to the following expression:

$$\epsilon_{\%} = \frac{|h_{real} - h|}{h_{real}} \cdot 100 \tag{3.6}$$

The relative error in deriving the real height, with respect to the measured one, versus the angle with respect to the POS is depicted in the graph in Figure 3.4. The average discrepancy is observed to increase as the angle φ varies from 0 to 90 degrees. The orange cross represents instances of eruptions in this study, such as “Event 4”, which were observed at an angle of 19 degrees off the solar limb during the eruption. In that case, the percent error is less than the 10% of its value, so it is comparable with the other sources of uncertainties. The projection effect has the potential to become the primary source of error when measuring prominence heights and might necessitate correction when feasible to determine the angle at which the prominence is situated in relation to the limb. One approach to address this is by observing the event with an alternate telescope positioned at a different location. An instance of this is the utilization of the AIA 304 channel within the Solar Dynamics Observatory (SDO) that allowed us to observe these events from a different perspective.

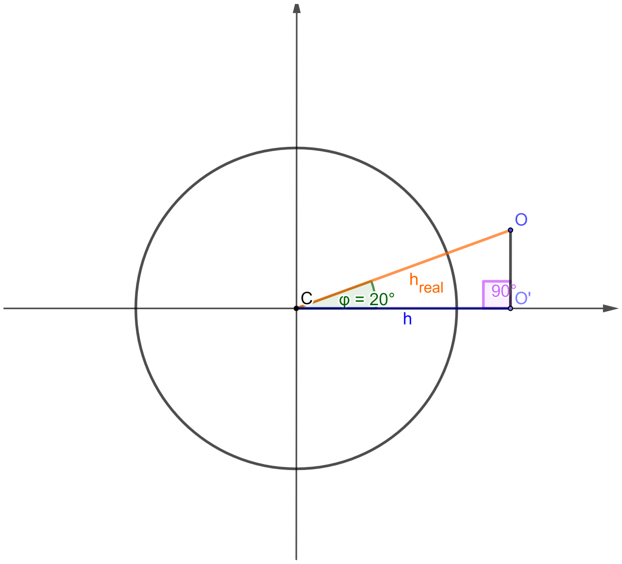

Figure 3.3: Sketch depicting the real height (h_{real}) versus the measured height (h). The measured height is the projection of the real height on the plane of sight. φ is the longitudinal angle between the real direction of propagation and the limb plane. The point C represents the centre of the Sun.

3.3.3 Solar Rotation Effect

In this section I assess how Sun's rotation affects the measurements of the prominence height during its propagation. It is possible to demonstrate that the contribution of solar rotation compared with the prominence velocity can be considered negligible. As indicated by Shrijver et al. 2008 [105], for a filament located at a geometric height $h(t)$ above the photosphere, the apparent velocity $\dot{h}$ to the limb due to the perspective change caused by the solar rotation is approximated by a term associated with the actual prominence velocity during its movement and a term contingent upon the solar rotation at that specific latitude. In other words, if we assume that during the propagation of a prominence, the Sun rotates by an angle α, then the prominence moves in a circular path with a radius equal to the measured height h, around the North of the Sun. However, since the prominence is also increasing in height, there will be an additional factor accounting for its intrinsic motion that affects the measured height, see Figure 3.5.

If we call $H(t)$ the real distance of the prominence from the centre at a certain instant of time t, the velocity of the prominence moving from its previous position (for instance, the limb) to O' is referred to as $\dot{H}$. In this time the Sun rotates by an angle α. Thus, the apparent velocity $\dot{h}$ relative to the solar limb induced by the solar rotation is:

$$\dot{h} = \dot{H} + \dot{\overline{OM}} \tag{3.7}$$

In the small angle approximation we can use the triangle $O'MO$ to infer the quantity OM. If we assume that the angle $O'\hat{M}O$ is 90°, then $M\hat{O}'O$ is equal to α:

$$\begin{aligned}
\overline{OM} &= \overline{OO}' \sin\alpha \approx \overline{OO'} \cdot \alpha \\
\overline{OO}' &= \overline{NO} \sin\alpha \approx \overline{NO} \cdot \alpha \\
\overline{NO} &= \frac{\overline{NO'}}{\cos\alpha} \approx \overline{NO'} = (R_\odot + H)
\end{aligned}$$

Thus, substituting $\overline{OM} = (R_\odot + H) \cdot \alpha^2$ and the derivative gives

$$\dot{h} = \dot{H} + 2(R_\odot + H)\alpha\dot{\alpha} + O(\alpha^2) \tag{3.8}$$

As already said, α is the variation in longitude with reference to the limb and $\dot{\alpha}$ the velocity at

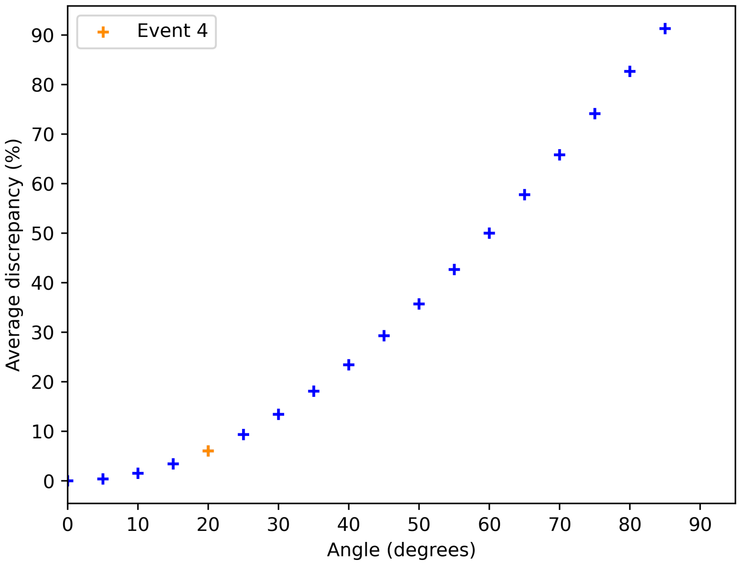

Figure 3.4: Discrepancy between measuring a prominence at a certain angle from the limb. The orange cross represent the value obtained with an angle of 20 degrees for which I found a percent error value of 6.03 %.

which it varies, so approximately the angular velocity of the Sun at that latitude. Note that both α and the height of the prominence H are functions of time but I neglect the term in α^2 in the small angle approximation. The Sun's rotational velocities differ depending on its latitude (Section 1.1.1), i.e. it rotates more rapidly at the equator than at the poles. Roudier et al., 2018 [99] pointed out that an approximate value of this rotation can be calculated with the following formula[3] :

$$\omega(\phi) = 2.86 + 0.00505 sin\phi - 0.549 sin^2\phi + 0.0015 sin^3\phi - 0.173 sin^4\phi \tag{3.9}$$

Where ϕ represents the latitude of the point and ω is given in microradians per second (¯rad/s). For example, if our prominence propagates at an approximate latitude of 30°, the angular velocity of the Sun at that specific latitude amounts to 2.71 μrad/s. Therefore, if we consider, for instance, "Event 6" and calculate the rotational velocity using formula 3.9, assuming a small value for α of around 2 degrees[4], we found that the relative velocity is approximately 0.14 km/s. This value is notably lower than the prominence's initial velocity. The situation remains quite analogous even when considering prominence eruptions occurring at the equator, such as in "Event 4"; the assumption can still be reasonably regarded as valid.

3.4 Fit procedure

An erupting prominence typically undergoes a multi-phase kinematic evolution, which includes three distinct stages: the slow-rise phase, where the prominence ascends with a constant velocity; the acceleration phase, characterized by an increase in speed; and, in some cases, the propagation phase, during which the prominence maintains an approximately constant velocity. This is discussed in Section 1.4.6.

Earlier studies (e.g., Schrijver et al., 2008 [105]) have shown that given the nature of the function that best fits the height-time profile of the acceleration phase it is possible to extract information on the initiation mechanism of the eruption.

---

[3] This formula is obtained by fitting the differential velocity profile in sin(ϕ). For more details see Roudier et al., 2018 [99].

[4] Since the Sun rotates at 2.71 km/s at a latitude of 30°, I estimated that in 2 hours and 30 minutes it rotates less than 2°.

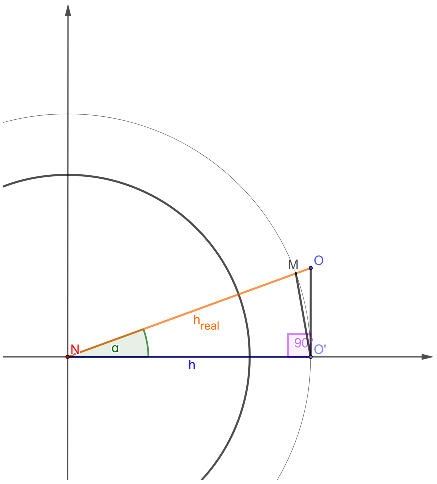

Figure 3.5: Sketch depicting the deflection between the measured height and the real height due to the solar rotation. M marks the position of the prominence due to the rotation of the Sun of an angle α. O points the real height due to the prominence motion and the rotation, and O' the projection in the POS.

In particular from the power-law exponents we can investigate different eruption mechanisms as pointed out by Mierla et al, 2013 [74]:

- The power-law exponent ($m = 2.5$) provides the best fit for the catastrophe model scenario as proposed by Priest and Forbes in 2002 [94];
- A parabolic profile ($m = 2$) effectively characterizes the CME rise in a breakout-model simulation, as demonstrated by Lynch et al. in 2004 [68];
- An exponent of 3 is more aligned with the torus-instability scenario, especially when a sufficiently large initial perturbation is applied, as observed by Schrijver et al. in 2008 [105];
- An exponential rise has been observed in a three-dimensional flux-rope subject to a helical kink instability, as studied by Török, Kliem, and Titov in 2004 [121], and Török and Kliem in 2005 [120];
- The exponential rise also holds true for the torus (expansion) instability, which initially follows a $\sinh(t)$ function similar to a pure exponential, as described by Kliem and Török in 2006 [57]).

This study primarily centers on identifying the initiation mechanism of eruptive prominences, specifically selecting the model that best characterizes the acceleration phase of the prominence. To achieve this, it is essential to distinguish between the three main phases mentioned earlier. The following section outlines the procedure for making this distinction.

3.4.1 Slow rising phase and the beginning of the acceleration phase

To determine the time when the acceleration phase started (t_0), I followed the procedure described in Mierla et al. 2013 [74]. The height-time profile of the feature was fitted with a power-law function of the type

$$h = h_0 + v_0(t - t_0) + a_0(t - t_0)^m \tag{3.10}$$

The parameters represent the following quantities: h_0 corresponds to the initial height of the prominence, measured in kilometers [km], v_0 represents the initial velocity perturbation resulting from destabilization during the initiation phase. It is measured in kilometers per second [km/s], a_0 is a parameter that characterizes the rate of change of acceleration [km s^{-m}], t_0 denotes the initial time [s], before which the acceleration can be considered negligible and is set to zero. Finally, m represents the coefficient of the power law. In this way it is possible to extract the coefficient m that minimize the chi square and the optimized initial time (t_0). Consequently, all the points preceding t_0 constitute the slow rising phase of the eruption, while the points after t_0 represent the acceleration phase.

Once the initial time is constrained, I fit again a power-law with 3 degrees of freedom, i.e. I fixed the time t_0, and the coefficient m with the best-fit parameters found previously. I did this because the fitting procedure with 5 degrees of freedom introduce larger uncertainties on the parameters. Afterwards, I can compare the results obtained using two additional functions where the value of t_0 is also kept constant: An exponential-law fit with 4 degrees of freedom,

$$h = ae^{d(t-t_0)} + b(t - t_0) + c \tag{3.11}$$

and a parabolic profile (3 degrees of freedom) which characterizes a constant acceleration growth:

$$h = a(t - t_0)^2 + b(t - t_0) + c \tag{3.12}$$

The three functions described above were employed to fit the early phase of the eruptive prominence using a script in python. This allows to determine the best fit and the associated initiation mechanism.

3.4.2 Propagation phase

After the acceleration phase, most erupting filaments rise with an almost-constant velocity (e.g. Kahler et al. 1988 [54]; Joshi and Srivastava 2007 [53]). This defines the propagation phase where the height of the prominence is observed to increase linearly. Due to the large field of view of the FSI instrument it was possible to track the eruptive prominence until high distances from the Sun's center. This means that it was possible to observe also the propagation phase. The start of the propagation phase was considered to be right after the acceleration phase ended. This was identified through the following procedure.

When the previous analysis, which considered all data points, did not yield satisfactory results or when the presence of a change in slope after the acceleration was evident, a stepwise approach was taken. One or more of the last data points were sequentially excluded from the fit using a 5-parameter free power-law function. In cases where there were at least 3 remaining data points, a linear fit was applied to model the presumed propagation phase. The aim was to identify an interval that minimized the chi-square value for the power-law function in the early phase while simultaneously providing a good fit for the linear phase. The time corresponding to the transition point within this interval was then determined as the final time for acceleration.

3.4.3 Chi-square Goodness of fit test

To determine the optimal fit, I employed the the reduced chi-square statistic, which gauges how well a statistical model aligns with a set of observations. The χ^2_ν value, computed using formula 3.13, resembles a normalized sum of squared deviations between observed and theoretical frequencies:

$$\chi^2_\nu = \frac{\chi^2}{\nu} \qquad \chi^2 = \sum_{i=1}^{N} \frac{(O_i - E_i)^2}{\sigma_i^2} \tag{3.13}$$

Here, ν represents the degrees of freedom of the data, O_i represents the observed value, E_i represents the expected value, and σ_i denotes the associated uncertainty of the observed one. If those are independent and standard normal random variables, then they are supposed to follow a chi square distribution χ^2 with mean equal to the number of independent data values (i.e. the degree of freedom df of the models) given from the number of data minus the number of fitting parameters, and variance $2df$. Considering the reduced chi square, we expected 1 for the mean, and 2 for the variance.

In general, chi-square value much greater than 1 ($\chi^2_\nu \gg 1$) suggests a poor fit of the model. A chi-square value greater than 1 ($\chi^2_\nu > 1$) indicates that the model has not adequately represented the data, or that the estimation of error variance was too low. Ideally, a chi-square value close to 1 ($\chi^2_\nu \approx 1$) signifies that the agreement between observations and estimates aligns well with the error variance. Conversely, a chi-square value less than 1 ($\chi^2_\nu < 1$) suggests that the model is "over-fitting" the data, potentially fitting noise inaccurately or overestimating the error variance.

The chi-square test is a hypothesis test that permits conclusions about population distribution based on a sample. Like all hypothesis tests, it assesses both null and alternative hypothesis:

$H_0 =$ The population follows the specified model.
$H_1 =$ The population does not follow the specified model.

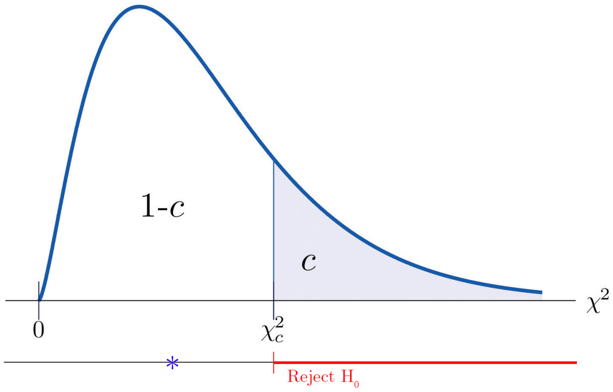

Figure 3.6: Critical value of Chi-Square Distributions. The blue area represents c, the significance level, 1-c denotes the confidence level, and χ^2_c the critical value . The '*' represents a value which falls below χ^2_c. The red line represents the values for which we can reject the null hypothesis. Image adapted from Introductory Statistics [2].

To assess the goodness of the fit, one needs to ascertain the degrees of freedom and specify the significance level, c, a predetermined threshold for statistical significance, see Figure 3.6. This threshold denotes the maximum acceptable risk of a false positive conclusion. For example, the *df* equates to the number of data points minus the model's parameters (2 for linear, 3 for quadratic, etc). Depending on *df* the corresponding distribution varies approaching a Gaussian for larger samples. The significance level is often set to 0.05. This value implies that there is a 95% (1-c) probability that the confidence interval contains the true parameter value. To this value corresponds a predefined *critical value* for the variable χ^2 which defines the boundary of the rejection region. The latter can be determined from chi-square critical value tables (See Figure 4.48 in Appendix) or software.

When the computed χ^2 value surpasses the critical value, it falls on the rejection interval (red line in Figure 3.6). In this case, the discrepancy between the observed and expected distributions is statistically significant ($p < c$). The symbol p represents the p-value, indicating the likelihood that the data would occur under the null hypothesis of the statistical test. Geometrically it represents the blue area between the computed chi value and the tail. Consequently, ($p < c$), enables rejection of the null hypothesis and support for the alternative hypothesis.

If the χ^2 value falls below the critical value (blue '*' in Figure 3.6), the gap between observed and expected distributions lacks statistical significance ($p > c$). In such cases, the data does not warrant null hypothesis rejection and does not provide backing for the alternative hypothesis.

3.5 Kinematic quantities

Calculations of the velocity and acceleration of an erupting prominence yield valuable insights into the forces acting on the prominence and the mechanisms involved in the eruption. These insights can be derived in two different ways. The first involves the derivation of the velocity and the acceleration from the measured height through jHelioviewer. The second involves the derivation of the same quantities from the heights obtained through the fitting process (e.g., from the best-fit parameters). For both, the velocity is determined as follows:

$$v_i = \frac{h_{i+1} - h_i}{t_{i+1} - t_i} \qquad \sigma_{v_i} = \frac{\sqrt{\sigma_{i+1}^2 + \sigma_i^2}}{t_{i+1} - t_i} \tag{3.14}$$

where 'h_i' represents the height [km], 'σ_i' the uncertainty in height, and 't_i' the time [s] of the observations.

These quantities are typically affected by significant uncertainty. Thus, when it is feasible, I will report the weighted average calculated as follow:

$$\bar{v} = \frac{\sum_{i=1}^{N} v_i/\sigma_{v_i}^2}{1/\sum_{i=1}^{N} \sigma_{v_i}^2} \qquad \sigma_{\bar{v}} = \sqrt{\frac{1}{\sum_{i=1}^{N} 1/\sigma_{v_i}^2}} \tag{3.15}$$

In both scenarios, the calculation remains consistent, with the only difference being the replacement of the observed height with the value of height obtained from the fitting procedure. In this case, it was necessary to compute the uncertainties in the heights derived from the fit. Using the best fit and disregarding correlations or assuming independent variables, we can apply the following formula:

$$\sigma_y \approx \sqrt{\left(\frac{\partial y}{\partial a}\right)^2 \sigma_a^2 + \left(\frac{\partial y}{\partial b}\right)^2 \sigma_b^2 + \left(\frac{\partial y}{\partial c}\right)^2 \sigma_c^2 + \dots} \tag{3.16}$$

Where σ_y is the standard deviation of the function y (i.e. parabolic, power-law, etc ...) a, b, c, etc... are the fit parameters and σ_a, σ_b, σ_c, etc ... are the standard deviation associated with the parameters. Regarding acceleration, the procedure remains analogous, with the height quantities replaced by velocity.

Chapter 4

Results and Interpretation

The methodology employed for studying the selected eruptive prominences aligns with the extensive discussions in Chapter 3. This chapter commences by presenting the measurement of the events and supplementary images collected for its analysis. Subsequently, it delves into a discussion of the initiation mechanisms, accompanied by the presentation of interpolation results for all the gathered data. Additionally, for events marked by a substantial volume of data, a low-cadence analysis has been incorporated, which entail the removal of certain data points simulating the measurement procedure at low frequency. This approach enables us to ascertain whether both types of analysis yield consistent conclusions and offers insight into the potential enhancements that increased data frequency can offer for this analysis. Then, the discussion delves into the kinetics of these events, offering insights into their speed and acceleration. Additionally, we explore the potential impact of the solar corona on their trajectory, which may result in deviations from the expected radial propagation pattern.

4.1 Event 1

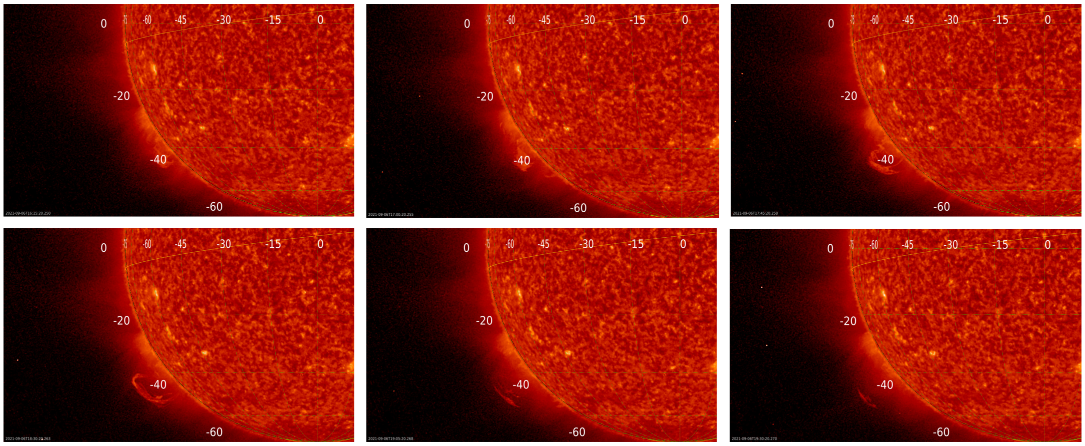

Figure 4.1: Event 1 observed on 2021-09-06. Sequence of images at increasing time.

The first event under study ("Event 1") is a small-scale prominence eruption with loop-like morphology which occurs in the South-East of the Sun (see Figure 4.2b) on September 6th, 2021, as shown in Figure 3.1a. This event became visible at approximately 16:15 UT starting at a height of 1.09 $R_\odot$, reaching a maximum value of 1.22 $R_\odot$ before disappearing at around 19:30 UT. In Figure 4.1 it is possible to observe how the prominence evolves in time.

The measurement procedure of the prominence follows what was already mentioned in Section 3.2. I start from the last frame in which the leading point of the loop was visible (Figure 4.2a), and then I track the same point (in terms of distance and position angle) backwards. The measurement was performed three times for each image. In Figure 4.2a the black arrow indicates the direction of propagation of the prominence. This propagation is essentially radial, as indicated by the slight variation in the position angle (theta) throughout the entire propagation process. These images are provided with a cadence of five minutes.

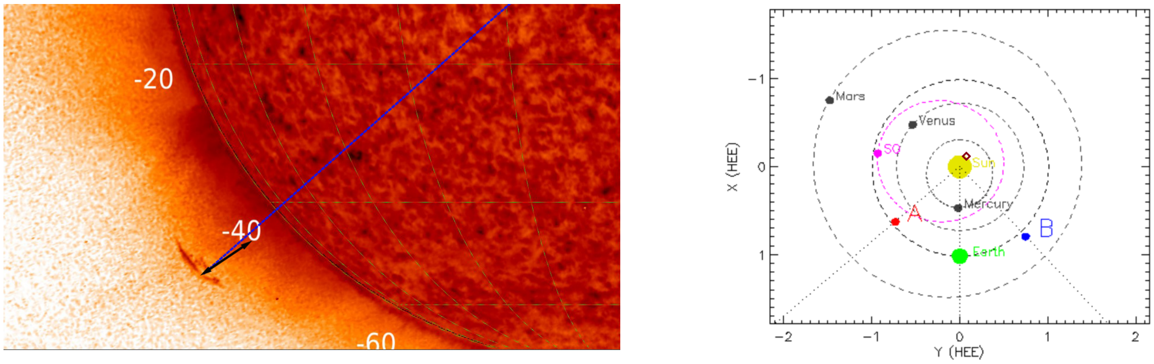

(a) Event 1 observed at 19:30:20 UTC. The black arrow points the leading point of the prominence under study following the direction of the measurement. The blue dashed line indicates the radial direction of the leading point.

(b) Event 1 relative position at 16:30 UT. The red rhombus roughly indicates the location of the solar eruption. For more details refer to Section 2.4.2.

Figure 4.2: Event 1 observed on 2021-09-06.

4.1.1 Initiation mechanisms

High cadence analysis The averaged distance and position angle over time are presented in Figure 4.3. The “stepped” appearance in the height-time plot (to the left) is due to the presence of different data at the same height, that is, the frequency at which the images were collected exceeds that at which the prominence grows in height. From the PA-time plot (to the right), it is possible to observe that the angle remains nearly constant, varying less than 1 degree. This confirms that the prominence propagates almost radially. The raw data used and the average values are presented in Table 4.7 in the Appendix.

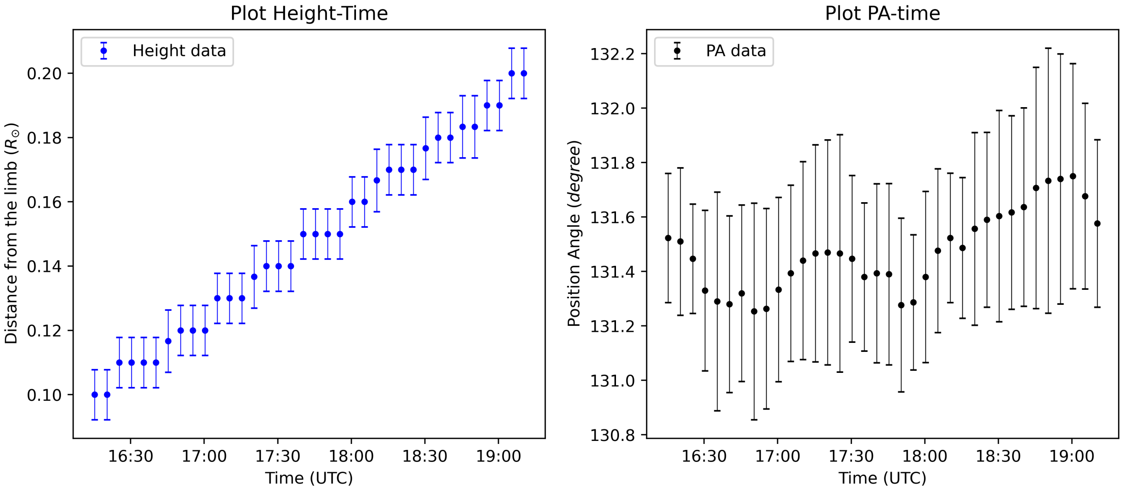

Figure 4.3: Event 1 height-time and PA-time plots. On the *left* the averaged height and on the *right* the averaged angular position of the prominence, both as a function of time.

The initial phase of the analysis involves identifying the onset of the slow-rise phase and the beginning of the acceleration phase (t_0) for the erupting prominence. This is done by finding the optimized time for the transition between these phases. The procedure is the one outlined in Section 3.4.1. The various efforts are presented in Table 4.1. The power-law yielded a coefficient of $m = 1.2 \pm 5.4$

with $\chi^2_\nu = 0.115$ and $t_0 = 9690 \pm 2614$ s. Thus, the onset happens at 18:51 UT to a distance of about 0.18 $R_\odot$ from the limb. Shortly thereafter, the prominence disappears.

Given that all the chi-square values are quite small (significantly less than 1), the uncertainties associated with the height points are larger than the discrepancies in the data. This suggests that the models might be overfitting the data. Therefore, I have selected the best-fit model as the one that minimizes the chi-square value.

Initial time	Final time	Input t_0	Best t_0	m	χ^2_ν
16:15	19:10	16:40	16:40	1.29	0.164
16:15	19:10	17:05	17:04	1.97	0.201
16:15	19:10	17:30	17:35	1.00	0.188
16:15	19:10	18:20	18:19	5.44	0.157
16:15	19:10	18:45	18:51	1.23	0.115
16:15	19:10	19:05	19:05	2.00	0.285

Table 4.1: EVENT 1 MINIMIZING χ^2. “Initial time” is the time of the first data measurement, “Final time” is the time when the acceleration phase is supposed to end, “Input t_0” is the input time to the python script and best t_0 is the best estimator for it. m and χ^2_ν are the exponent and the reduced chi square values respectively. The yellow row is the one that minimizes the chi square.

At this point, I employed various functions for fitting: the power-law with fixed m and t_0, the parabolic, and the exponential, following the procedure outlined in Section 3.4. Additionally, I applied linear regression since the data seemed to exhibit a linear trend. The outcomes are presented in Figure 4.4. All the functions appear to represent the data quite well. The power-law yielded $\chi^2_\nu = 0.108$. The parabolic function provided a slightly lower value of $\chi^2_\nu = 0.112$. The exponential and the linear function yielded the same chi-value as the power-law ($\chi^2_\nu = 0.115$).

Upon inspecting Table 4.4b, it becomes apparent that the parameter a associated with the exponential functions exhibit large uncertainties. In the case of the parabolic function, the parameters are precise, but the coefficient a is close to zero, as is the case for d in the exponential function and a in the power-law. This may be attributed to the fact that in all instances, the coefficients related to acceleration or its variations are near zero (a and d). All of these models seem to replicate a linear trend. This examination demonstrates that even though the chi-square values for the variables are low, especially for the power-law fit, the optimal fit results from employing linear regression. This conclusion gains additional support from the small associated parameter uncertainties, as can be seen in the column “Linear” on the same table.

The p-values are all approaching one, making it impossible to obtain statistically significant information about the quality of the fit, see Section 3.4.3.

The p-value reflects the probability that the observed data align with the null hypothesis, which assumes that the regression model used represents the data accurately. However, when the p-value is close to one, it implies a lack of statistical significance. Consequently, we cannot either confirm or reject the null hypothesis. See Section 3.4.3 for a detailed explanation.

LOW CADENCE ANALYSIS Through the omission of certain data points, it becomes feasible to replicate the outcomes that would emerge at a reduced frame rate, specifically a cadence of 20 minutes. This particular cadence was selected as it eliminates the instances of points sharing the same height, while still ensuring an adequate number of data points. The data selected for this particular analysis has been highlighted using a distinct color (Table 4.7 in the Appendix).

The procedure follows the same steps as described earlier. The power-law with 5 degrees of freedom returns $m = 1.55$ with t_0 at 18:50 UT with $\chi^2_\nu = 0.070$, but with large uncertainties. Next, I applied the various fitting functions to the data obtaining that all the functions appear to closely reproduce the data, as depicted in Figure 4.5a. Once again, the power-law, the parabolic fit and the exponential fit provide precise parameters, but they indicate an acceleration close to zero. In conclusion, the linear function ($\chi^2_\nu = 0.232$) continues to be the best-suited function for describing the data. Thus, conducting an analysis with a reduced image cadence has allowed us to estimate results that align closely with those obtained in the high-cadence analysis. The fit parameters associated with the best fit are found to be higher in value and less accurate compared with the high cadence analysis.

A linear fit does not offer any insights into the underlying trigger mechanism for the eruption, primarily because no models in the existing literature have been proposed that account for constant velocity alone. The various eruption mechanisms are discussed in Section 1.5

4.1.2 Kinematic analysis

I investigated the velocity and the acceleration of the prominence during its propagation, both in the high-cadence and low-cadence analysis. I calculated these quantities using the two different methods outlined in Section 3.5: I calculated the velocity from the measured heights (1) and from the heights performed with the best fit function (2). The second method allows to obtain quantities close to the former, but with less uncertainty. Thus in the analysis I report the latter. The results can be observed in Figure 4.6. The first panels represents the height of the prominence in [km] with the linear fit. In the middle and lower graphs, the velocity and the acceleration are shown.

The prominence is observed to move with an averaged constant velocity of:

$$v_{high} = 6.54 \pm 0.57 \text{ km/s} \qquad v_{low} = 6.73 \pm 0.61 \text{ km/s} \tag{4.1}$$

These values are compatible with the b coefficients (slope) of the linear functions (4.4b, 4.5b), i.e. $b = 6.540 \pm 0.090$ km/s for the high cadence analysis and 6.73 ± 0.21 km/s for the low cadence one.

Therefore, we can observe that the averaged acceleration is approximately zero:

$$a_{high} = 0.0 \pm 2.7 \text{ m/s}^2 \qquad a_{low} = 0.00 \pm 0.71 \text{ m/s}^2 \tag{4.2}$$

This confirms that the acceleration phase is not observed and the prominence just moved at a constant speed during its propagation.

The cadence is expected to have an impact on the parameters of the fitting function, especially when there are missing data points that could otherwise help constrain the curvature of the height-time plot. Consequently, given the observed linear trend, I anticipated similar results for both analyses. Indeed, the low cadence analysis yielded values similar to those obtained from the high cadence data. However, the low cadence values are characterized by lower uncertainty. This is likely attributable to the smaller dataset in comparison to the larger dataset in the case of high cadence, which reduces the steps-like appearance.

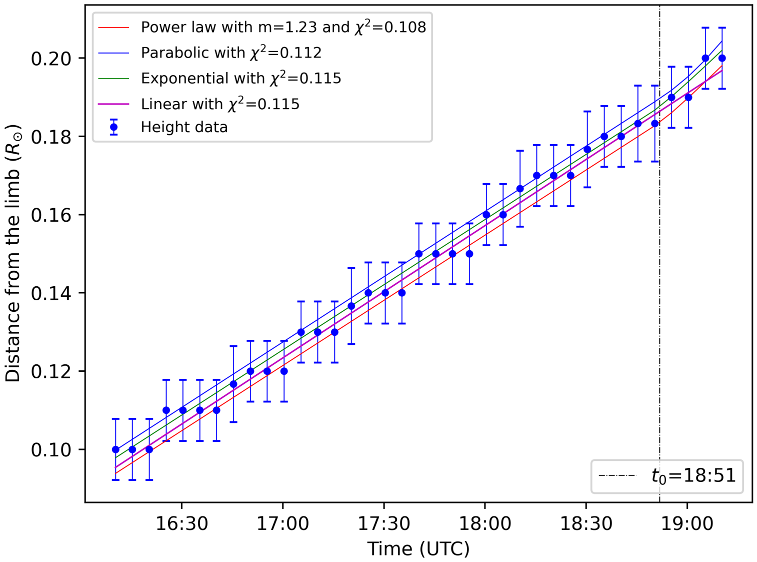

(a) Event 1 fitted functions. This height-time plot shows the functions fitted on the data during the analysis. Shifting the parabolic and the power-law functions by 0.002 $R_\odot$ helped distinguish the models on the height-time plot.

	Power law	**Parabolic**	**Exponential**	**Linear**
a	0.040 ± 0.020	0.0025 ± 0.0015	92190 ± 1238446	-
b	6.45 ± 0.11	6.45 ± 0.11	6.44 ± 0.11	6.540 ± 0.090
c	129818 ± 602	129864 ± 593	129759 ± 657	67046 ± 601
d	-	-	0.0001 ± 0.0012	-
χ^2_ν	0.108	0.112	0.115	0.115
df	34	34	33	35
p	0.999	0.999	0.999	0.999

(b) Event 1 fit parameters. The employed functions are as follows: the power-law $a(t-t_0)^{1.23}+b(t-t_0)+c$, the parabolic $a(t-t_0)^2+b(t-t_0)+c$, the exponential $ae^{d(t-t_0)}+b(t-t_0)+c$ and the linear $bt+c$. For the power-law and the parabolic profile a represents respectively the variation in the acceleration [km/s$^{\mathrm{m}}$], and the acceleration itself [km/s^2]. For all of them, b is the averaged velocity of the prominence [km/s] and c the initial height of the prominence [km]. For the exponential, d [1/s] combined with a [km] is another coefficient that represents the variation in the acceleration. χ^2_ν is the reduced chi square, df the degrees of freedom and p the p-value.

Figure 4.4: Event 1: fit results. The resulting analysis concerns the high cadence data.

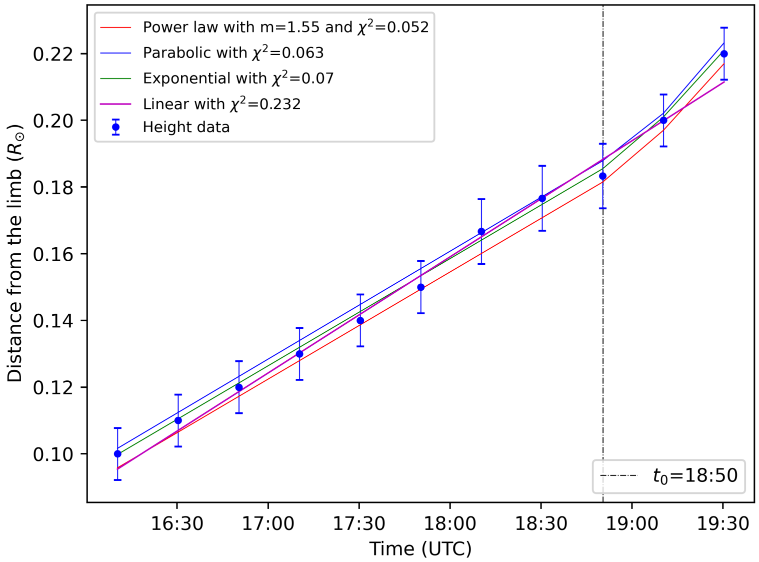

(a) Event 1 fitted functions. This height-time plot shows the functions fitted on the data during the analysis. Shifting the parabolic and the power-law functions by 0.002 $R_\odot$ helped distinguish the models on the height-time plot.

	Power law	**Parabolic**	**Exponential**	**Linear**
a	0.040 ± 0.010	0.00167 ± 0.00030	37432 ± 47795	-
b	6.21 ± 0.14	6.25 ± 0.14	6.21 ± 0.16	6.73 ± 0.21
c	128398 ± 805	128642 ± 794	128367 ± 963	67072 ± 1478
d	-	-	0.00021 ± 0.00021	-
χ^2_ν	0.052	0.063	0.070	0.232
df	8	8	7	0
p	0.999	0.999	0.999	0.999

(b) Event 1 fit parameters. The employed functions are as follows: the power-law $a(t-t_0)^{1.55}+b(t-t_0)+c$, the parabolic $a(t-t_0)^2+b(t-t_0)+c$, the exponential $ae^{d(t-t_0)}+b(t-t_0)+c$ and the linear $bt+c$. For the power-law and the parabolic profile a represents respectively the variation in the acceleration [km/s$^{\mathrm{m}}$], and the acceleration itself [km/s^2]. For all of them, b is the averaged velocity of the prominence [km/s] and c the initial height of the prominence [km]. For the exponential, d [1/s] combined with a [km] is another coefficient that represents the variation in the acceleration. χ^2_ν the reduced chi square, df the degrees of freedom and p the p-value.

Figure 4.5: Event 1: fit results. The resulting analysis concerns the low cadence data.

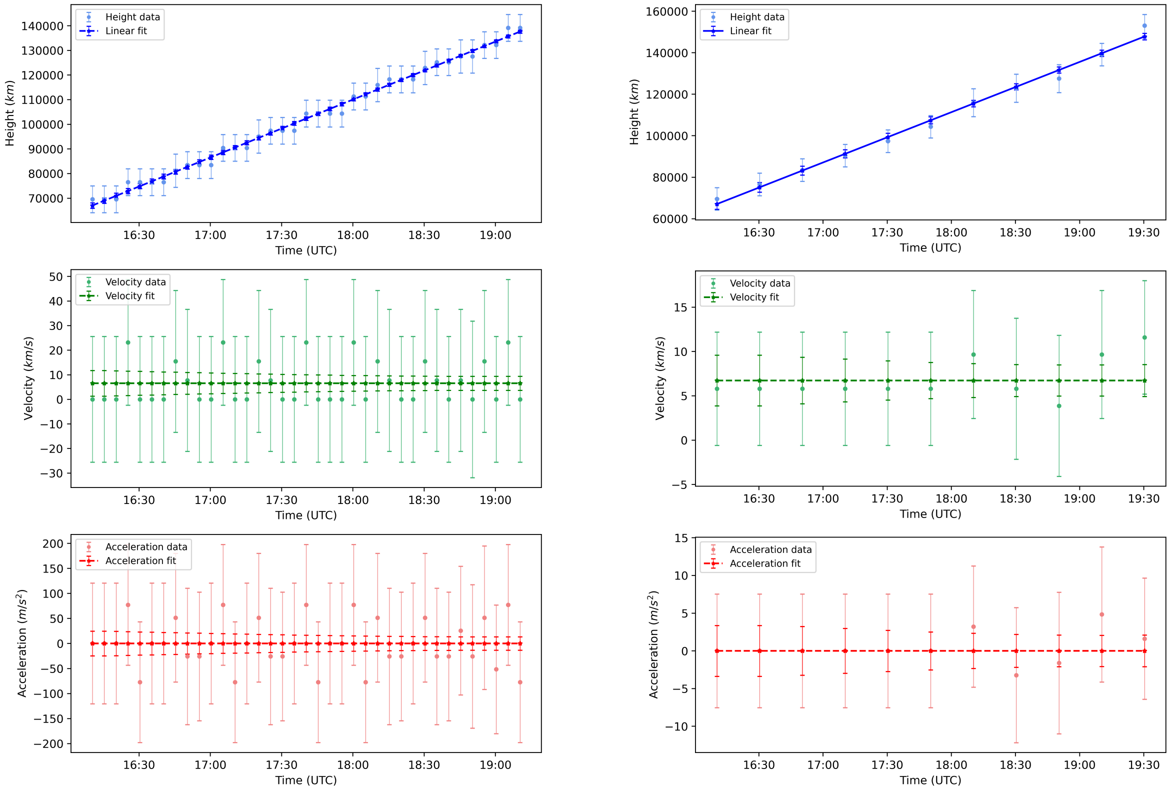

(a) Event 1. High cadence kinematic plot.

(b) Event 1. Low cadence kinematic plot.

Figure 4.6: Event 1 kinematics. Distances from the limb (height) in [km] are shown (*top*). "Velocity" (green dots) is calculated from the differential of the height data in time [km/s]. The green dashed line represents the differential calculated from the linear function called "Fitted velocity" (*middle*). "Acceleration data" are calculated from the differential of velocity in time [m/s^2], and the red dashed line represents the "Fitted acceleration" differential calculated from the fitted velocity (*bottom*).

4.1.3 Influence of the surrounding corona

A burst of light at the eruption site, or the presence of current sheets, plasmoids, etc. could potentially indicate the involvement of the magnetic reconnection within the erupting prominence (see Section 1.2.6 for more details). However, looking at the sequence of FSI 304 images it was not possible to clearly identify the footpoints of the prominence. They appear to be arched slightly behind the Sun, while the prominence grows and propagates outwards, becoming clearly visible from the Solar Orbiter point of view. The SDO/AIA 304 did not capture the eruption, and STEREO-A/EUVI 304 was also unable to observe the footpoints. As a result, the site of the eruption remained not clearly observed. This may signify that the eruption was well behind the solar limb which may explain the fact that the acceleration phase was not observed in the measured data points. As a result, the constant velocity I measured could be consistent with the propagation phase of the eruption

To analyze the corona surrounding the eruption, I also looked at the images recorded by FSI 174 and at the PFSS extrapolation provided in jHelioviewer (for a short description of the PFSS method see Section 1.2.4). All these elements are visible in Figure 4.7. The PFSS model suggests that the prominence is surrounded by magnetic loops, a conclusion that is also supported by observations in FSI 174. When tracking the prominence during its propagation, it becomes evident that a magnetic field loop undergoes rearrangement, appearing to confine the erupting filament. This phenomenon is illustrated in the two distinct observations captured by FSI 174 in Figure 4.8. The light-blue arrow points the shielding loop, while the blue arrow points to the prominence when it becomes visible.

.

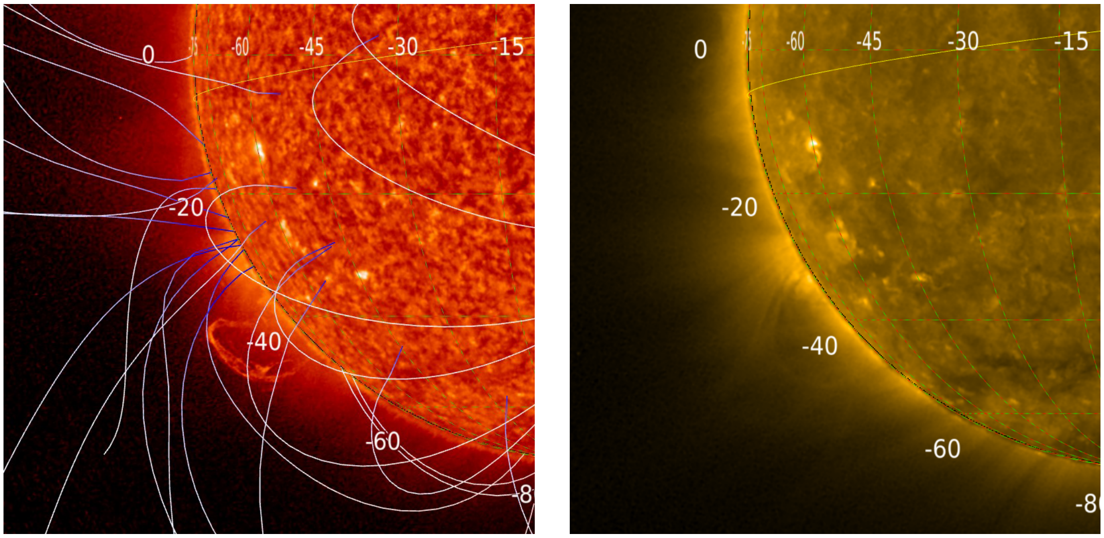

(a) FSI 304 Å. **(b)** FSI 174 Å.

Figure 4.7: Event 1 on 2021-06-09 18:35:20 UTC . The different channels through which EUI can observe the Sun and The PFSS model of the solar magnetic field lines (*left*).

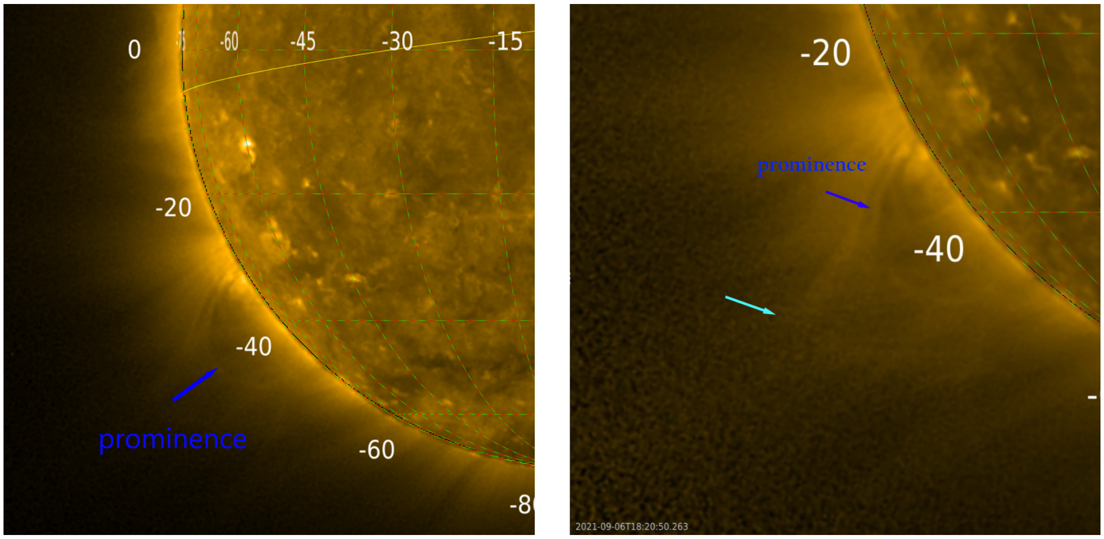

Figure 4.8: Event 1 on 2021-09-06 in FSI 174 Å. The filament is quite faint, but an overlying structure, which seems to be shielding the prominence site is clearly observed (*left*). In the successive images with the eruption (*right*) one can observe the aforementioned loop gently rearranging, allowing the prominence material to escape.

4.1.4 Discussion

The analysis conducted seems to agree with the fact that a linear model best characterizes the eruption. It means that the forces acting on the filament balanced out and the eruption is moving at a constant speed. The impulsive acceleration of the prominence during its eruption is not always observed, as reported by Mierla et al., in 2013 [74]. This implies that mechanisms involving the release of large amounts of energy are not always necessary for the eruption of a prominence, such as magnetic reconnection or the development of kink-type instabilities. Fan and Gibson in 2007 [35], delved into the study of eruptive phenomena that did not exhibit signs of impulsive energy release. The eruptions under study exhibited a structure similar to what was observed for this event, namely, an anchored flux rope confined by an external arcade. From their simulations, it was observed that the flux rope can sometimes become unstable before it has stored enough energy and twist for the potential development of a helical kink instability, displaying a more planar growth instead, which is compatible with the torus instability. Additionally, Mierla et al. in 2013 [74] demonstrated that some eruptions may not be consistent with an immediate acceleration due to magnetic reconnection but rather could be swept away as part of a large-scale relaxation of the coronal magnetic field. Despite the small-scale nature of this event, it was challenging to clearly observe its acceleration, making it difficult to associate it with a single initiation mechanism. If this were the case, it could suggest that the initiation of these phenomena without clear signs of magnetic reconnection is indeed possible. However, another possible explanation exists: the acceleration phase might not have been observed due to its propagation occurring on the backside, and only the propagation phase was captured.

The comparison between the high frequency and low frequency analysis has allowed us to identify the influence of the cadence on the estimation of the kinematics of the eruptive phenomena. In fact, it is crucial to limit the fitting parameters of the kinematic profile, which is impacted by the cadence of the instruments employed to estimate these coefficients. This has been investigated by several authors (Byrne et al., 2013 [18]; and Vashishtha et al. 2023 [124]). The results obtained for both frequency levels align quite well in terms of initial time and best model fitting the data. From this specific event, I was able to compare the velocity of the prominence under both high and low cadence conditions. The low cadence analysis provides fit parameters with higher values and less precision. However, when considering the averages from the individual data points, it becomes apparent that the velocity extracted from the low cadence data is not only higher but also more accurate than the estimate from high cadence data. The higher value of speed in the low cadence analysis could be attributed to the fact that low-frequency data eliminates the ‘steps’, thereby reducing the discrepancy between measured values and the mean value.

4.2 Event 2

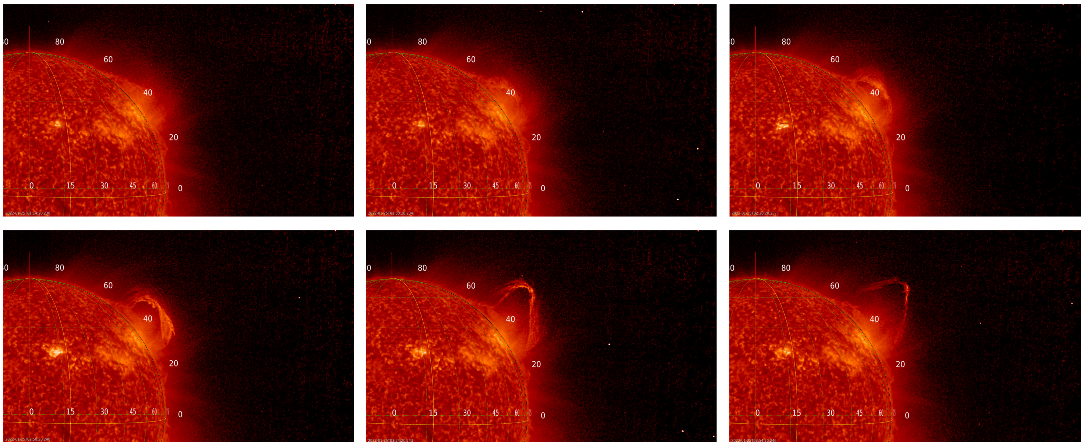

Figure 4.9: Event 2 observed on 2022-01-25. Sequence of images at increasing time.

The second event under study ("Event 2") is another loop-like prominence eruption occurring at the North-West of the Sun (see Figure 4.10b), on January 25th, 2022 (Figure 3.1b). It starts around 01:14 UT at a height of 0.04 $R_\odot$ from the limb and reaches the maximum height of 0.45 $R_\odot$ above the limb at 03:54 UT. After that there is a gap of 63 minutes between the frames and so it is not observable anymore. In Figure 4.9 it is possible to observe how the prominence evolves in time.

The measurement procedure of the prominence follows what already mentioned in Section 3.2. I start from the last frame in which the leading point of the loop was visible (Figure 4.10a), and then I track the distance and position angle of the leading point of the prominence backward, three times for each image. The black arrow in the figure points to the direction of propagation of the prominence. The prominence is seen to propagate almost radially, as indicated by the slight variation in the position angle throughout the entire propagation. The images are provided with a cadence of four and six minutes.

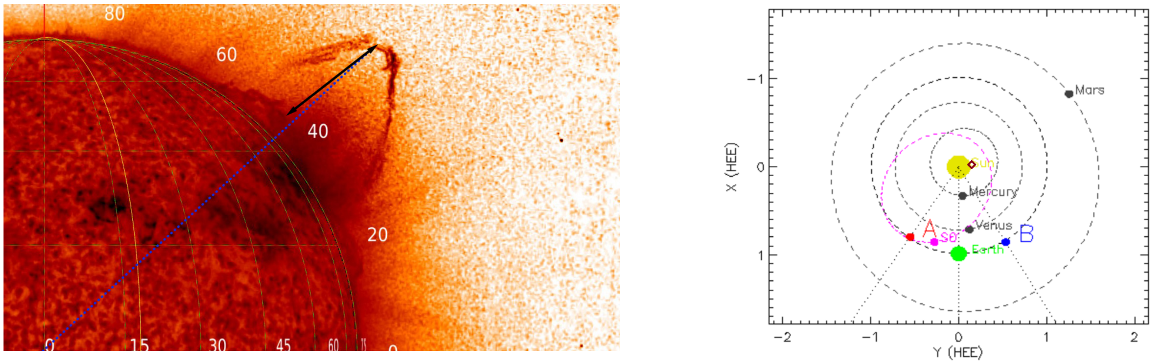

(a) Event 2 observed on 2022-01-25 03:54:50 UTC. The black arrow points the leading point of the prominence under study following the direction of the measurement. The blue dashed line indicates the radial direction of the leading point.

(b) Event 2 relative position at 02:00 UT. The red rhombus roughly indicates the location of the solar eruption. For more details refer to Section 2.4.2.

Figure 4.10: Event 2 observed on 2022-01-25.

4.2.1 Initiation mechanisms

HIGH CADENCE ANALYSIS The averaged distance and position angle over time are presented in Figure 4.11. Although the prominence was seen to rise at 01:14 UT, the specific point that was tracked during the measurement process becomes noticeable starting from 02:00 UT. As a result, the earlier point has been omitted from the analysis. The left panel in Figure 4.11 shows the height-time plot where it is possible to observe three different trends. In particular, it reveals a distinct pattern in the last (approximately six) data points, resembling a constant velocity. This may be indicative of the propagation phase of the eruptive prominence, after the acceleration phase. On the right panel we can observe the position angle of the prominence over time. The angle varies by about one degree, confirming that the prominence is moving almost radially. The raw data and the averaged ones are shown in Table 4.8 in the Appendix.

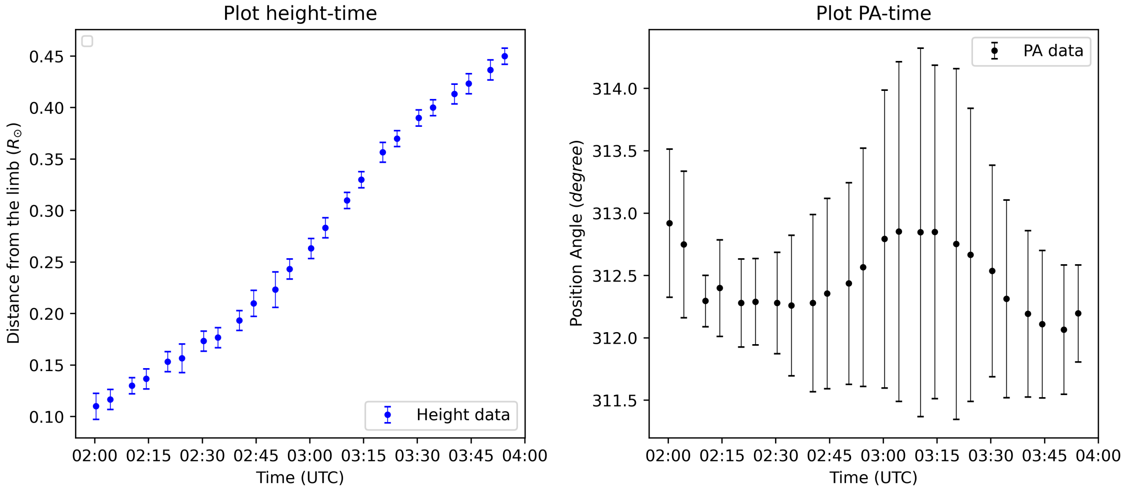

Figure 4.11: Event 2 height-time and PA-time plots. On the *left* the averaged height and on the *right* the averaged angular position of the prominence, both as a function of time.

To determine the transition from the acceleration phase to the propagation phase (t_f), I followed the procedure outlined in Section 3.4.2. The attempts are summarized in Table 4.2, with light blue cells highlighting the different efforts. I obtained a value of $\chi^2_\nu = 0.046$ for the propagation phase starting at 03:20 UT at a height of around 0.35 $R_\odot$ above the limb. Therefore, I selected the data until 03:20 UT to analyse the acceleration phase.
The chi-square values are consistently much smaller than 1, and this observation suggests that it is likely due to an overestimation of uncertainties on the data, and/or overfitting. Hence, I opted for the lower values as indicative of the best fit, even though they are significantly smaller than 1.

To determine the onset of the acceleration phase (t_0), I fitted the power-law function in the time range between 02:00 UT and 03:20 UT. The procedure for the initial time determination is well explained in Section 3.4.1. By varying the input time for the power-law function, I identified the output time that minimized the chi-square, as presented in Table 4.2, with the orange cells indicating the variations in the input time. All combinations yielded t_0 around 02:34 UT ($t_0 = 2073 \pm 266$ s) with $m = 1.59 \pm 0.22$ and $\chi^2_\nu = 0.046$. According to this analysis, the onset of the acceleration phase occurred at approximately 0.18 $R_\odot$ above the limb at 02:34 UT.

At this point I fitted the different functions: the power-law with $m = 1.59$, the parabolic and the exponential following the procedure in Section 3.4. The results are shown in Figure 4.12a and the associated parameters are shown in Table 4.12b. The power-law with $m = 1.6$ is seen to produce the lowest chi-square value ($\chi^2_\nu = 0.009$). The parabolic and the exponential fit provide larger values for chi-square ($\chi^2_\nu = 0.085$ and $\chi^2_\nu = 0.053$). It is worth noting that in all functions incorporating an acceleration term (power-law, parabolic and exponential), the coefficients related to this quantity were found to be approximately zero. Consequently, a linear function was also applied to the data between

t_0 and t_f. This resulted in a chi-square value of $\chi^2_\nu = 0.225$ one order of magnitude higher than the power-law fit. A linear fit appears to closely approximate the data within this, but something must have occurred at t_0 to account for the increase in velocity. From Table 4.12b, we can see that the p-values are all approaching one. The p-value reflects the probability that the observed data align with the null hypothesis, which assumes that the regression model used represents the data accurately. However, when the p-value is close to one, it implies a lack of statistical significance. Consequently, we cannot either confirm or reject the null hypothesis. See Section 3.4.3 for more details.

Initial time	Final time	Input t_0	Best t_0	m	χ^2_ν	prop-χ^2_ν
02:00	03:44	02:24	02:38	1.00	0.463	0.054
02:00	03:34	02:24	02:42	1.00	0.182	0.032
02:00	03:24	02:24	02:38	1.32	0.069	0.061
02:00	03:14	02:24	02:33	1.72	0.045	0.368
02:00	03:20	02:24	02:34	1.59	0.046	0.090
02:00	03:20	02:50	02:34	1.59	0.046	0.090
02:00	03:20	03:14	02:34	1.59	0.046	0.090
02:00	03:20	02:24	02:34	1.59	0.046	0.090

Table 4.2: EVENT 2 MINIMIZING χ^2. "Initial time" is the time of the first data measurement, "Final time" is the time when the acceleration phase is supposed to end, "Input t_0" is the input time to the python script and best t_0 is the best estimator for it. m and χ^2_ν are the exponent and the reduced chi square values respectively. The yellow row is the one that minimizes the chi square. The rows in which I changed the final time is emphasized with the cyan color, while the alteration in the input time is indicated by the peach color.

LOW CADENCE ANALYSIS The procedure was replicated similarly as for Event 1, omitting specific points to simulate a lower cadence analysis. The reduced count of points guided the selection to a 10 minutes cadence. This selection ensures an adequate number of points for conducting fitting, while also maintaining the same timing intervals among all points in each frame. The data selected for this particular analysis has been highlighted using a distinct color (Table 4.8 in the Appendix).

The analysis leads to slightly different conclusion as for high-cadence data. The results are presented in Figure 4.13. The initial time of the acceleration is set at 02:45 UT slightly bigger compared to the previous one (02:34 UT) and $m = 1.22 \pm 0.14$. The final time of the acceleration phase is the same (03:20 UT) as for the high cadence data. The power-law fit and the exponential fit, despite yielding small values of the variable χ^2 (0.090 and 0.019, respectively), resulted in values of a and d small or close to zero. The parabolic fit provides $\chi^2 = 0.303$, a value that is one or two orders of magnitude higher than the other functions, and again an acceleration close to zero. Therefore, linear functions also fit the data well between t_0 and t_f, yielding $\chi^2_\nu = 0.044$. Thus, the prominence is observed to rapidly increase its velocity after t_0, but it appears to propagate at a constant speed immediately afterward. It looks like the decrease in image cadence leads to a reduction in the determination of curvature. The fit coefficients (Table 4.13b) provide comparable or slightly higher values with reference to the high cadence analysis.

Thereafter, a linear trend also fit well the propagation phase giving a value $\chi^2_\nu = 0.199$. The relative parameters are found to be similar but less accurate compared with the high cadence results.

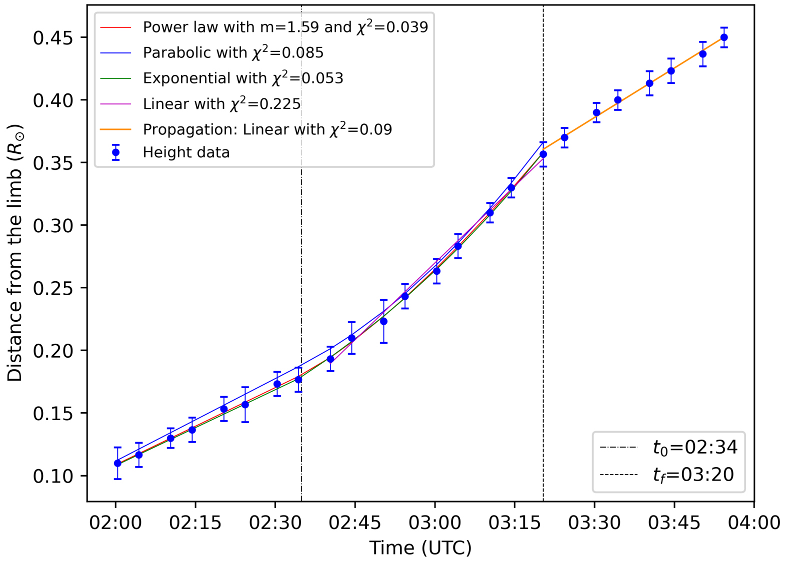

(a) Event 2 fitted functions. This height-time plot shows the functions fitted on the data during the analysis. Shifting the parabolic and the power-law functions by 0.002 $R_\odot$ helped distinguish the models on the height-time plot.

	Power law	**Parabolic**	**Exponential**	**Linear**	**Prop. Linear**
a	0.190 ± 0.010	0.00731 ± 0.00039	140972 ± 23554	-	-
b	23.82 ± 0.49	25.45 ± 0.62	23.40 ± 0.75	47.4 ± 1.4	30.53 ± 0.93
c	125462 ± 540	127468 ± 689	124852 ± 891	131088 ± 2182	250833 ± 1127
d	-	-	0.000233 ± 0.000029	-	
χ^2_ν	0.039	0.085	0.053	0.225	0.090
df	14	14	13	7	6
p	0.999	0.999	0.999	0.980	0.997

(b) Event 2 fit parameters. The employed functions are as follows: the power-law $a(t-t_0)^{1.6}+b(t-t_0)+c$, the parabolic $a(t-t_0)^2+b(t-t_0)+c$, the exponential $ae^{d(t-t_0)}+b(t-t_0)+c$ and the linear $bt+c$. For the power-law and the parabolic profile a represents respectively the variation in the acceleration [km/s$^{\mathrm{m}}$], and the acceleration itself [km/s^2]. For all of them, b is the averaged velocity of the prominence [km/s] and c the initial height of the prominence [km]. For the exponential, d [1/s] combined with a [km] is another coefficient that represents the variation in the acceleration. χ^2_ν is the reduced chi square, df the degrees of freedom and p the p-value.

Figure 4.12: Event 2: Fit results. The resulting analysis concerns the high cadence data.

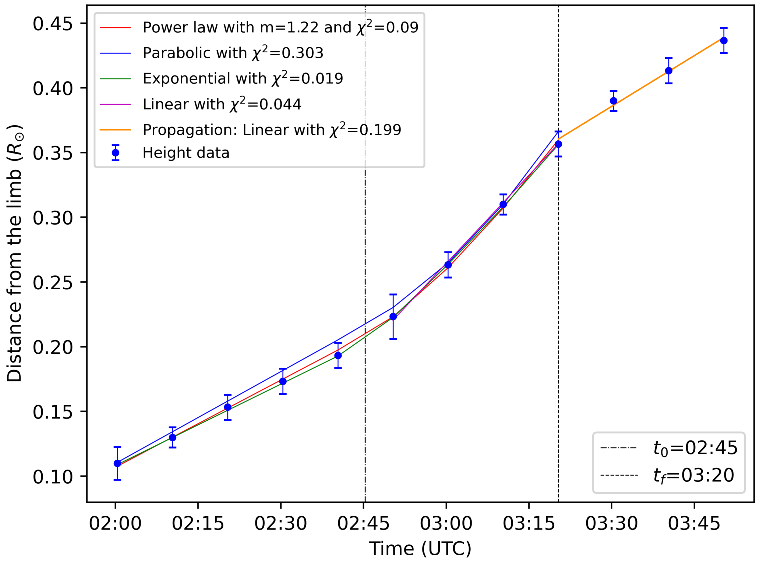

(a) Event 2 fitted functions. This height-time plot shows the functions fitted on the data during the analysis. Shifting the parabolic and the power-law functions by 0.002 $R_\odot$ helped distinguish the models on the height-time plot.

	Power law	**Parabolic**	**Exponential**	**Linear**	**Prop. Linear**
a	0.240 ± 0.020	0.0105 ± 0.0014	328348 ± 87540	-	-
b	26.02 ± 0.83	27.43 ± 1.27	24.31 ± 0.45	52.7 ± 1.3	30.3 ± 2.2
c	145076 ± 1282	147473 ± 1938	142031 ± 731	152693 ± 1620	250744 ± 2382
d	-	-	0.000134 ± 0.000031	-	
χ^2_ν	0.090	0.303	0.019	0.044	0.199
df	6	6	5	2	2
p	0.997	0.912	0.999	0.957	0.819

(b) Event 2 fit parameters. The employed functions are as follows: the power-law $a(t-t_0)^{1.2}+b(t-t_0)+c$, the parabolic $a(t-t_0)^2+b(t-t_0)+c$, the exponential $ae^{d(t-t_0)}+b(t-t_0)+c$ and the linear $bt+c$. For the power-law and the parabolic profile a represents respectively the variation in the acceleration [km/s$^{\mathrm{m}}$], and the acceleration itself [km/s^2]. For all of them, b is the averaged velocity of the prominence [km/s] and c the initial height of the prominence [km]. For the exponential, d [1/s] combined with a [km] is another coefficient that represents the variation in the acceleration. χ^2_ν is the reduced chi square, df the degrees of freedom and p the p-value.

Figure 4.13: Event 2: Fit results. The resulting analysis concerns the low cadence data.

4.2.2 Kinematic analysis

I investigated the velocity and the acceleration of the prominence during its propagation, both in the high-cadence and low-cadence analyses. I calculated these quantities using the two different methods outlined in Section 3.5: I calculated the velocity from the measured heights (1) and from the heights performed with the best fit function (2). In this analysis I report the latter because allows to obtain quantities close to the former, but with less uncertainty. The results are presented in Figure 4.14. The first graph presents again the height-time plot in [km] fitted with the the power-law for the slow rise and acceleration phase, and the linear fit for the propagation phase. In the middle and lowest graphs, the velocity and the acceleration of the prominence are presented.

In the slow-rise phase the prominence starts to increase with an averaged constant velocity of:

$$v_{0,high} = 23.8 \pm 1.3 \text{ km/s} \qquad v_{0,low} = 26.6 \pm 3.2 \text{ km/s} \tag{4.3}$$

The high cadence value is compatible with the b coefficient of the power law, i.e. $b_{high} = 23.82 \pm 0.49$ km/s (see Table 4.12b). This represents the speed of the prominence when the acceleration starts. In the case of the low cadence, $b_{low} = 26.02 \pm 0.83$ km/s, which is compatible with the averaged one (4.13b). In this interval the acceleration turns out to be approximately zero:

$$a_{0,high} = 0.0 \pm 7.0 \text{ m/s}^2 \qquad a_{0,low} = 0.0 \pm 8.0 \text{ m/s}^2 \tag{4.4}$$

After 02:34 UT, the prominence is seen to accelerate and increase its velocity, reaching a maximum value of $v_{max} = 56.9 \pm 5.3$ km/s for high cadence data and $v_{max} = 59.9 \pm 7.5$ km/s for low cadence data. Both values were reached at 03:20 UT. Note that these values are not average, but the maximum values recorded. In addition, the prominence is observed to experience a maximum value of acceleration of $a_{max} = 26 \pm 17$ km/s^2 for high cadence data and $a_{max} = 21.9 \pm 8.9$ km/s^2 for low cadence data.

Finally, after 03:20 UT (t_f) the prominence decelerates and appears to reach a constant value. The averaged velocity calculated during the propagation phase is:

$$v_{p,high} = 36.0 \pm 2.3 \text{ km/s} \qquad v_{p,low} = 36.6 \pm 3.4 \text{ km/s} \tag{4.5}$$

Both values are compatible with the slope parameters of the propagation phase. Referring to the high cadence analysis, $b_{prop} = 30.53 \pm 0.93\,\text{km/s}$ and for the low cadence data $b_{prop} = 30.3 \pm 2.2\,\text{km/s}$. The averaged acceleration in this interval is close to zero:

$$a_{p,high} = -5 \pm 12 \text{ m/s}^2 \qquad a_{p,low} = -7.0 \pm 8.0 \text{ m/s}^2 \tag{4.6}$$

In general, the low cadence provides values similar to the high cadence values, but with higher uncertainties. In contrast to the situation observed for event 1, the low-cadence analysis yields results with greater uncertainties. This is likely attributed to the fact that, while in the previous case the elimination of certain data points helped in the mitigation of “steps” (as discussed in Section 4.1), generally, a larger dataset contributes to a more precise analysis.

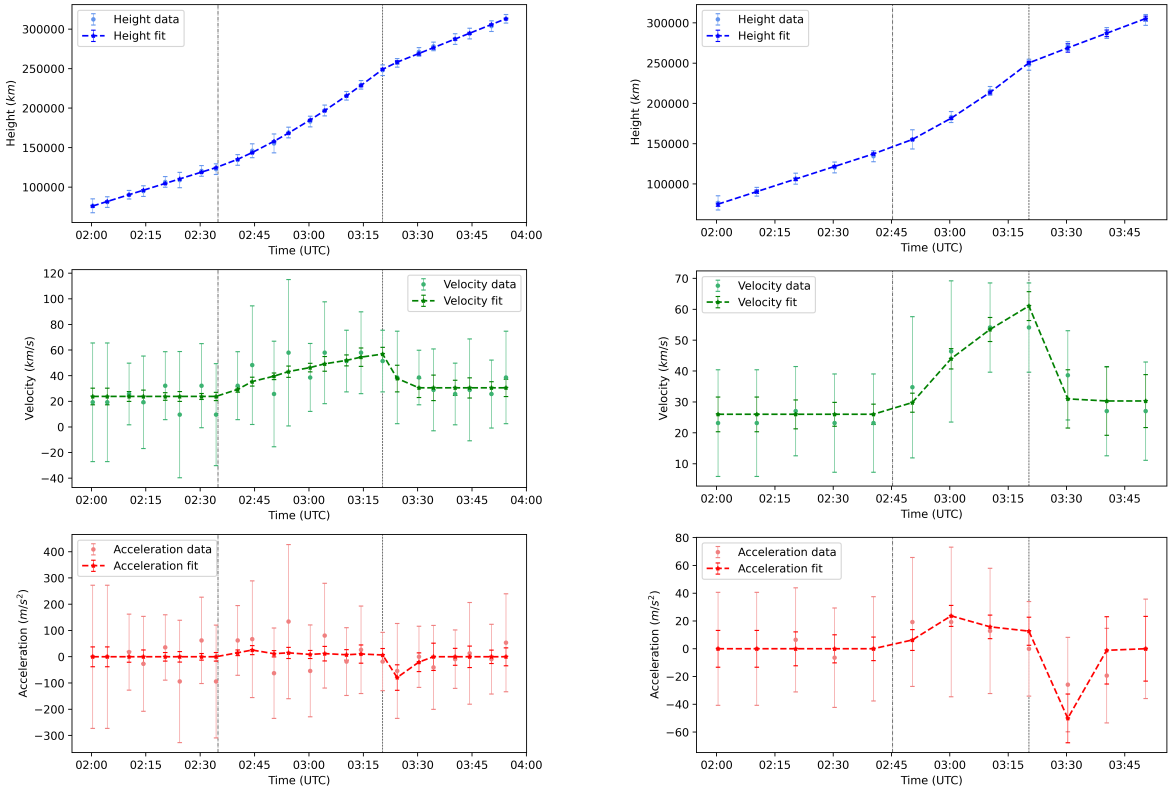

(a) Event 2. High cadence kinematic plot. **(b)** Event 2. Low cadence kinematic plot.

Figure 4.14: Event 2 kinematics. Distances from the limb (height) in [km] are shown, "Height fit" represents the fit for the early phase and acceleration phase (*top*). "Velocity" (green dots) is calculated from the differential of the height data in time [km/s]. The green dashed line represents the differential calculated from the linear function called "Fitted velocity" (*middle*). "Acceleration data" are calculated from the differential of velocity in time [m/s^2], and the red dashed line represents the "Fitted acceleration" differential calculated from the fitted velocity (*bottom*). The vertical black dotted lines mark the transition between the slow rise, the acceleration, and the propagation phases.

4.2.3 Influence of the surrounding corona

As mentioned in Section 1.2.6, searching for bursts of light at the eruption site or the presence of jetting activity, current sheets, plasmoids, etc ... could potentially indicate the involvement of magnetic reconnection with the prominence eruption. However, when examining the sequence of FSI 304 images it was challenging to clearly identify the footpoints of the prominence. They appeared to be slightly arched behind the Sun. Similar observations were made when looking at images from other perspectives and other instruments, such as SDO/AIA or STEREO-A/EUVI, where it remained elusive to pinpoint the precise location of the prominence's footpoints.

To analyze the corona surrounding the eruption I also looked at the images recorded by FSI 174 and at the PFSS extrapolation provided in jHelioviewer. All these elements are visible in Figure 4.15. The PFSS model suggested that the prominence was enveloped by magnetic loops, a conclusion that is also supported by observations in FSI 174. In fact, it can be observed that the prominence eruption occurs within an active region (black region in Figure 4.10a or bright region in Figure 4.15). In Figure 4.15b, even though the eruption wasn't distinctly visible in the FSI 174 channel, a large coronal feature (pointed by arrows) was discernible in the surrounding corona, aligning with the positions of the active region. Looking at coronographic images with LASCO-C2 [16], that large scale coronal feature appears to be at the base of a coronal streamer. The site of the eruption seems to correspond with a multipolar region, as can be confirmed by looking at the SOHO/MDI Magnetogram [16] images of that region.

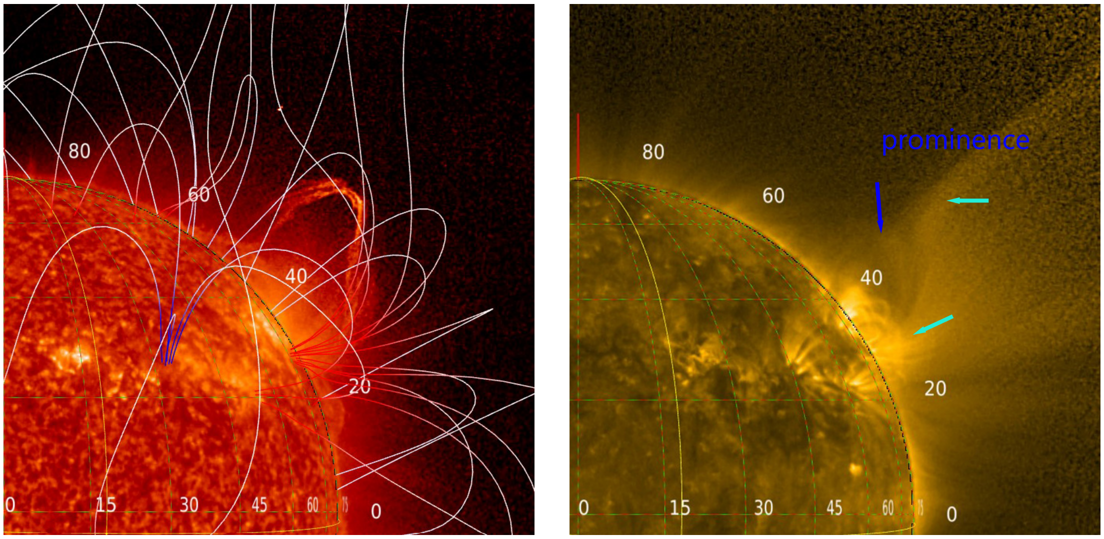

(a) FSI 304 Å. **(b)** FSI 174 Å.

Figure 4.15: 2022-01-25 03:34:50 UTC . The different channels through which EUI can observe the Sun and The PFSS model of the solar magnetic field lines (*left*).

4.2.4 Discussion

The analysis conducted so far suggests that a power-law with an exponent between 1 and 2 provides the best model for characterizing the eruption. Specifically, from the high cadence data, I found an exponent of $m = 1.59 \pm 0.22$, while from the low cadence data, it was $m = 1.22 \pm 0.1$. This indicates a slight imbalance in the forces acting on the filament during its propagation phase, although this imbalance is relatively small and occurs for less than an hour.

The comparison between high-frequency and low-frequency analyses allows us to understand the impact of cadence on estimating the kinematics of the eruptive phenomena. It is crucial to limit the fitting parameters of the kinematic profile, as they are influenced by the cadence of the instruments used for estimation. This aspect has been explored in previous studies (Byrne et al., 2013 [18]; Vashishtha et al., 2023 [124]).

The cadence analysis yields similar results in terms of initial time, final time, best fit, and parameter determination. However, it becomes evident from both the high and low cadence analysis that reducing the image frequency leads to a loss of information about the curvature of the power-law, causing the function to tend towards linearity. In this specific event, which had a cadence of four to six minutes, increasing the cadence further might reveal a more pronounced curvature. This could potentially help align the eruption more closely with existing models found in the literature.

4.3 Event 3

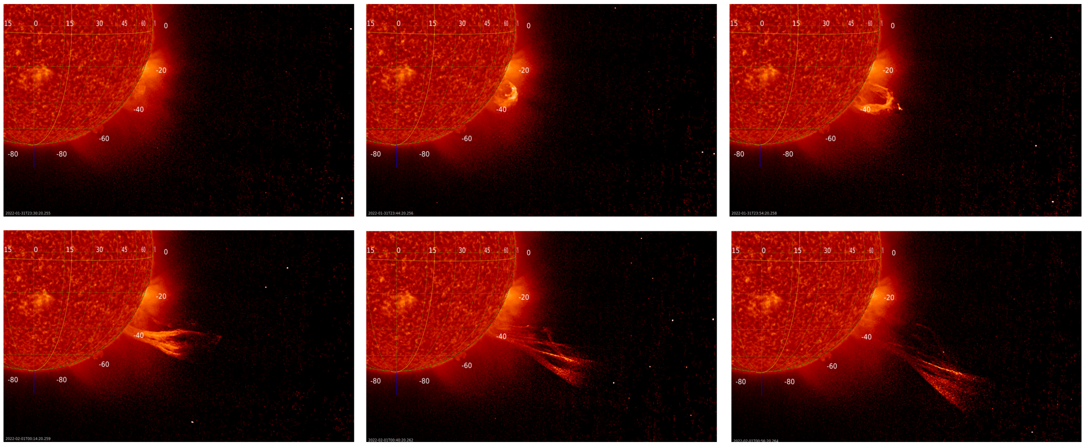

Figure 4.16: Event 3 observed on 2022-01-31 and 2022-02-01. Sequence of images at increasing time.

The third event ("Event 3") under study is another loop-like eruption occurring at the South-West of the Sun, (see Figure 3.1c), between the January 31st and February 1st, 2022. The loop-like prominence starts to rise around 23:10 UT (at a height of 0.06 $R_\odot$ above the solar limb), it starts to twist before midnight and it can be followed until 00:15 UT the next day when it reached a height of 0.62 $R_\odot$ above the limb. A sequence of the evolution of the prominence is provided in Figure 4.16. The measurement procedure involves tracking the prominence's motion (three times) along the direction indicated by the black arrow in Figure 4.17a. It is evident from the figure that the prominence propagates in an almost radial manner, despite a small deflection. It's worth noting that, in this case, I tracked not the leading point of the prominence but the twisting point, which is the location where the filament appears to coil upon itself. This cross-point is highlighted in Figure 4.17a. This behavior bears a resemblance to the occurrence of a helical kink instability, which could potentially serve as an explanation for triggering this eruption. In the final stage of propagation, the prominence undergoes a change in morphology and extends in a fan-like shape. I did not collect data points during this phase because the same features that were measured during the ascent are no longer distinguishable. The image cadence is between four and two minutes.

4.3.1 Initiation mechanisms

High cadence analysis The averaged distance and position angle over time for Event 3 are presented in Figure 4.18. The left panel shows the height-time plot where it possible to observe apparently two different trends. On the right panel one can observe the position angle of the prominence over time. The angle varies by about six degrees during the propagation of the prominence. The event propagates almost radially until approximately midnight, after that the eruption is observed to twist and to deviate from the radial direction. In this analysis I assume that the tracked feature propagates radially, despite the small deviation of six degrees of the position angle. The raw data and the averaged ones are shown in Table 4.9 in the Appendix.

The initial time (t_0) of the acceleration phase was determined through the procedure explained in Section 3.4.1. The various attempts to determine it are presented in Table 4.3. All the efforts return the same initial time t_0 at 23:53 UT ($t_0 = 1294 \pm 185$ s) with $\chi^2_\nu = 0.524$ and $m = 1.90 \pm 0.35$. The

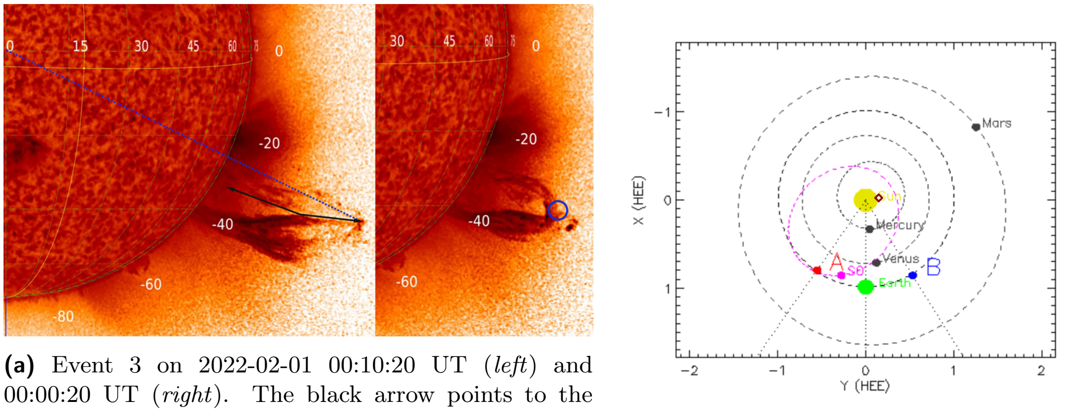

(a) Event 3 on 2022-02-01 00:10:20 UT (*left*) and 00:00:20 UT (*right*). The black arrow points to the tip of the prominence under study while propagating. The blue dashed line indicates the radial direction of the leading point. The feature which was tracked is encircled in the right panel.

(b) EVENT 3 RELATIVE POSITION AT 23:30 UT. The red rhombus roughly indicates the location of the solar eruption. For more details refer to Section 2.4.2.

Figure 4.17: EVENT 3 OBSERVED ON 2022-01-31.

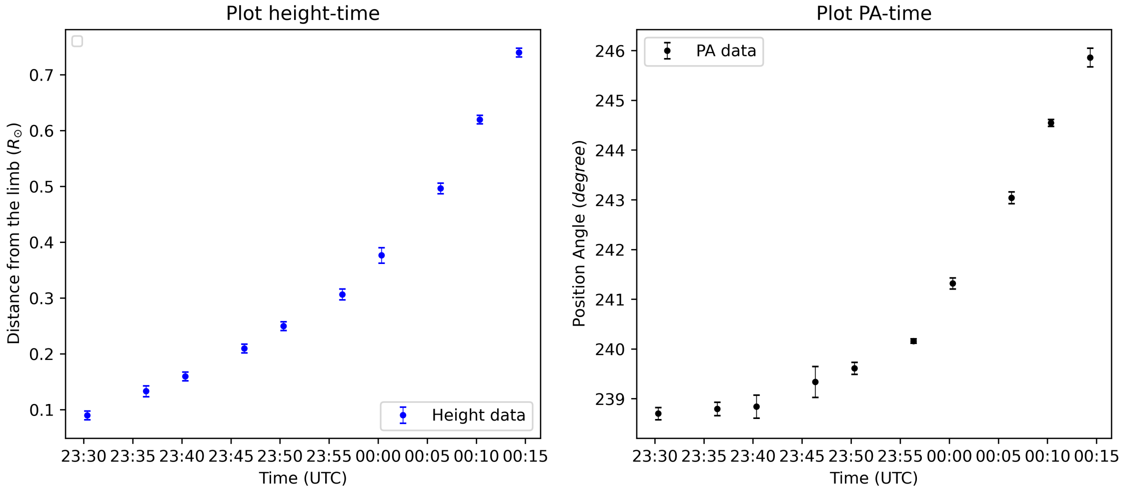

Figure 4.18: 2022-01-31 HEIGHT-TIME AND PA-TIME PLOTS. On the left the height and on the right the angular position of the prominence, both as function of time.

prominence is seen to accelerate between the heights of 0.2 and 0.3 $R_\odot$ above the limb.

At this point I fitted various functions to the data points: the power-law with $m = 1.9$, the parabolic, and the exponential. Please refer to Figure 4.19, where you can find the plot of the fitted functions along with their respective parameters.

The parabolic function yields $\chi^2_\nu = 0.494$. The power-law with fixed m and t_0 gives $\chi^2_\nu = 0.900$. which is very close to 1, and at the same time a value of m close to 2. Even the exponential fit appears to closely represent the data, returning $\chi^2_\nu = 0.760$. Looking at the table it becomes evident that the coefficient d is very small, leading me to exclude this function from consideration. Additionally, the linear fit fails to replicate the data, resulting in a $\chi^2_\nu = 6.999$ ($p = 0.0001$) and not aligning with the observed velocity increase. The chi value is larger than the critical value set at 2.605 with 3 degrees of freedom (see Table 4.48). Thus we can reject the hypothesis that a linear function represents the data with a confidence level of 95%.

The p-value reflects the probability that the observed data align with the null hypothesis, which assumes that the regression model used represents the data accurately. However, when the p-value is close to one (or higher than the significance level 0.05), it implies a lack of statistical significance.

Initial time	Final time	Input t_0	Best t_0	m	χ^2_ν
23:30	00:14	23:55	23:51	1.90	0.524
23:30	00:14	00:00	23:51	1.90	0.524
23:30	00:14	23:40	23:51	1.90	0.524
23:30	00:14	23:50	23:51	1.90	0.524

Table 4.3: EVENT 3 MINIMIZING χ^2. "Initial time" is the time of the first data measurement, "Final time" is the time when the acceleration phase is supposed to end, "Input t_0" is the input time to the python script and best t_0 is the best estimator for it. m and χ^2_ν are the exponent and the reduced chi square values respectively.

Consequently, for the other models, we cannot either confirm or reject the null hypothesis. See Section 3.4.3 for more details. In this analysis I selected the parabolic function as the best fit for the data because it results in parameters of higher accuracy. Additionally, also the power-law with free parameters returns a coefficient close to 2, and the power-law with fixed m and t_0 returned a chi square value close to one.

LOW CADENCE ANALYSIS The low cadence analysis was not conducted for this particular event. Despite the instrument's high operating frequency, the event itself was also moving at a relatively high speed, allowing us to collect only 10 data points related to the same prominence feature. Further reduction in the number of data points would not have been suitable for conducting a meaningful statistical analysis.

4.3.2 Kinematic analysis

In this section I investigate the velocity and the acceleration of the prominence during its propagation. I calculated these quantities using the two different methods outlined in Section 3.5: I calculated the velocity from the measured heights (1) and from the heights performed with the best fit function (2). The latter allows to obtain quantities close to the former, but with less uncertainty. Thus in the analysis I report the latter. The results are presented in Figure 4.20. The upper panel of the figure presents the height-time plot and its best fit with the parabolic function. In the middle and the lowest panels one can observe the velocity and the acceleration extracted from the data and from the fit.

Initially the prominence rises with an approximately averaged velocity of

$$v_0 = 93.7 \pm 6.2 \text{ km/s} \tag{4.7}$$

The prominence is moving very fast compared to the velocity at which the slow rise is often observed (1-15 km/s [85]).
The speed is compatible with the value obtained from the b coefficient of the parabolic fit, i.e. $b = 93.7 \pm 2.7$ km/s from Table 4.19b. b represents the initial speed of the acceleration phase. The acceleration in this interval is $a_0 = -9 \pm 32$ m/s^2 which is basically zero due to the large uncertainties.

After 23:51 UT, the prominence is observed to steeply increase its velocity, reaching a maximum value of $v_{max} = 379 \pm 40$ km/s at 00:10 UT. This is not an average, it is the maximum value recorded for its velocity. The averaged acceleration of the prominence turns out to be:

$$a_0 = 233 \pm 39 \text{ m/s}^2 \tag{4.8}$$

During this interval, the acceleration should be comparable with the acceleration term in the parabolic fit. The acceleration in a parabolic profile is given by $2a_{fit}$ where $a_{fit} = 117.0 \pm 4.0$ m/s^2 is the parameter associated with the second order term. Thus the expected acceleration should be around $a_{exp} = 234.0 \pm 8.0$ m/s^2. The two values are indeed compatible with each other.

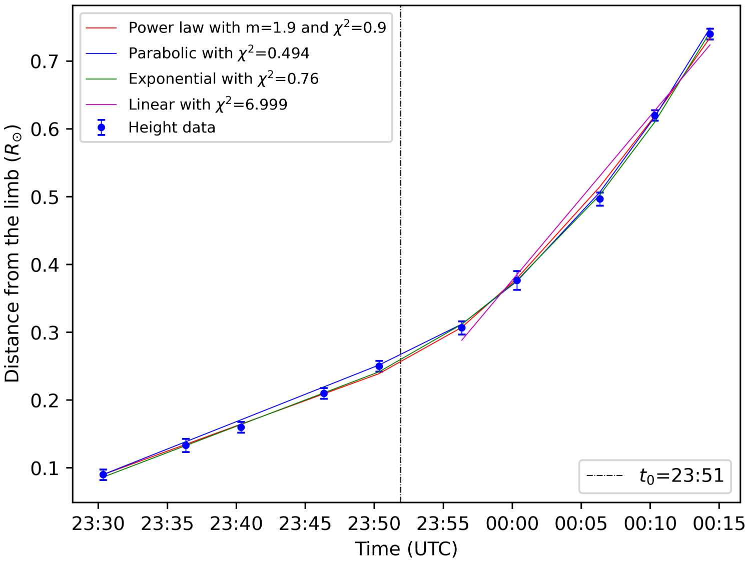

(a) Event 3 fitted functions. This height-time plot shows the functions fitted on the data during the analysis. Shifting the parabolic and the power-law functions by 0.002 $R_\odot$ helped distinguish the models on the height-time plot.

	Power law	**Parabolic**	**Exponential**	**Linear**
a	2.17 ± 0.10	0.1165 ± 0.0037	158985 ± 28101	-
b	86.4 ± 4.3	93.7 ± 2.7	90.1 ± 4.4	281 ± 19
c	174359 ± 3088	180438 ± 1960	177266 ± 3316	199836 ± 14881
d	-	-	0.000850 ± 0.000090	-
χ^2_ν	0.900	0.494	0.760	6.999
df	7	7	6	3
p	0.505	0.814	0.579	0.0001

(b) Event 3 fit parameters. The employed functions are as following: the power-law $a(t-t_0)^{1.9}+b(t-t_0)+c$, the parabolic $a(t-t_0)^2+b(t-t_0)+c$, the exponential $ae^{d(t-t_0)}+b(t-t_0)+c$ and the linear $bt+c$. For the power-law and the parabolic profile a represents respectively the variation in the acceleration [km/s$^{\mathrm{m}}$], and the acceleration itself [km/s^2]. For all of them, b is the averaged velocity of the prominence [km/s] and c the initial height of the prominence [km]. For the exponential, d [1/s] combined with a [km] is another coefficient that represents the variation in the acceleration. χ^2_ν is the reduced chi square, df the degrees of freedom and p the p-value.

Figure 4.19: Event 3: Fit results. The resulting analysis concerns the high cadence data.

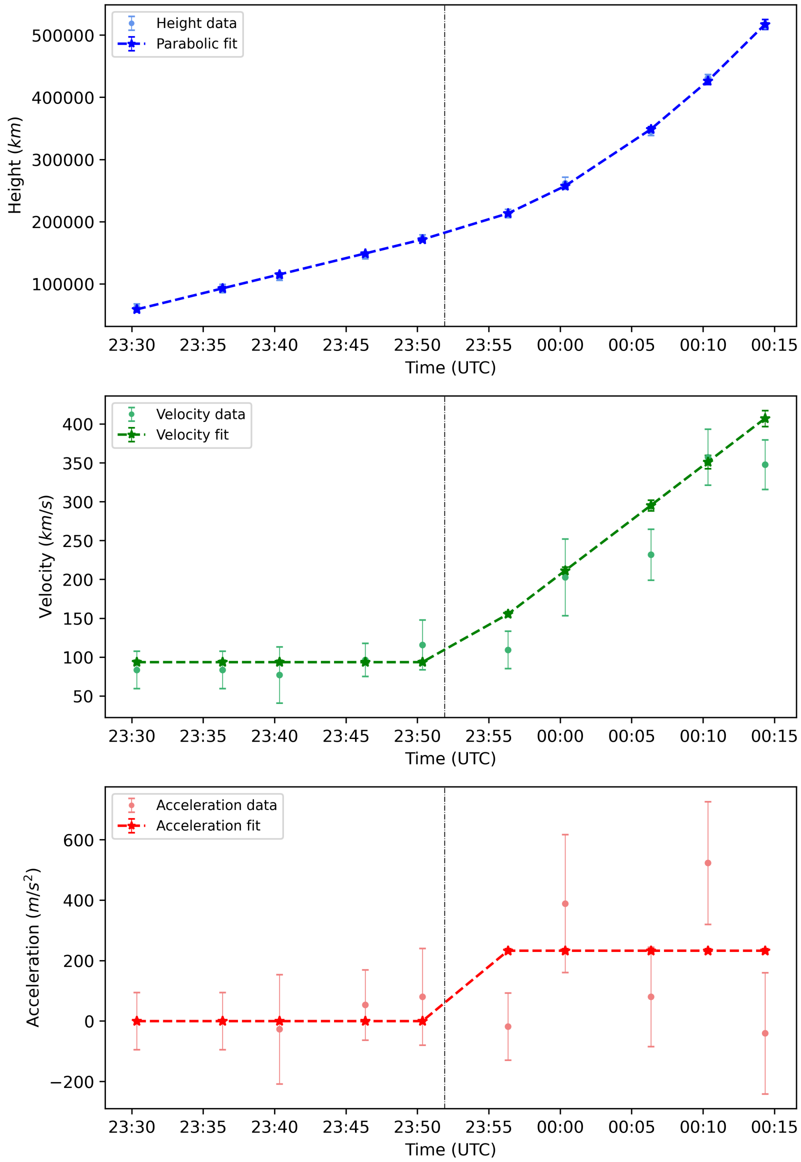

.

Figure 4.20: Event 3 kinematics. Distances from the limb (height) in [km] are shown (*top*). "Velocity" (green dots) is calculated from the differential of the height data in time [km/s]. The green dashed line represents the differential calculated from the linear function called "Fitted velocity" (*middle*). "Acceleration data" are calculated from the differential of velocity in time [m/s^2], and the red dashed line represents the "Fitted acceleration" differential calculated from the fitted velocity (*bottom*). A black dotted line is placed at t_0

4.3.3 Influence of the surrounding corona

The presence of sudden brightning, or plasmoids, etc. on the site of the eruption, might be indicative of magnetic reconnection going on (see Section 1.2.6 for more details). However, the prominence originates in the backside of the Sun as observed from SolO's perspective. Yet, by looking at the images from SDO/AIA 304 one can observe both the footprints of the erupting prominence at the limb (see Figure 4.21a). The angular separation between FSI images and AIA images is 19 degrees. Therefore, the prominence observed in FSI is positioned at an angle of at least 19 degrees behind the Sun. From the FSI 304 images and especially upon examining the AIA 304 images, one can observe particularly bright regions at the base of the prominence and at its top. The brightness in the footpoints can be indicative of magnetic reconnection.

To analyze the corona surrounding the eruption I looked at the images recorded by FSI 304, FSI 174 and at the PFSS extrapolation provided in jHelioviewer. From Figure 4.22, we can observe that the prominence is propagating in a region with open magnetic field lines. Open field lines may be an indication of the presence of coronal holes. This scenario was subsequently validated through observations of the Sun utilizing the AIA 193 telescope on the Solar Dynamics Observatory (SDO) (refer to Figure 4.21b).

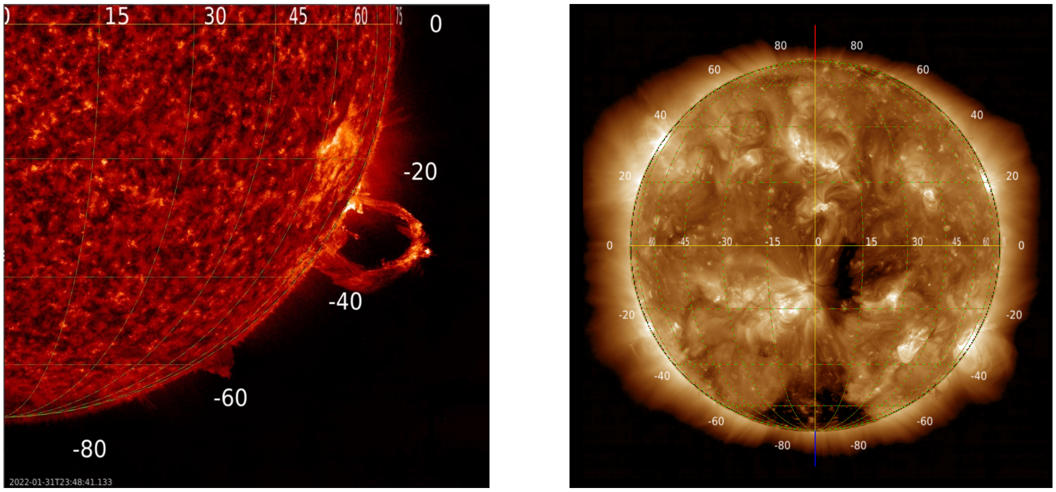

(a) 2022-01-31 23:48:41 UTC. AIA 304

(b) 2022-01-14 20:17:52 UTC. AIA 193.

Figure 4.21: EVENT 3. Images obtained through the SDO/AIA telescope.

These observations reveal the distinct presence of a large dark region that precisely characterizes the coronal hole, located at the southern pole of the Sun in January. Additionally, another one (smaller) is observed in the southern hemisphere near the equator. However, the presence of the coronal holes does not appear to deflect the prominence trajectory. The prominence propagates almost radially, as already mentioned. Moreover, it is also possible to observe that after the prominence experiences a twisting motion, it continues to propagate resembling a fan-like eruption, as shown in Figure 4.22b.
By observing the North-West side of the Sun from the 30th of January onwards, one can spot the region from which the prominence originated before rotating to the backside of the Sun. This area is characterized by large active regions, as depicted in Figure 4.23a. Consequently, in FSI 174, it becomes possible to observe the prominence, as indicated by the blue arrow in Figure 4.23b. Upon examining the two images in Figure 4.23, one can discern something resembling a large-scale coronal feature overlying the site of the eruption. It is worth noting that the eruption of the prominence occurs close to an active region with multiple loops. This can be associated with a multipolar region, as can be confirmed by looking at the SOHO/MDI Magnetogram images of that region, the same as for Event 2.

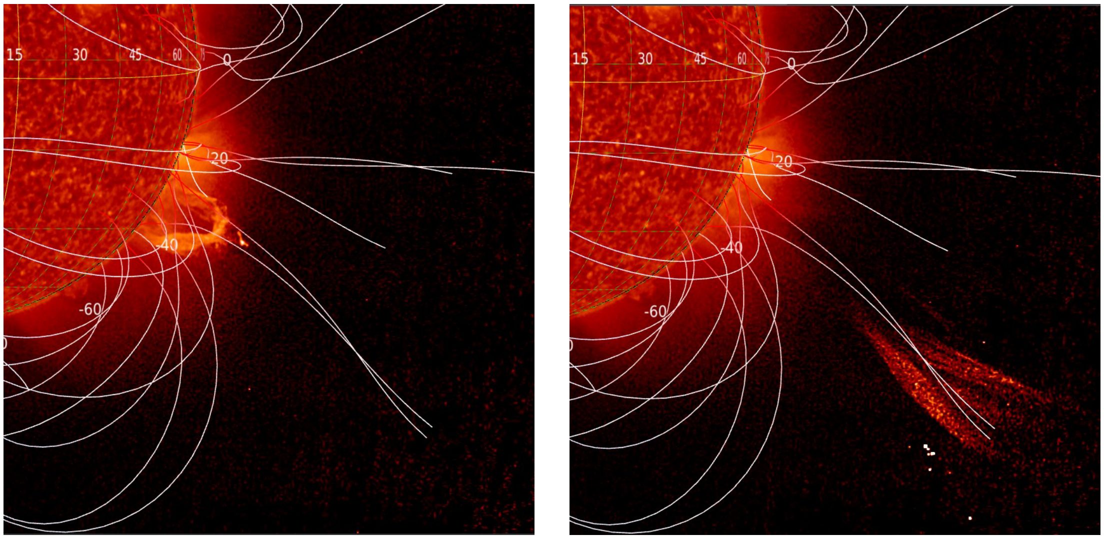

(a) 2022-01-31 23:54:20 UT. **(b)** 2022-01-31 01:16:20 UT.

Figure 4.22: EVOLUTION OF EVENT 3 IN FSI 304 IMAGES. The PFSS model of the magnetic field lines. The prominence is moving in a region with open magnetic field lines.

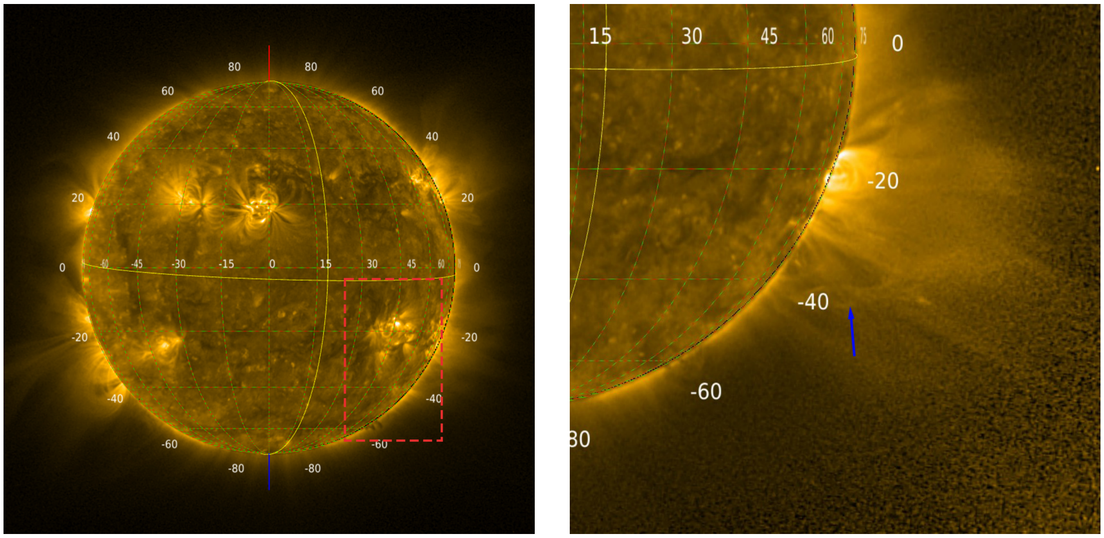

(a) 2022-01-28 22:56:50 UT **(b)** 2022-01-31 23:54:50 UT

Figure 4.23: EVENT 3 IN FSI 174 IMAGES. The red box surrounds an active region (*left*) situated in the vicinity from where the prominence is anticipated to erupt. The image is taken before the active region becomes obscured from the observer's view as a result of the Sun's rotation. The prominence can be observed also in FSI 174 (indicated by the blue arrow) even if not very clearly.

4.3.4 Discussion

The statistical analysis has revealed that the prominence is best represented by a parabolic model, implying that the prominence undergoes acceleration at a relatively constant rate. This finding aligns with the breakout model, which incorporates the concept of magnetic reconnection as a driving force in the eruption's acceleration phase. However, it is important to note that the prominence exhibits twisting, a characteristic typically associated with helical instability. This twisting may also be influenced by the surrounding corona.

Nevertheless, this twisting phenomenon, as well the CHs, do not seem to significantly impact the propagation of the eruption, which is observed to move radially. This is probably due to its high speed, which at the initial stage was estimated to be $b = 93.7 \pm 2.7$ km/s from the parabolic fit parameters. Indeed, several authors established that strong magnetic fields emanating from active regions where CMEs originate can influence CME deflection (e.g., Möstl et al., 2015 [77]; Wang et al., 2015 [126]; Kay, Opher, and Evans, 2015 [55]). This deflection is inversely proportional to the speed and mass of the CME. Specifically, during solar minimum, slower and broader CMEs tend to deflect toward the equator, while faster and narrower CMEs experience less deflection, and in certain cases, they propagate radially from their source region.

It's worth noting that this event was observed to be located approximately 19 degrees behind the solar limb. As discussed in Section 3.3.2, the projection effect has the potential to introduce a significant source of error when measuring prominence heights. Correction for this effect may be necessary once it becomes feasible to determine the angle at which the prominence is positioned in relation to the limb. On a related note, Figure 3.3 illustrates the increasing discrepancy with the angle behind the limb. For instance, at an angle of 20 degrees, the difference between the measured height and the true height of the prominence is 6.03%. While this value is still comparable to other sources of uncertainty, it's important to consider that the prominence likely doesn't maintain a constant angle throughout its motion. This factor, in combination with the fact that the prominence doesn't move radially, could potentially explain the observed discrepancies in the analysis.

Regarding the cadence analysis, it was not possible to conduct it for this event due to an insufficient number of data points.

4.4 Event 4

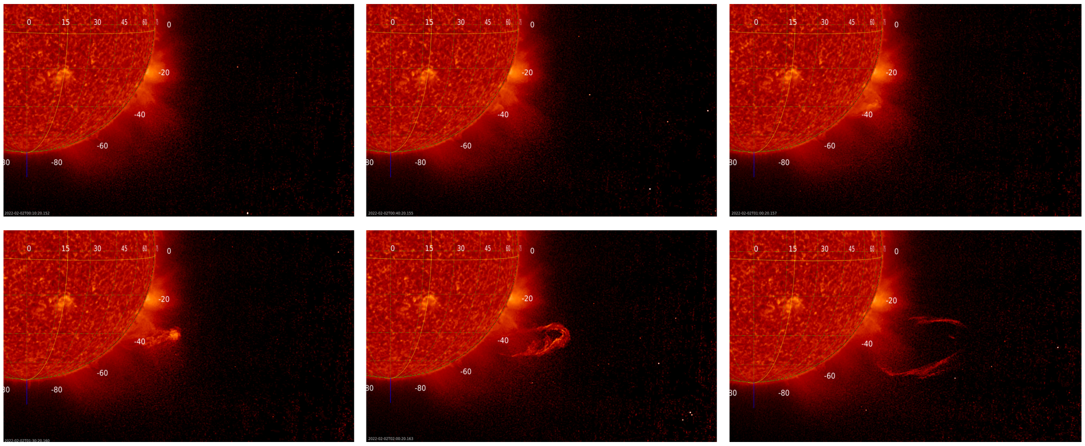

Figure 4.24: Event 4 observed on 2022-02-02. Sequence of images at increasing time.

The fourth eruption in this study ("Event 4") is observed at the South-West of the Sun (refer to Figure 3.1d) on February 2nd, 2022. The evolution of this loop-like prominence is presented in Figure 4.24. The eruption was initiated at 00:10 UT at a distance of 0.03 $R_\odot$ from the solar limb and could be tracked until it reached a height of 0.71 $R_\odot$ above the limb at 02:34 UT. The loop is not clearly observed from the beginning, but it becomes visible from the fourth image on, when it appears as if it has been rotated toward our line of sight. The measurement procedure involves tracking the prominence's motion along the direction indicated by the black arrow in Figure 4.25a, repeating the measurements three times. In the figure it is also possible to observe that the position angle varies significantly during its propagation. Thus, the observed prominence demonstrates a non-radial propagation, moving almost horizontally. This event is a noteworthy subject for understanding the forces influencing such events. The image cadence is 4 and 2 minutes.

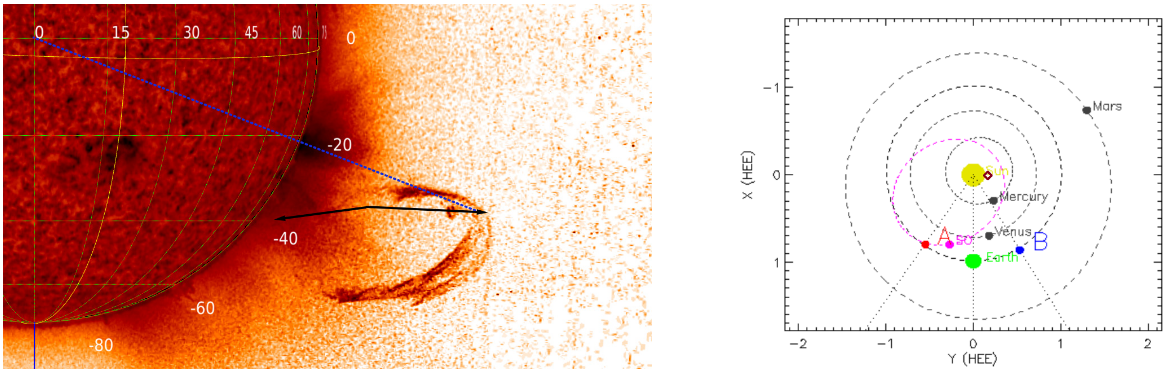

(a) Event 4 on 2022-02-02 02:34:20 UT. The black arrow points to the tip of the prominence under study while propagating. The blue dashed line indicates the radial direction of the leading point.

(b) Event 4 relative position at 00:00 UT. The red rhombus roughly indicates the location of the solar eruption. For more details refer to Section 2.4.2.

Figure 4.25: Event 4 observed on 2022-02-02.

4.4.1 Initiation mechanisms

High cadence analysis The averaged heights and position angles over time are presented in Figure 4.26. The left panel shows the height-time plot where we can guess different growth regions. Specifically, there is a linear trend that closely resembles the acceleration phase. In the right panel the position angle of the prominence over time is shown. The angle varies with approximately 16 degrees confirming that the prominence is not moving radially. The raw data and the averaged ones are shown in Table 4.10 in the Appendix.

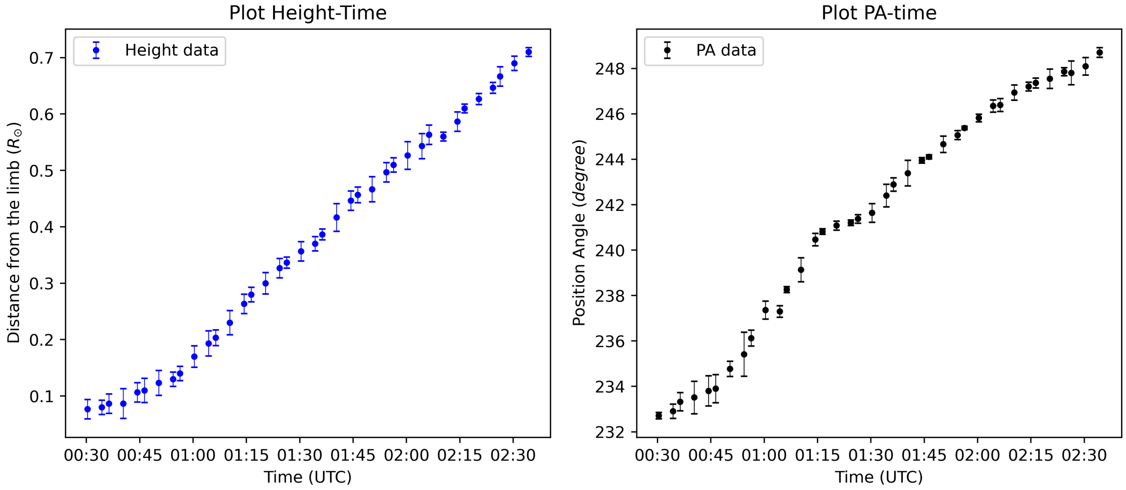

Figure 4.26: Event 4 height-time and PA-time plots. On the *left* the averaged height and on the *right* the angular position of the prominence, both as function of time.

To determine the transition from the acceleration phase to the propagation phase, I followed the procedure outlined in Section 3.4.2. The attempts are summarized in Table 4.4 where light-blue cells highlights different candidates as the beginning of the propagation phase, or the ending of the

acceleration phase (t_f). Given that there are no chi-square values close to 1, it suggests the potential overestimation of data uncertainties or overfitting. Therefore, I chose the model that minimizes the chi-square value, as it appears to be the most appropriate in this context.
I obtained that the change in slope occurs at 01:14 UT at a height of 0.26 $R_\odot$ above the limb, with a value of $\chi^2_\nu = 0.380$.

To determine the onset of the acceleration phase (t_0), I fitted again the power-law following the procedure in Section 3.4.1. The combination providing the lowest value for chi square is emphasized with a yellow row in Table 4.4. It means that $t_0 = 840 \pm 486$ s, thus the acceleration starts around 00:44 UT at a height of around 0.12 $R_\odot$. The power-law returns $m = 1.94 \pm 0.64$.

Initial time	Final time	Input t_0	Best t_0	m	χ^2_ν	prop-χ^2_ν
00:30	02:34	00:50	00:49	1.00	0.473	-
00:30	02:26	00:40	00:48	1.00	0.564	0.011
00:30	02:00	00:44	00:44	1.06	0.307	0.450
00:30	01:44	00:44	00:44	1.13	0.330	0.535
00:30	01:34	00:40	00:53	1.00	0.176	0.502
00:30	01:26	00:44	00:44	1.42	0.178	0.450
00:30	01:14	00:40	00:40	2.16	0.071	0.380
00:30	01:14	00:36	00:36	2.34	0.072	0.380
00:30	01:14	00:44	00:44	1.94	0.067	0.380

Table 4.4: EVENT 1 MINIMIZING χ^2. "Initial time" is the time of the first data measurement, "Final time" is the time when the acceleration phase is supposed to end, "Input t_0" is the input time to the python script and best t_0 is the best estimator for it. m and χ^2_ν are the exponent and the reduced chi square values respectively. The yellow row is the one that minimizes the chi square. The rows in which I changed the final time is emphasized with the cyan color, while the alteration in the input time is indicated by the peach color.

The time interval encompassing the slow rise and the acceleration of the prominence has thus been determined between 00:30 UT and 01:14 UT. At this point, I fitted the data points in this range with different functions: the power-law with $m = 1.94$, the parabolic, and the exponential, following the procedure in Section 3.4. In this case I employed also a linear function because the curvature of the data in the height-time plot appeared very subtle. The results are shown in Figure 4.27. In figure 4.27a I present all the fitting functions. All of them appear to reproduce well the data. The power-law with $m = 1.94$, which is close to 2, returns $\chi^2_\nu = 0.073$. The lowest value is obtained with the parabolic function giving $\chi^2_\nu = 0.061$. The exponential fit provides a slightly higher value for the chi-square ($\chi^2_\nu = 0.087$). The linear function gives a value of an order of magnitude higher ($\chi^2_\nu = 0.507$), but it cannot explain the observed change in slope at t_0. In Table 4.10 one can see the coefficients of the fitted functions. The exponential fit is characterized by a coefficient d very small, and as a consequence it was excluded from the analysis. The parabolic fit provides the parameters with the highest accuracy and the lowest chi-square value. Moreover, the power-law gave a coefficient m close to 2. Thus, the parabolic function is selected as the best fit to the data.

A linear function is also used to fit the last points of the propagation phase (after the acceleration phase). It appears to reproduce quite well the data with a value of $\chi^2_\nu = 0.380$.

The p-value reflects the probability that the observed data aligns with the null hypothesis, which assumes that the used regression model represents the data accurately. However, when the p-value is close to one, it implies a lack of statistical significance. Consequently, we cannot either confirm or reject the null hypothesis (see Section 3.4.3).

LOW CADENCE ANALYSIS The procedure was replicated omitting specific points to simulate a lower cadence analysis (10 minutes cadence). The data selected for this particular analysis has been highlighted using a distinct color (Table 4.10 in the Appendix).
The analysis leads to an earlier time for the onset of the acceleration phase at 00:32 UT. And similar conclusion for the end of the acceleration phase at 01:20 UT.

The results for the low cadence analysis are shown in Figure 4.28a. The power law returns a lower value for the coefficient m and higher uncertainty: $m = 1.5 \pm 6.9$ with $\chi^2_\nu = 0.169$.

At this point, I fit again all the functions (Figure 4.28a). The values of the parameters associated with the fitted functions are shown in Table 4.28b. The power-law ($\chi^2_\nu = 0.003$) and the exponential fit ($\chi^2_\nu = 0.007$) return the lowest values for the chi square value. The parabolic functions gives $\chi^2_\nu = 0.083$. Then, the linear function returns a value for chi-square of 1 or 2 orders in magnitude higher ($\chi^2_\nu = 0.335$). The power-law and the exponential provide a negative value for b, which indicates that the velocity is decreasing. However there is only one point before t_0 so these values are not reliable. Also, the exponential is characterized by a very small coefficient d, so the exponential term is negligible. Again, the parabolic function is chosen as the best fit.

Based on the low cadence analysis, it is challenging to definitively determine which fit is the most suitable. However, considering that the parabolic function provides more reliable parameters and that the power-law function might yield a lower coefficient value m due to the cadence limitations, it is reasonable to conclude that the parabolic function remains the most probable choice.

Considering a and b (but also c) for the parabolic function, we can see that the low cadence analysis provides lower values and lower accuracy compared with the high cadence analysis.

The data points on the propagation phase, after 01:20 UT, are still compatible with a linear trend. However the chi square is slightly higher with respect to the high cadence analysis ($\chi^2_\nu = 0.497$). The coefficients of the linear function are found to be lower and less accurate than the high cadence results.

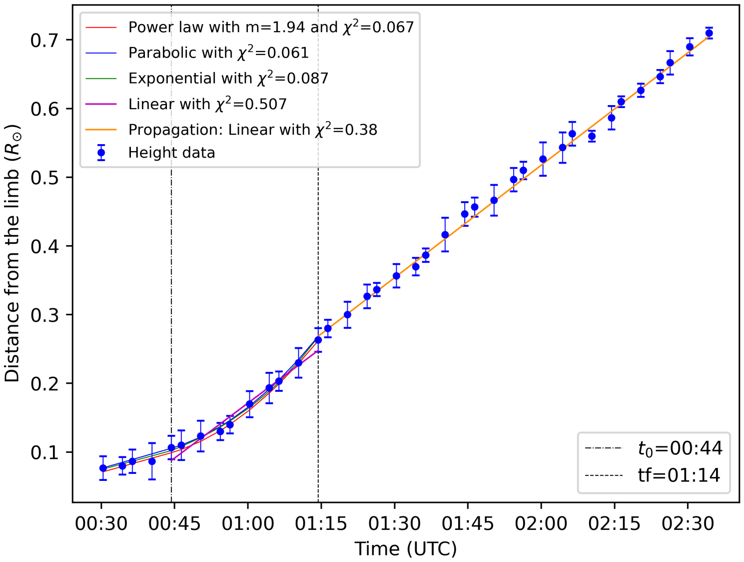

(a) Event 4 fitted functions. This height-time plot shows the functions fitted on the data during the analysis. Shifting the parabolic and the power-law functions by 0.002 $R_\odot$ helped distinguish the models on the height-time plot.

	Power law	**Parabolic**	**Exponential**	**Linear**	Prop. Linear
a	0.490 ± 0.040	0.0218 ± 0.0015	46267 ± 13202	-	-
b	18.6 ± 2.5	23.6 ± 1.8	22.4 ± 4.4	61.9 ± 4.9	63.26 ± 0.71
c	68585 ± 1178	71248 ± 929	70332 ± 2250	60957 ± 4976	187378 ± 2249
d	-	-	0.00069 ± 0.00011	-	
χ^2_ν	0.073	0.061	0.087	0.507	0.380
df	11	11	10	8	23
p	0.999	0.999	0.999	0.852	0.997

(b) Event 4 fit parameters.The employed functions are as follows: the power-law $a(t-t_0)^{1.94}+b(t-t_0)+c$, the parabolic $a(t-t_0)^2+b(t-t_0)+c$, the exponential $ae^{d(t-t_0)}+b(t-t_0)+c$ and the linear $bt+c$. For the power-law and the parabolic profile a represents respectively the variation in the acceleration [km/s$^{\mathrm{m}}$], and the acceleration itself [km/s^2]. For all of them, b is the averaged velocity of the prominence [km/s] and c the initial height of the prominence [km]. For the exponential, d [1/s] combined with a [km] is another coefficient that represents the variation in the acceleration. χ^2_ν is the reduced chi square, df the degrees of freedom and p the p-value.

Figure 4.27: Event 4: Fit results. The resulting analysis concerns the high cadence data.

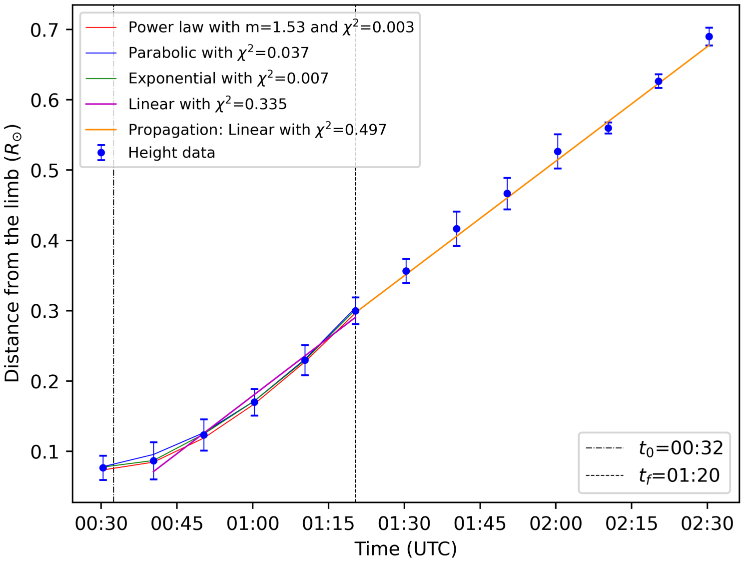

(a) EVENT 4 FITTED FUNCTIONS. This height-time plot shows the functions fitted on the data during the analysis. Shifting the parabolic and the power-law functions by 0.002 $R_\odot$ helped distinguish the models on the height-time plot.

	Power law	**Parabolic**	**Exponential**	**Linear**	Prop. Linear
a	0.460 ± 0.010	0.01359 ± 0.00096	93817 ± 9699	-	-
b	-0.5 ± 1.2	15.1 ± 2.7	-83 ± 13	63.6 ± 4.7	63.0 ± 1.9
c	53086 ± 501	54249 ± 1567	42693 ± 1503	49503 ± 7412	207513 ± 5878
d	-	-	0.000355 ± 0.000022	-	
χ^2_ν	0.003	0.037	0.007	0.335	0.497
df	3	3	2	3	6
p	0.999	0.963	0.934	0.800	0.811

(b) EVENT 4 FIT PARAMETERS. The employed functions are as follows: the power-law $a(t-t_0)^{1.53}+b(t-t_0)+c$, the parabolic $a(t-t_0)^2+b(t-t_0)+c$, the exponential $ae^{d(t-t_0)}+b(t-t_0)+c$ and the linear $bt+c$. For the power-law and the parabolic profile a represents respectively the variation in the acceleration [km/s$^{\mathrm{m}}$], and the acceleration itself [km/s^2]. For all of them, b is the averaged velocity of the prominence [km/s] and c the initial height of the prominence [km]. For the exponential, d [1/s] combined with a [km] is another coefficient that represents the variation in the acceleration. χ^2_ν is the reduced chi square, df the degrees of freedom and p the p-value.

Figure 4.28: EVENT 4: FIT RESULTS. The resulting analysis concerns the low cadence data.

4.4.2 Kinematic analysis

I investigated the velocity and the acceleration of the prominence during its propagation, both in the high-cadence and low-cadence analyses. I calculated these quantities using the two different methods outlined in Section 3.5: I calculated the velocity from the measured heights (1) and from the heights performed with the best fit function (2). In the analysis I report the latter, because it allows to obtain quantities close to the former, but with less uncertainty. The results can be observed in Figure 4.29. The upper panel shows the height of the prominence in [km] and the best-fit function: the parabolic fit for the slow rise and the acceleration phase, and the linear fit for the propagation phase. In the middle and bottom panels, the velocity and the acceleration are shown. We can see that, before 01:20 UT the prominence moves with an averaged constant velocity:

$$v_{0,high} = 24 \pm 5 \text{ km/s} \tag{4.9}$$

There is only one point for the low cadence analysis before t_0 so I only reported the high cadence value for the slow-rise phase. The velocity is compatible with the b coefficient of the parabolic function: $b = 23.6 \pm 1.8$ km/s (high cadence data) presented in Table 4.35b. The coefficient b represents the initial speed when the acceleration phase starts.

The prominence starts to accelerate reaching the highest speed observed during its eruption of $v_{max} = 97 \pm 22$ km/s (high cadence data) and $v_{max} = 85 \pm 17$ km/s (low cadence data) at 01:20 UT. Note that this is not an average but the maximum value recorded. The averaged acceleration for the data points on the acceleration phase (i.e. after t_0 and before t_f) is:

$$a_{high} = 13 \pm 17 \text{ m/s}^2 \qquad a_{low} = 9.5 \pm 6.5 \text{ m/s}^2 \tag{4.10}$$

These values should be comparable with the acceleration term in the parabolic fit. The acceleration in a parabolic profile is given by $2a_{fit}$ where $a_{fit} = 21.8 \pm 1.5$ m/s^2 is the parameter associated with the second order term. Thus the expected acceleration should be around $a_{exp} = 43.6 \pm 3.0$ m/s^2 from the high cadence analysis (and 27.2 ± 2.0 m/s^2 from the low cadence analysis). However the value obtained from the analysis is significantly lower. The lower values are explained due to the fact that a_{high} (and a_{low}) are averaging positive and negative values in this interval.

After 03:20 UT the prominence is seen to decelerate and reaching a constant velocity of:

$$v_{p,high} = 63.3 \pm 3.6 \text{ km/s} \qquad\qquad v_{p,low} = 62.9 \pm 7.0 \text{ km/s} \tag{4.11}$$

These are compatible with the slope parameter of linear function reproducing the propagation phase. In this linear function, the coefficient b represents the speed at which the prominence moves after the acceleration stopped. In this case, $b_{prop} = 63.26 \pm 0.71$ km/s (high cadence) and 63.0 ± 1.9 km/s (low cadence). Note that the acceleration:

$$a_{0,high} = -4 \pm 26 \text{ m/s}^2 \qquad\qquad a_{0,low} = 1 \pm 16 \text{ m/s}^2 \tag{4.12}$$

is almost zero, taking into account the large uncertainties. In general, the values obtained from the low cadence analysis appears to be slightly lower than the high cadence one. This holds true for both the fit parameters and for the averaged values. In the case of the fit parameters the uncertainties increases with a smaller data set, while for the averaged values the situation is opposite.

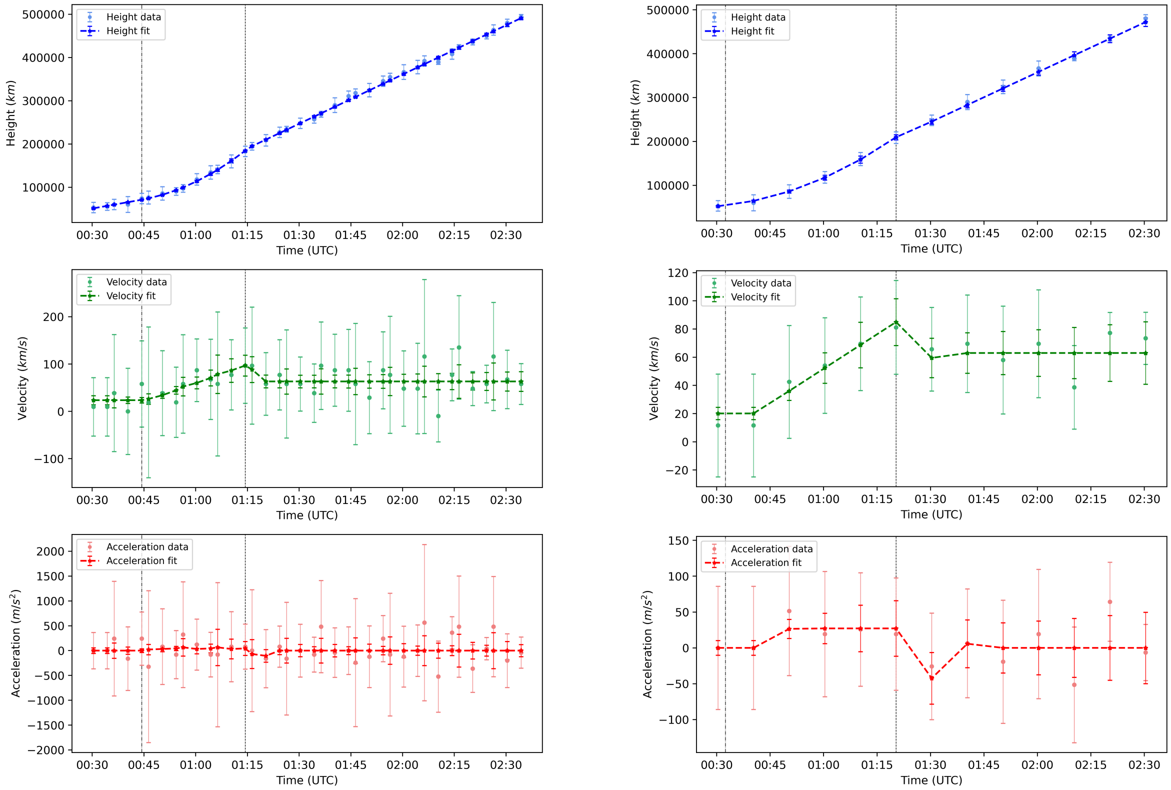

(a) Event 4. High cadence kinematic plot.

(b) Event 1. Low cadence kinematic plot.

Figure 4.29: Event 4 kinematics. Distance from the limb (height) in [km] are shown, “Height fit” represents the fit for the early phase and acceleration phase (*top*). (*top*). “Velocity” (green dots) is calculated from the differential of the height data in time [km/s]. The green dashed line represents the differential calculated from the linear function called “Fitted velocity” (*middle*). “Acceleration data” are calculated from the differential of velocity in time [m/s^2], and the red dashed line represents the “Fitted acceleration” differential calculated from the fitted velocity (*bottom*). The vertical black dotted lines marked the transition between the slow rise, the acceleration, and the propagation phases.

4.4.3 Influence of the surrounding corona

Searching for sudden brightening, plasmoids, etc. at the eruption site could potentially indicate the involvement of dissipative processes in driving the eruption's acceleration, such as magnetic reconnection (refer to Section 1.2.6 for more details).

In the FSI images, the footpoints are not visible, and only one leg of the filament is discernible (see Figure 4.24). Nonetheless, in the AIA 304 images (see Figure 4.30), a leg of the prominence can be observed at the limb, even though the footpoint is not clearly visible. Taking into account the relative position of SolO in relation to SDO (as described in Section 2.4.2), the eruption is occurring approximately 19 degrees or more behind the limb. Nevertheless, there is no noticeable increase in brightness observed either at the eruption site or on the prominence itself.

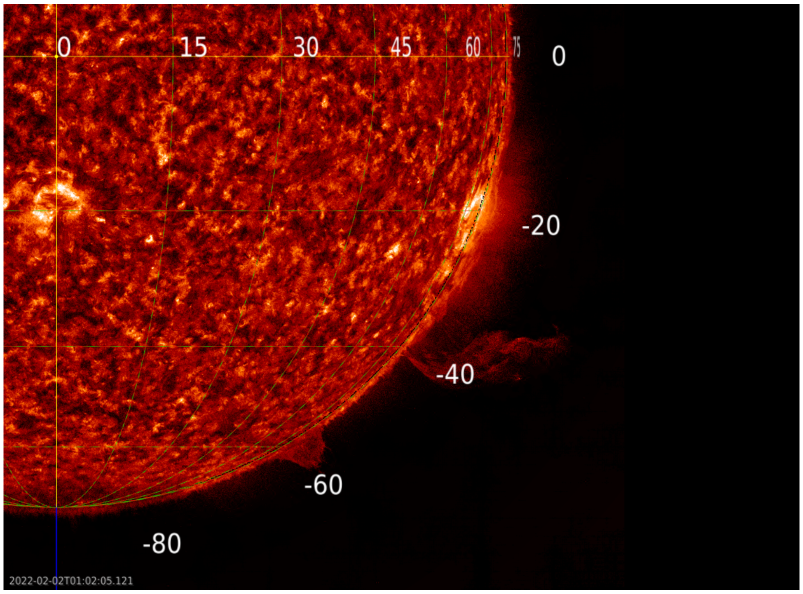

Figure 4.30: Event 4 from SDO/AIA 304 Å. Just one leg of the prominence is seen from SDO/AIA 304.

As already mentioned, we can observe only a leg of the eruption during the first frames. Probably because we are observing it laterally and then it twists, making the loop visible even from the perspective of Solar Orbiter. The prominence also experiences a strong deflection leading it to propagate almost horizontally in the plane of the image. Therefore, having confirmed the presence of a big coronal hole to the south of the Sun and its nearby active region (see Section 4.3, Event 3 took place less than two days before), the deflection could be attributed to the global magnetic field topology. As depicted in Figure 4.31a, the prominence is observed in the proximity of both open and closed magnetic field lines, akin to the scenario described earlier for Event 3 (4.3). Both eruptions look to come from the same (or close-by) active region of the Sun and start at approximately the same position angle near the equator. Consequently, the erupting prominence might be susceptible to the effects of the nearby coronal hole and of the coronal changes induced by the previous eruption.

To comprehensively analyze the corona surrounding the eruption, I also examined the images captured by FSI 174 and the PFSS (1.2.4) extrapolation provided in jHelioviewer . All of these components are visible in Figure 4.31. The PFSS model indicates that the prominence is located near magnetic loops, a conclusion further supported by observations in FSI 174. Additionally, the prominence is surrounded by open magnetic field lines. However, unlike Event 3, the prominence is not observed to follow these open field lines due to the significant deflection it undergoes.

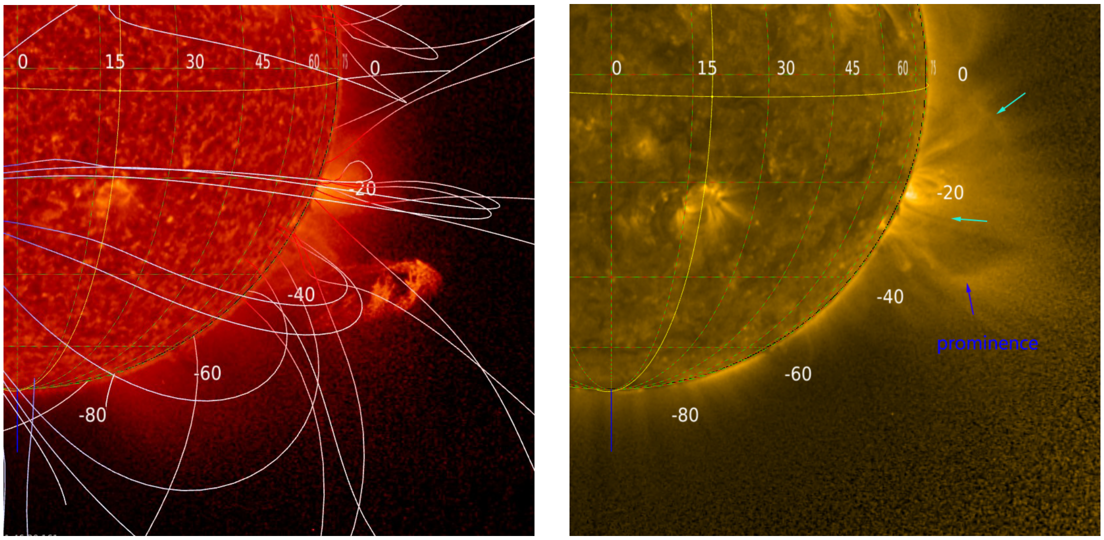

(a) 2022-02-02 01:46:20 UT. FSI 304 Å.

(b) 2022-02-02 00:00:50 UT. FSI 174 Å.

Figure 4.31: Event 4. The PFSS model of the solar magnetic field lines is shown over plotted on the data of 2022-02-02 00:14:00 UT (*left*). The prominence is quite faint in FSI 174 (*right*), as indicated by the blue arrow. One can distinguish some overlying loops in the sites pointed by the light-blue arrows.

4.4.4 Discussion

The analysis conducted so far suggests that a parabolic function provides the best model for this eruption (Event 4). This scenario aligns with the numerical simulations obtained for the height-time plot in a magnetic breakout model. However, some discrepancies were observed, such as the mean acceleration measured during the accelerating phase, which was found to be lower than that obtained from the fit. These anomalies could be attributed to the region being heavily affected by the underlying magnetic field topology. As previously mentioned, the prominence experiences significant deflection, and the cause has been linked to the huge coronal hole in the South of the Sun (see Section 1.4.8 for more details).

The comparison between high-frequency and low-frequency analyses has enabled us to discern the influence of cadence on the estimation of eruptive phenomena kinematics. Indeed, it is important to constrain the fitting parameters of the kinematic profile, as they are influenced by the instrument cadence used to derive these coefficients. This has been investigated by several authors (Byrne et al., 2013 [18]; and Vashishtha et al. 2023 [124]). The results obtained for the fitting parameters vary with cadence. Therefore the larger dataset allows for slightly more precise estimates.
In general, the results of the two analysis led to very similar conclusions about t_f. On the other hand, the low-cadence analysis shows an acceleration onset occurring approximately ten minutes earlier. Moreover, the power-law model with free parameters produced a lower coefficient m compared to the high-frequency model. This observation appears to support what I observed for Event 2 (Section 4.2), where it was evident that reducing the amount of data resulted in a loss of information concerning the curvature of the plot. For this particular event, I was able to compare the velocity and the acceleration of the prominence under both high and low cadence scenarios. The fit parameters obtained from the low cadence analysis return lower values with less precision. The same happens for the acceleration of the parabolic profile. The average values for velocity and acceleration align quite well with what was mentioned, yielding lower values for these quantities. Even if, for some values, the uncertainties associated with these values are smaller compared to the high cadence values.

It is important to notice that this particular event was observed to be situated approximately 19° behind the limb. As mentioned in Section 3.3.2, the projection effect has the potential to become the primary source of error when measuring prominence heights and might necessitate correction when it becomes feasible to determine the angle at which the prominence is situated in relation to the limb. On the other side, in Figure 3.3 I reported the average discrepancy with increasing angle behind the limb.

In the case of 20° the difference between the measured height and the true height of the prominence is 6.03 %. This value is still comparable with the other sources of uncertainties. However, taking into account that the prominence likely doesn't maintain a constant angle throughout its motion, this factor could potentially have an even greater impact. This, combined with the fact that the prominence does not move radially, could explain the discrepancies observed in the analysis.

4.5 Event 5

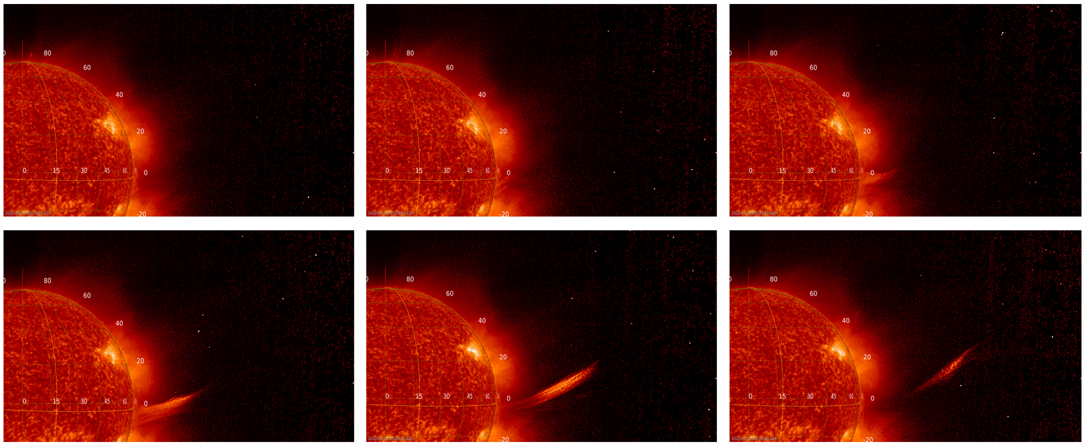

Figure 4.32: Event 5 observed on 2022-02-13. Sequence of images at increasing time.

The fifth event ("Event 5") under study is a jet-like eruption occurring on February 13th, 2022 (see Figure 3.1e). It starts at the equatorial region of the Sun and deflects to the North-West region (the position of the event is shown Figure 4.33b). The prominence starts to rise at around 02:04 UT (at a height of 0.05 $R_\odot$ above the limb) reaching a large height in the field of view of the image. However, the leading point of the jet can be followed until 02:40 UT when it reached a height of 0.44 $R_\odot$ above the limb. A sequence of the evolution of the prominence is provided in Figure 4.32. The measurement procedure involves tracking the prominence's motion along the direction indicated by the black arrow in Figure 4.33a measuring it backward three times for each image. It is evident from the figures that the prominence is largely deflected towards the Northern hemisphere. The image cadence is 4 and 2 minutes.

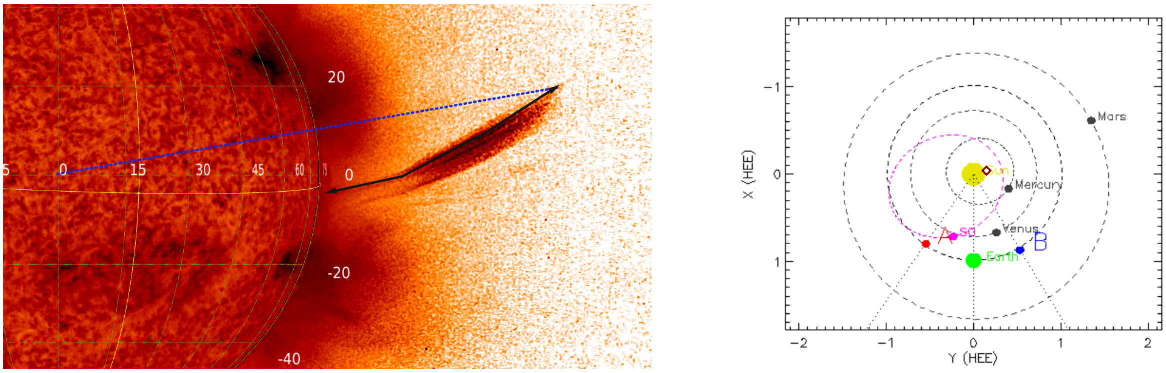

(a) Event 5 on 2022-02-13. The black arrow points to the tip of the prominence under study while propagating. The blue dashed line indicates the radial direction of the leading point.

(b) Event 5 relative position at 02:10 UT. The red rhombus roughly indicates the location of the solar eruption. For more details refer to Section 2.4.2.

Figure 4.33: Event 5 observed on 2022-02-13.

4.5.1 Initiation mechanisms

High cadence analysis The averaged distance and position angle over time are presented in Figure 4.34. The left panel shows the height-time plot where it is possible to observe two different trends. On the right panel one can observe the position angle of the prominence over time. The angle varies by around eight degrees during the propagation of the prominence. The raw data and the averaged ones are shown in Table 4.11 in Appendix.

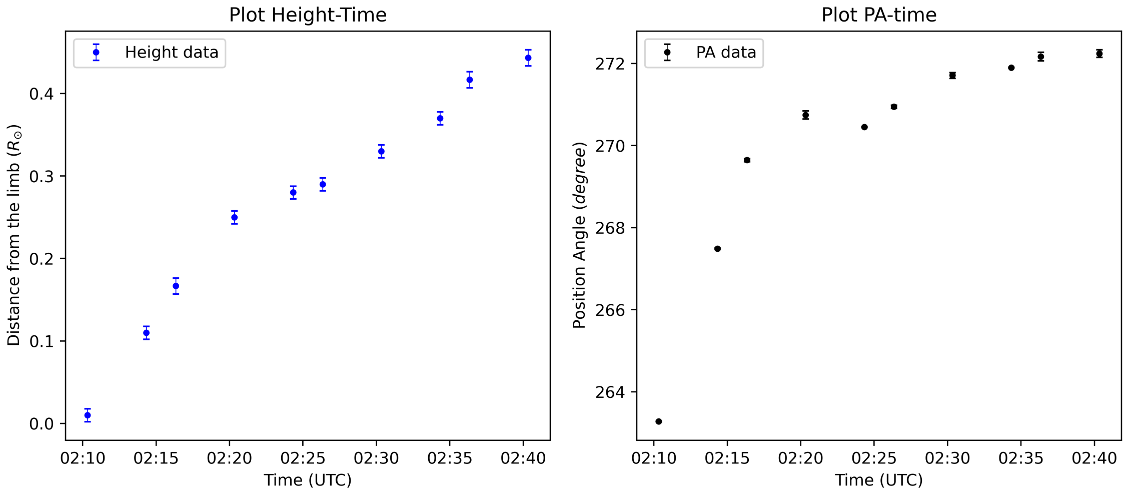

Figure 4.34: Event 5 height-time and PA-time plots. On the left panel the height is shown and on the right panel the angular position of the prominence, both as function of time.

Anticipating what I will discuss in the next section, based on the SDO/AIA 304 image, it appears that I may not have observed the slow-rise and acceleration phases but rather the end of the acceleration phase and the propagation phase. To address this, I have excluded the data points corresponding to the propagation phase using the standard procedure (see Section 3.4.2). Consequently, the remaining data points should align well with a linear fit, showing deceleration towards the end. This alignment is because the final points of the acceleration phase become indistinguishable from a linear trend. It is the transition from the slow rise to the acceleration phase that provides valuable information. The results are presented in Table 4.5. The first three rows lack sufficient data points for a statistical analysis of the acceleration phase. The lowest chi-square value is achieved by setting the final time t_f at 02:26 UT with a power-law coefficient of $m = 1.18 \pm 0.26$ ($\chi^2_\nu = 1.360$) which is close to the expected value of one. Thus, the prominence is observed to stop accelerating at approximately 0.29 $R_\odot$ above the limb. Regarding the onset time of acceleration, there is not sufficient data to make an estimation. The script I made in python returns t_0 at 02:19 UT, but this does not coincide with the onset of the acceleration phase, it gives the instant when its height-time profile is seen to change slope, i.e. when the prominence starts to decelerate, I will refer to this time as 't_d'.

Initial time	Final time	Input t_0	Best t_0	m	χ^2_ν	prop-χ^2_ν
02:10	02:16	-	-	-	-	7.141
02:10	02:20	-	-	-	-	1.897
02:10	02:24	-	-	-	-	1.503
02:10	02:26	02:10	02:19	1.18	0.180	1.360
02:10	02:30	02:10	02:10	1.679	4.413	1.877

Table 4.5: Event 5 minimizing χ^2. "Initial time" is the time of the first data measurement, "Final time" is the time when the acceleration phase is supposed to end, "Input t_0" is the input time to the python script and best t_0 is the best estimator for it. m and χ^2_ν are the exponent and the reduced chi square values respectively. The yellow row is the one that minimizes the chi square.

To validate my previous statements, I fitted the power-law with $m = 1.18$, the parabolic, and the exponential for the data before t_f. Refer to Figure 4.35, where you can find the plot of the fitted functions along with their respective parameters. All the functions seem to represent quite well the data. However, looking at the associated parameters, we can notice that the coefficients a related to the acceleration term are negative. This indicates that the prominence after t_d is observed to decelerate. The exponential fit provides the lower value for the chi square variable ($\chi^2_\nu = 0.227$), but the coefficient d is very small, thus it can be excluded. The parabolic fit provides a value of $\chi^2_\nu = 1.574$, slightly higher than 1. The power-law returns $\chi^2_\nu = 0.399$, slightly lower than 1. Even if the two points between 02:19 UT and 02:26 UT are not enough to perform a more accurate statistical analysis, they seem compatible with the deceleration of the prominence. However, an anomalous change in slope at t_d can be observed, and another one at t_f. It is essential to highlight that this particular event exhibits a significant deviation from the radial direction and displays a distinct morphology compared to other events. Tracking this event was particularly challenging, and it's possible that I didn't consistently follow the same point throughout the measurement phase. This could have influenced the recorded height values and explain this behaviour.

The p-value reflects the probability that the observed data align with the null hypothesis, which assumes that the regression model used represents the data accurately. In this case, the p-values align with what I have mentioned before. In fact, when the p-value are higher than the confidence level (0.05), it implies a lack of statistical significance. Consequently, we cannot either confirm or reject the null hypothesis, i.e. we cannot confirm or reject that the models represent the data.

It is not possible to associate an initiation mechanism to this event because we cannot determine which function is the better fit without observing the transition from the slow rise to the acceleration phase. Nevertheless, we can utilize certain parameters from the power-law function to extract some information, such as the initial speed, which can be obtained from the parameter b.

Low cadence analysis The low cadence analysis was not conducted for this particular event. Despite the instrument's high operating frequency, the event itself was moving at a relatively high speed, allowing us to collect only 10 data points related to the same prominence feature. Further reduction in the number of data points would not have been suitable for conducting a meaningful statistical analysis.

4.5.2 Kinematic analysis

I investigated the velocity and the acceleration of the prominence during its propagation. The velocity and the acceleration are obtained following the procedure explained in Section 3.5. I obtained these quantities using the two different methods outlined in Section 3.5: I calculated the velocity from the measured heights (1) and from the heights performed with the best fit function (2). For this specific case, I report the quantities obtained from the data (1), because no function was found to adequately represent the data. The results are presented in Figure 4.36. The upper panel presents the height-time plot in [km], the power-law fit with $m = 1.18$ until t_f and the linear fit for the propagation phase. In the middle and bottom graphs, the velocity and the acceleration are shown. Initially the prominence rises with an approximately averaged velocity of

$$v_0 = 296 \pm 29 \text{ km/s} \tag{4.13}$$

This value is compatible with the coefficient b obtained from the power-law in Table 4.35b, i.e. $b = 285.5 \pm 8.2$ km/s. As expected, the initial speed assumes a very high value, it seems more compatible with the end of the acceleration phase. This validates the fact that the initial slow-rise phase was not observed for this prominence. This will be exploited in more detail in the next section. The averaged acceleration in this initial observed phase is $a_0 = 24 \pm 181$ m/s^2, which is compatible with zero, due to the large uncertainty. The averaged acceleration which characterize the interval between t_d and t_f is:

$$a = -523 \pm 89 \text{ m/s}^2 \tag{4.14}$$

which confirm that the prominence is observed to decelerate very fast. After 02:26 UT the prominence is seen to propagate with a new constant velocity, with an averaged value of:

$$v_f = 118 \pm 19 \text{ km/s} \tag{4.15}$$

which is compatible with the b coefficient of the linear function used to fit the propagation phase, i.e. $b_{lin} = 131 \pm 11$ km/s. The averaged acceleration in this interval is $a_p = -22 \pm 141$ m/s^2. Which is compatible with zero, but with large uncertainty.

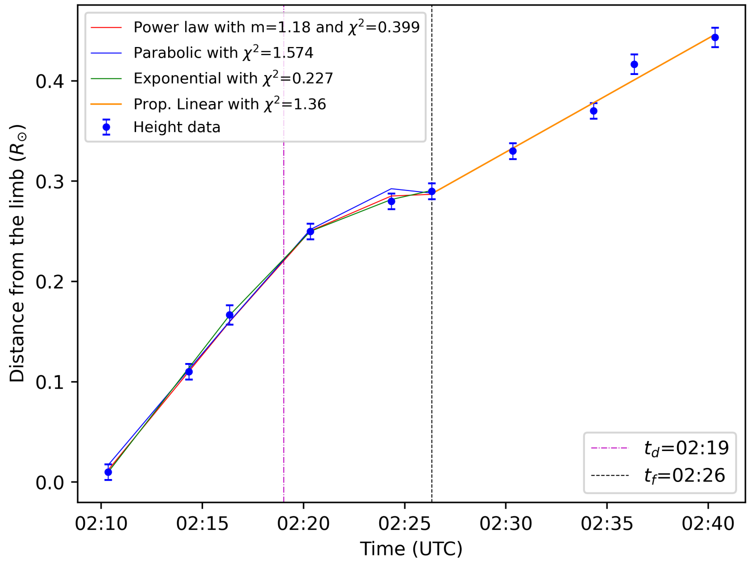

(a) Event 5 fitted functions. This height-time plot shows the functions fitted on the data during the analysis. Shifting the parabolic and the power-law functions by 0.002 $R_\odot$ helped distinguish the models on the height-time plot.

	Power law	**Parabolic**	**Exponential**	**Prop. Linear**
a	-4.89 ± 0.42	-0.398 ± 0.057	-178624 ± 130350	-
b	285.5 ± 8.2	276.6 ± 12.4	302.3 ± 6.2	131 ± 11
c	156926 ± 2630	153670 ± 3938	163496 ± 2191	199967 ± 5161
d	-	-	0.00097 ± 0.00056	-
χ^2_ν	0.399	1.574	0.227	1.360
df	3	3	2	3
p	0.754	0.207	0.634	0.253

(b) Event 5 fit parameters. The employed functions are as follows: the power-law $a(t-t_0)^{1.18}+b(t-t_0)+c$, the parabolic $a(t-t_0)^2+b(t-t_0)+c$, the exponential $ae^{d(t-t_0)}+b(t-t_0)+c$ and the linear $bt+c$. For the power-law and the parabolic profile a represents respectively the variation in the acceleration [km/s$^{\mathrm{m}}$], and the acceleration itself [km/s^2]. For all of them, b is the averaged velocity of the prominence [km/s] and c the initial height of the prominence [km]. For the exponential, d [1/s] combined with a [km] is another coefficient that represents the variation in the acceleration. χ^2_ν is the reduced chi square, df the degrees of freedom and p the p-value.

Figure 4.35: Event 5: Fit results. The resulting analysis concerns the high cadence data.

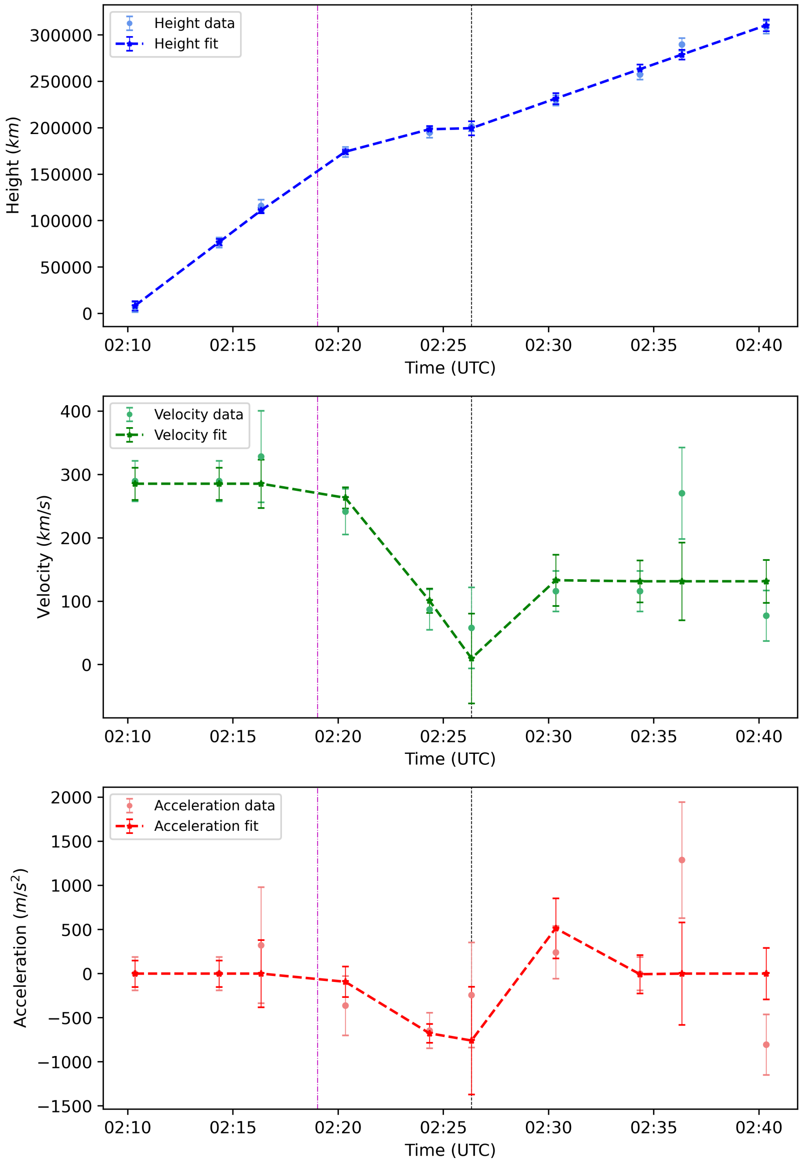

Figure 4.36: Event 5 kinematics. Distance from the limb (height) in [km] are shown, "Height fit" represents the fit for the early phase and acceleration phase (*top*). "Velocity" (green dots) is calculated from the differential of the height data in time [km/s]. The green dashed line represents the differential calculated from the linear function called "Fitted velocity" (*middle*). "Acceleration data" are calculated from the differential of velocity in time [m/s^2], and the red dashed line represents the "Fitted acceleration" differential calculated from the fitted velocity (*bottom*). A black dotted line is placed at t_f, while the pink one represents the time where the prominence is seen to start decelerating (t_d).

4.5.3 Influence of the surrounding corona

As said before, the presence of a sudden brightening, jetting activity, plasmoids, etc. at the site of an eruption may be indicative of magnetic reconnection occurring at the site (refer to Section 1.2.6 for more details). In this jet-like event, the footpoints are not observed in FSI images. However, when examining AIA 304 images (see Figure 4.37), I made the discovery that the prominence does not originate at the equatorial region (position angle of around 264°), but rather from an active region nine degrees below the equatorial region (at a position angle of around 255°), from a region slightly at the backside of the Sun. Consequently, the prominence was significantly deflected towards the northern hemisphere, possibly due to the coronal hole on the southern side of the Sun, which was previously discussed for Event 3 (4.3) and Event 4 (4.4). Taking into account the relative position of SolO with respect to SDO (as described in Section 2.4.2), there is an angular difference of approximately 18 degrees. Thus, the prominence should be 18° behind the limb in the FSI images.

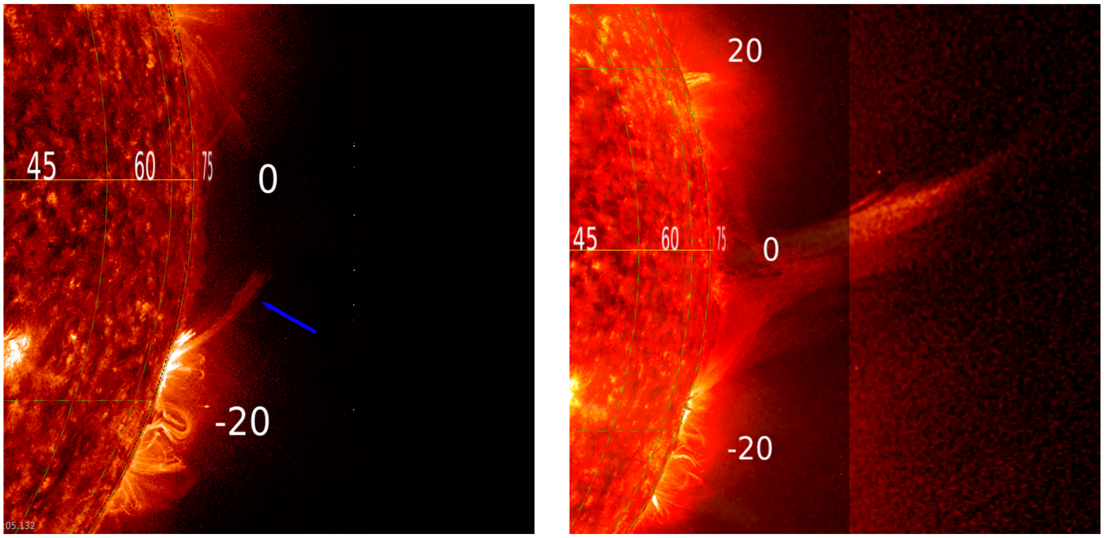

Figure 4.37: Event 5 observed on 2022-02-13. The prominence is observed to originate in an active region of the Sun in SDO/AIA 304 image (*left*). The prominence observed by both FSI 304 (larger FOV) and AIA 304 images (*right*).

To analyze the corona surrounding the eruption I also looked at the images recorded by FSI 174 and at the PFSS extrapolation provided in jHelioviewer (for a short description of the PFSS method see Section 1.2.4). All these elements are visible in Figure 4.38. According to the PFSS model, the prominence is located near several magnetic loops and open magnetic field lines. Therefore, the prominence is observed to follow the path of these open magnetic field lines up to a large distance. The presence of magnetic loops is also suggested by observations in FSI 174, where the prominence is somewhat challenging to distinguish but can be observed at the site of an active region of the Sun.

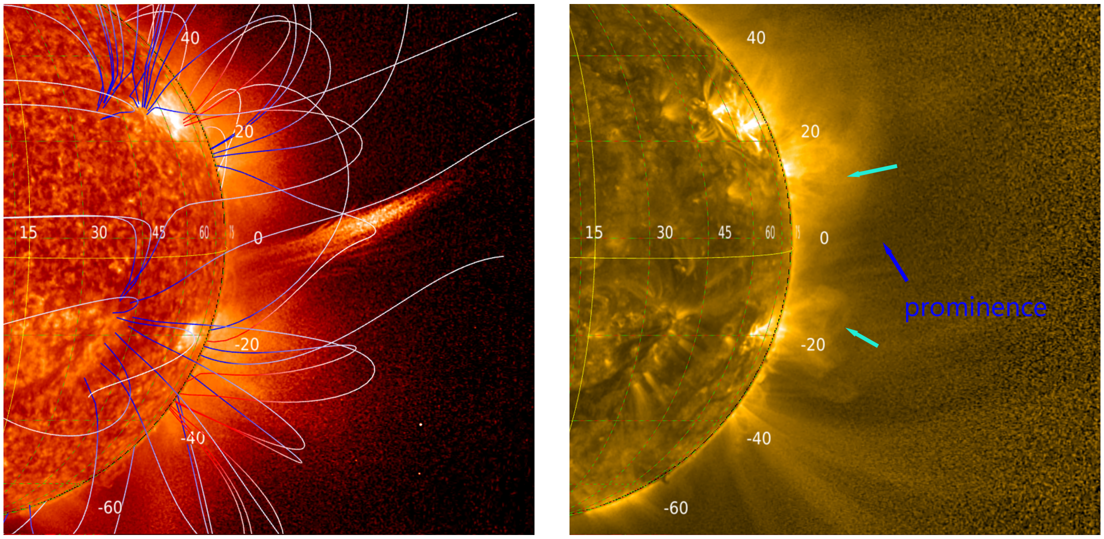

(a) 2022-02-13 02:56:20 UT. FSI 304 Å. **(b)** 2022-02-13 02:56:20 UT. FSI 174 Å.

Figure 4.38: Event 5. The PFSS model of the solar magnetic field lines is shown overplotted on the data of 2022-02-13 02:56:50 UT (*left*). The prominence is quite faint in FSI 174 (*right*), but it is located at the blue arrow. One can distinguish some closed loops pointed out by the light-blue arrows.

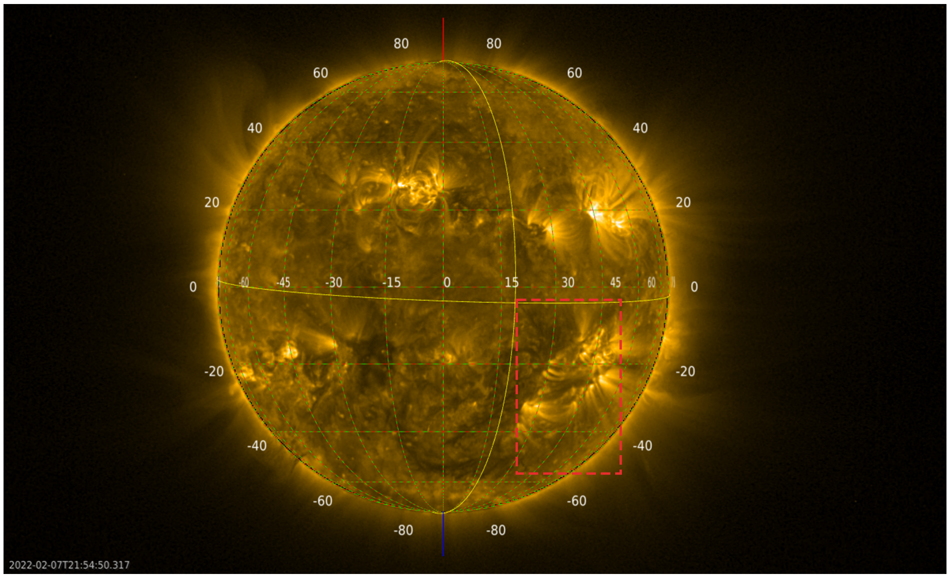

Figure 4.39: Sun observed on 2022-02-07. Images from FSI 174 captured a few days prior to the eruption. The red box highlights the region believed to be in proximity to the eruption site.

4.5.4 Discussion

The analysis conducted so far suggests that the fitting functions do not represent well enough the profile of the erupting prominence. The first data points observed in FSI do not coincide with the initial stage of the eruption, which is observed at earlier times in AIA images. Thus, the initial stage observed in FSI could be compatible with the last scenario of an acceleration phase. After that, the prominence is observed to decelerate quite fast. This event is observed to be highly deflected into the northern hemisphere of the Sun and reaching high speeds. The deflection could be attributed to the proximity to an active region and to the CH in the South of the Sun (see Section 1.4.8 for more details). Typically slow and narrow events are more affected by deflection. However, it is important to note that the measurements were taken after the event had already undergone acceleration, so we do not have precise information regarding its initial speed. It remains plausible that the deflection observed in this event could be attributed to the coronal hole.

Although the deflection may have affected the measurements, this particular event was observed to originate approximately 18° behind the limb, similar to what was observed for Event 4 (See Section 4.4). As mentioned in Section 3.3.2, the projection effect has the potential to become the primary source of error when measuring prominence heights and might necessitate correction when it becomes feasible to determine the angle at which the prominence is situated in relation to the limb. In Figure 3.3 I reported the average discrepancy at increasing angle behind the limb. In the case of 20° the difference between the measured height and the true height of the prominence is 6.03 %. This value is still comparable with the other sources of uncertainties. However, taking into account that the prominence likely doesn't maintain a constant angle throughout its motion, this factor could potentially have an even greater impact. This, combined with the fact that the prominence does not move radially, could explain the discrepancies observed in the analysis.

Regarding the cadence analysis, it was not possible to conduct it for this event due to the insufficient number of data points.

4.6 Event 6

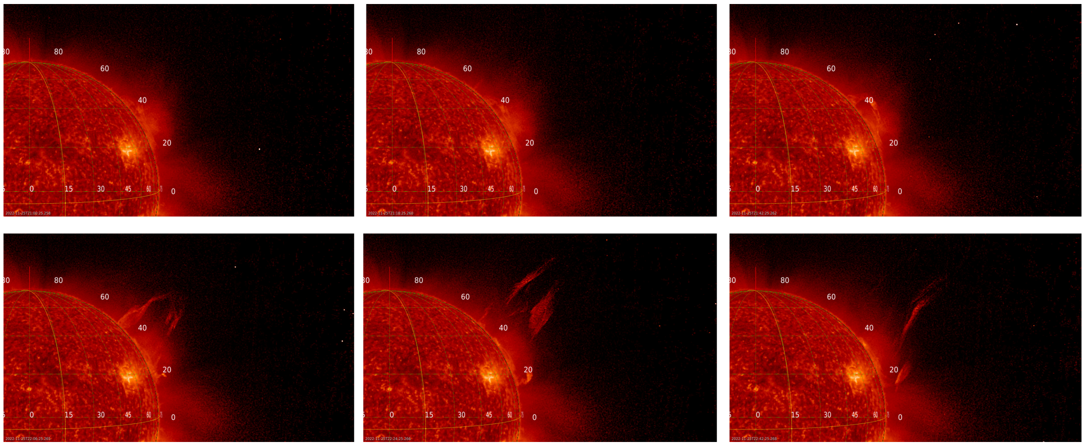

Figure 4.40: Event 6 observed on 2022-11-25. Sequence of images at increasing time.

The last eruption studied ("Event 6") is a loop-like prominence occurring in the North-West region of the Sun (4.41b) on the 25th of November, 2022 (see Figure 3.1f). It seemed to start erupting at around 21:00 UT at a height of 0.07 $R_\odot$ above the limb and, despite reaching a large distance, the leading point could be correctly followed until a height of 0.49 $R_\odot$ at 22:06 UT. The evolution of the prominence is presented in Figure 4.40. The measurement procedure involves tracking the prominence's motion (three times) along the direction indicated by the black arrow in Figure 4.41a. In the figure it can be seen that the position angle of the prominence varies very little during its propagation. Thus, it can be considered a radially moving prominence. The images are taken every 6 minutes and the prominence is really fast (it reaches a speed of about 190 km/s), so only 10 points could be measured.

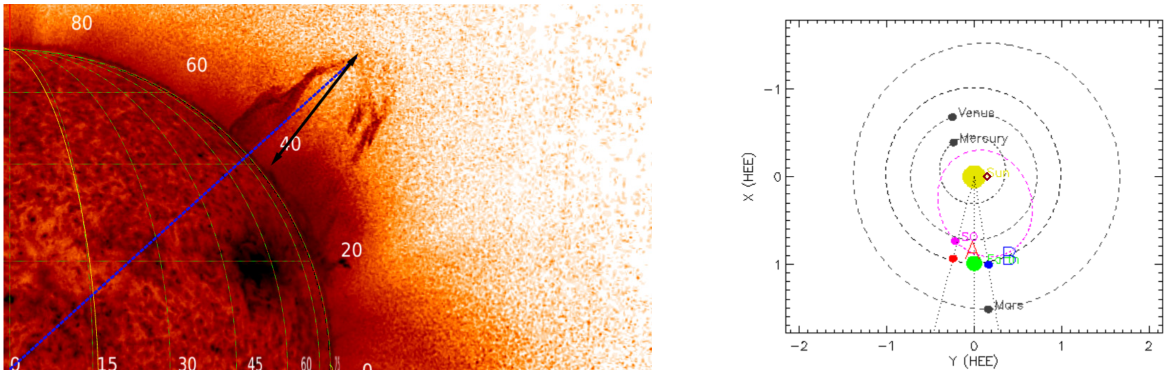

(a) 2022-11-25 22:06:25 UT. The black arrow points to the tip of the prominence under study while propagating. The blue dashed line indicates the radial direction of the leading point.

(b) Event 6 relative position at 21:00 UT. The red rhombus roughly indicates the location of the solar eruption. For more details refer to Section 2.4.2.

Figure 4.41: Event 6 observed on 2022-11-25.

4.6.1 Initiation mechanisms

High cadence analysis The averaged distance and position angle over time are presented in Figure 4.42. The left panel shows the height-time plot where it seems that only the slow rise and the acceleration phases are observed. On the right panel one can observe the position angle of the prominence over time. The angle varies by around two degrees, which confirms that the prominence is moving almost radially. The raw data and the averaged ones are shown in Table 4.12.

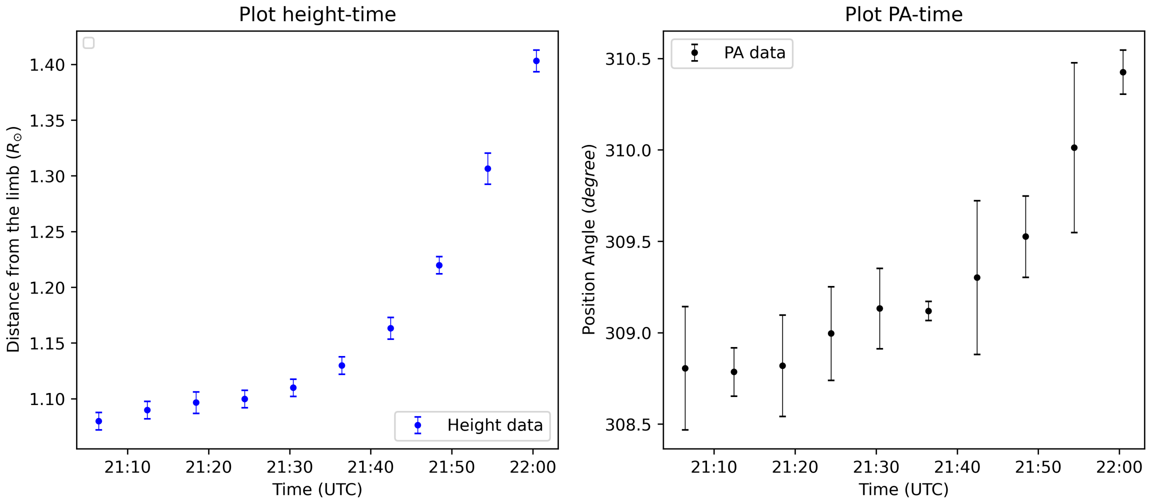

Figure 4.42: Event 6 height-time and PA-time plots. The left panel shows the height and the right panel shows the angular position of the prominence, both as function of time.

The initial phase of the analysis involves determining the onset of the acceleration phase for the erupting prominence (t_0), the same procedure as outlined in Section 3.4.1. The various attempts are presented in Table 4.6 for which the power-law returns a value t_0=21:27 UT ($t_0 = 1442 \pm 149$ s), with $m = 2.011 \pm 0.225$ at a height of around 0.11 $R_\odot$ above the limb, emphasized with a yellow row where the minimum value for chi square is found. This choice is justified by the fact that there are no values close to 1, the chi square values are too small probably due to an overestimation of the errors or over-fitting of the model.

At this point, I fitted different functions: the power-law with $m = 2.011$, the parabolic, and the exponential, following the procedure explained in Section 3.4. The power-law returned a value close to

Initial time	Final time	Input t_0	Best t_0	m	χ^2_ν
21:06	22:00	21:18	21:27	2.33	0.455
21:06	22:00	21:24	21:25	2.18	0.554
21:06	22:00	21:06	21:06	2.07	5.073
21:06	22:00	21:30	21:30	2.01	0.126

Table 4.6: EVENT 6 MINIMIZING χ^2. "Initial time" is the time of the first data measurement, "Final time" is the time when the acceleration phase is supposed to end, "Input t_0" is the input time to the python script and best t_0 is the best estimator for it. m and χ^2_ν are the exponent and the reduced chi square values respectively. The yellow row is the one that minimizes the chi square.

2, now with $\chi^2_\nu = 0.997$ which is highly close to 1. The parabolic fit instead provides $\chi^2_\nu = 0.109$. The exponential fit returns $\chi_\nu = 0.249$. Although all the functions represent well the data, the parabolic fit minimizes the chi-square and yields fit parameters with lower uncertainties. Furthermore, the power-law with free parameters gave a coefficient that happens to coincide with 2. Therefore, we select the parabolic fit as the most suitable choice. A chi-square value this low can be rationalized by the fact that the errors in height may be likely greater than the disparity between the data and the model.

The p-value reflects the probability that the observed data aligns with the null hypothesis, which assumes that the regression model used represents the data accurately. However, when the p-value is greater than the significance level (0.05), it implies a lack of statistical significance. Consequently, we cannot either confirm or reject the null hypothesis (see Section 3.4.3).

LOW CADENCE ANALYSIS The low cadence analysis was not conducted for this particular event. Combining the cadence of 6 minutes with the fact that the event was moving at a relatively high speed it allowed me to collect only 10 data points of the tracked prominence feature. Further reduction in the number of data points would not have been suitable for conducting a meaningful statistical analysis.

4.6.2 Kinematic analysis

I investigated the velocity and the acceleration of the prominence during its propagation.
I calculated these quantities using the two different methods outlined in Section 3.5: I calculated the velocity from the measured heights (1) and from the heights performed with the best fit function (2). The latter allows to obtain quantities close to the former, but with less uncertainty. Thus in the analysis I report the latter. The results can be observed in Figure 4.44. The upper panel shows the height of the prominence in [km] and the best-fit function, the parabolic fit. In the middle and bottom graphs, the velocity and the acceleration are shown.

During the slow rise, the prominence is observed to move with an averaged constant velocity of:

$$v_0 = 13.6 \pm 2.0 \text{ km/s} \tag{4.16}$$

which is compatible with the b coefficient obtained through the parabolic fit, i.e. $b = 13.57 \pm 0.97$ km/s in Table 4.43b. The b parameter represents the initial velocity of the prominence. The averaged acceleration in this interval is zero, i.e. $a_0 = -0.0 \pm 9.0$ m/s^2.

After 21:30 UT the prominence is seen to accelerate reaching a maximum value of $v_{max} = 187 \pm 33$ km/s. Note that this is not an average, but the maximum value recorded. The averaged acceleration in this interval is:

$$a = 88.2 \pm 8.1 \text{ m/s}^2 \tag{4.17}$$

and it should be comparable with the acceleration term in the parabolic fit. The acceleration in a parabolic profile is given by $2a_{fit}$ where $a_{fit} = 56.0 \pm 1.0$ m/s^2 is the parameter associated with the second order term. Thus the expected acceleration should be around $a_{exp} = 112.0 \pm 2.0$ m/s^2. The latter is compatible with the averaged acceleration obtained in equation 4.17.

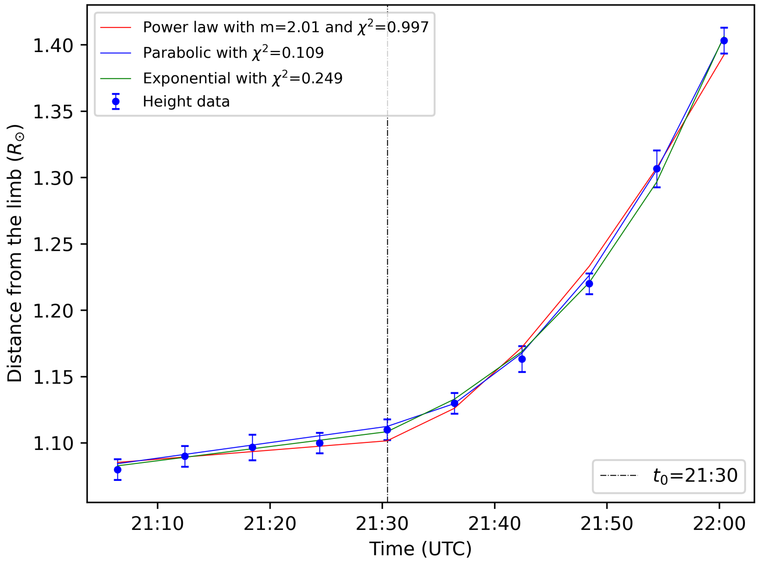

(a) Event 6 fitted functions. This height-time plot shows the functions fitted on the data during the analysis. Shifting the parabolic and the power-law functions by 0.002 $R_\odot$ helped distinguish the models on the height-time plot.

	Power law	**Parabolic**	**Exponential**
a	1.170 ± 0.070	0.0556 ± 0.0010	37875 ± 5152
b	7.9 ± 3.5	13.57 ± 0.97	12.4 ± 2.0
c	766403 ± 2792	771866 ± 780	770490 ± 1727
d	-	-	0.001039 ± 0.000064
χ^2_ν	0.997	0.109	0.249
df	7	7	6
p	0.431	0.995	0.941

(b) Event 6 Fit parameters.The employed functions are as follows: the power-law $a(t-t_0)^{2.011}+b(t-t_0)+c$, the parabolic $a(t-t_0)^2+b(t-t_0)+c$, the exponential $ae^{d(t-t_0)}+b(t-t_0)+c$. For the power-law and the parabolic profile a represents respectively the variation in the acceleration [km/s$^{\mathrm{m}}$], and the acceleration itself [km/s^2]. For all of them, b is the averaged velocity of the prominence [km/s] and c the initial height of the prominence [km]. For the exponential, d [1/s] combined with a [km] is another coefficient that represents the variation in the acceleration. χ^2_ν is the reduced chi square, df the degrees of freedom and p the p-value.

Figure 4.43: Event 6: Fit results. The resulting analysis concerns the high cadence data.

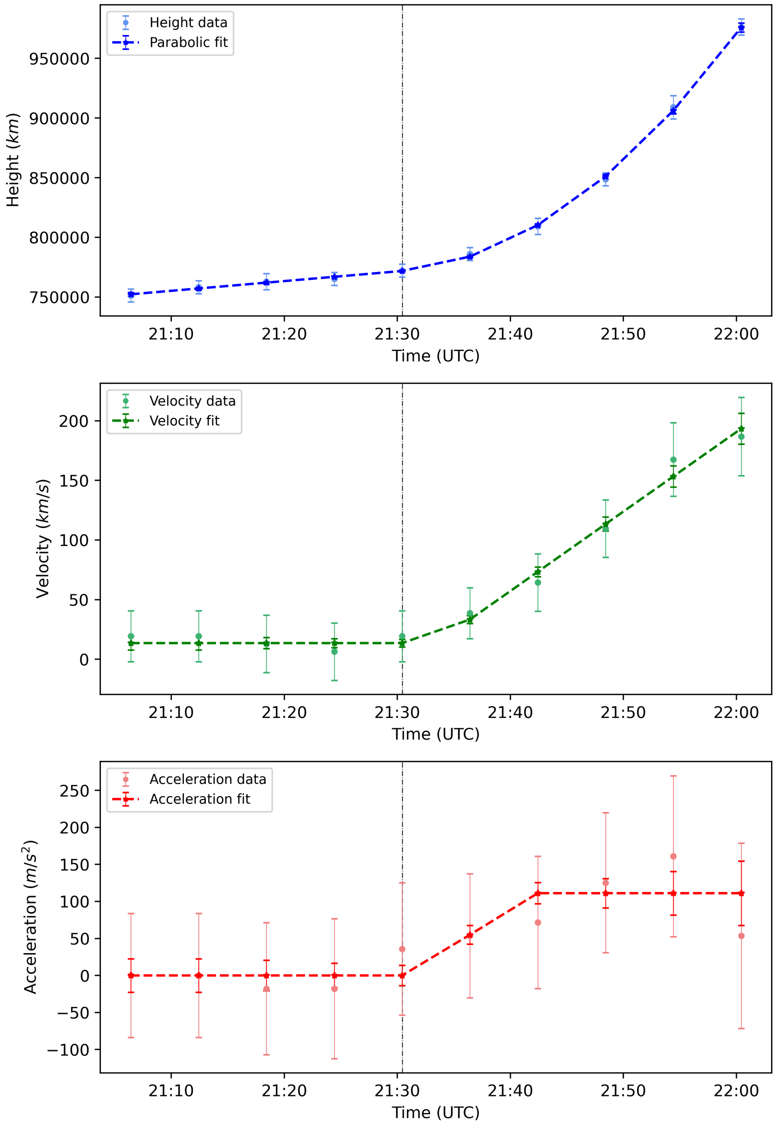

Figure 4.44: Event 6 kinematics. Distance from the limb (height) in [km] are shown (*top*). "Velocity" (green dots) is calculated from the differential of the height data in time [km/s]. The green dashed line represents the differential calculated from the linear function called "Fitted velocity" (*middle*). "Acceleration data" are calculated from the differential of velocity in time [m/s^2], and the red dashed line represents the "Fitted acceleration" differential calculated from the fitted velocity (*bottom*). A black dotted line is placed at t_0.

4.6.3 Influence of the surrounding corona

Searching for sudden brightening, current sheets, plasmoids, etc. in the eruption site may be indicative of the presence of magnetic reconnection (see Section 1.2.6 for more details). However, the footpoints appear to originate at or slightly behind the solar limb from SolO's perspective. But they are well observed by instruments on other missions, such as SDO and STEREO-A. An image obtained from SDO/AIA 304 is displayed in Figure 4.45b. In this image, you can observe a burst of light in the southernmost leg of the eruption. It looks like during the primary eruption, there is a further release of matter occurring in the southern leg. This phenomenon is also visible in FSI 304 (Figure 4.45a), accompanied by bursts of light beneath the leading point of the prominence itself. This can be indicative of a sudden release of energy, i.e., it may be associated with magnetic reconnection.

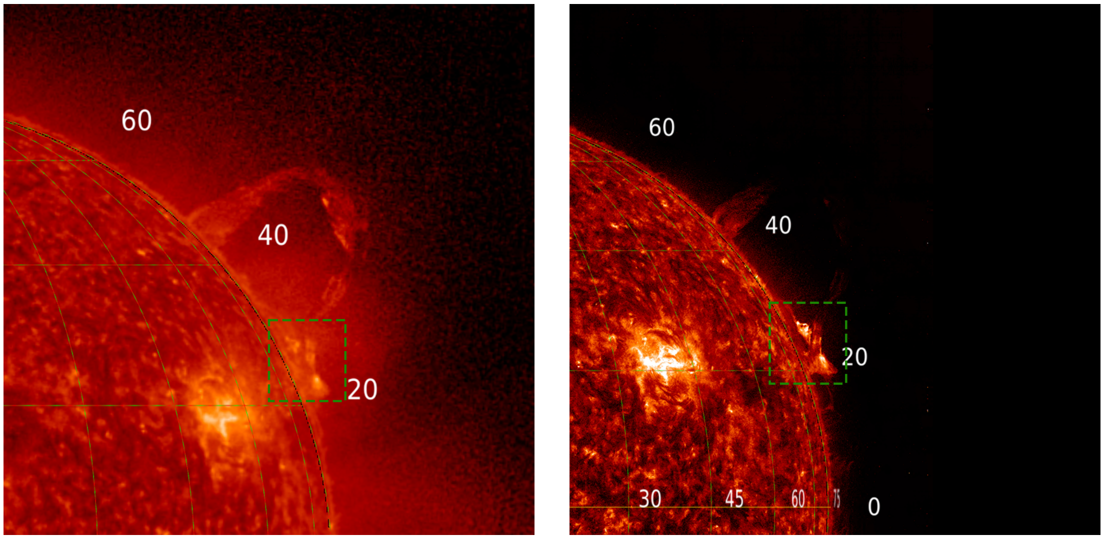

(a) 2022-11-25 21:54:25 UTC. Some bursts of light observed at one of the footpoints and on the arch of the prominence itself.

(b) 2022-11-25 21:56:29 UTC. The erupting prominence as seen in SDO/AIA 304.

Figure 4.45: EVENT 6. Additional images from SolO and SDO. The red box highlights the brightness occurring on one of the legs of the prominence.

To analyze the corona surrounding the eruption I also looked at the images recorded by FSI 174 and at the PFSS (1.2.4) extrapolation provided in jHelioviewer. All these elements are visible in Figure 4.46. According to the PFSS model, the prominence is located near several magnetic loops, which indicates the presence of an active region. The presence of magnetic loops is also suggested by observations in FSI 174, where the prominence is somewhat challenging to distinguish but can be observed near an active region of the Sun. This can be confirmed to be associated with a multipolar magnetic region looking at the SOHO/MDI Magnetogram images.

4.6.4 Discussion

The analysis conducted so far suggests that a parabolic function provides the best model for this eruption. This implies that the prominence experiences a relatively constant acceleration. This finding aligns with the breakout model, which incorporates the concept of magnetic reconnection to explain the acceleration of eruptive phenomena. To support this model, the presence of a quadrupolar region of magnetic flux is necessary, and such a region could potentially emerge within an active region as a result of interactions between magnetic field lines as observed for this particularly event. Lastly, the eruption is moving almost radially and seems to occurs at the limb. Regarding the cadence analysis, it was not possible to conduct it for this event due to the insufficient number of data points.

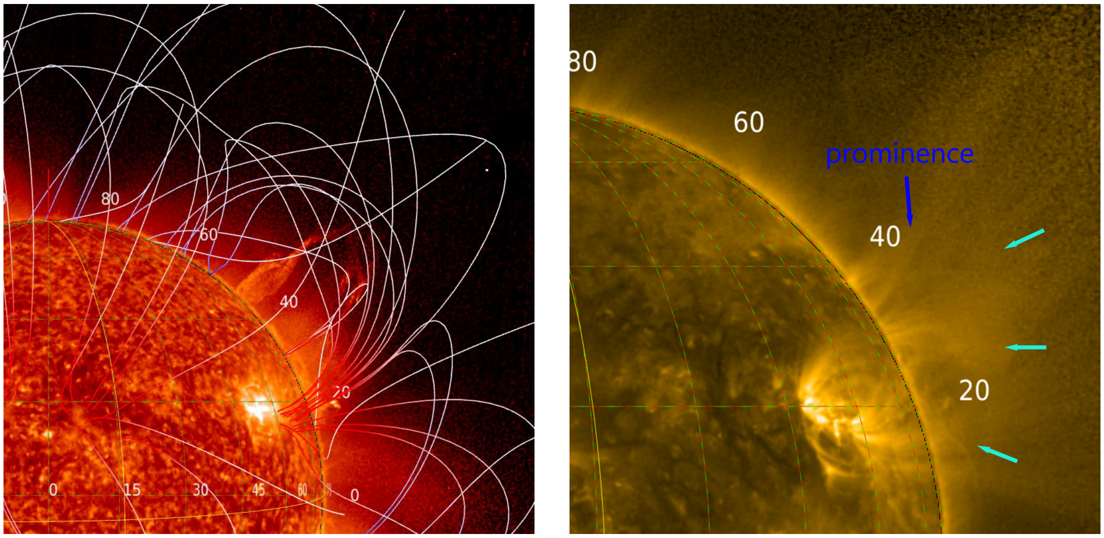

(a) FSI 304 Å. **(b)** FSI 174 Å.

Figure 4.46: Event 6. The PFSS model of the solar magnetic field lines is shown over plotted on the data of 2022-02-13 20:14:00 UT (*left panel*). The prominence is quite faint in FSI 174 (*right*), but it is located at the blue arrow. One can distinguish some overlying loops in the site pointed with the light-blue arrows.

Conclusion

This study was motivated by our limited understanding of the acceleration processes involved in eruptive events, encompassing phenomena like erupting prominences, CMEs, and flares. The objective was to refine their characterization and enhance overall understanding. The approach to achieve this was by analyzing these events in detail and investigating their underlying eruption mechanisms.

There has been some progress in understanding the propagation phase (i.e. the third phase of the three-part kinematic profile) of CMEs, which is believed to be primarily driven by the drag force of the solar wind from a certain altitude onward [102]. The early phase of the kinematic profile characterizing an erupting prominence, as well as a CME, encompassing the slow rise and the impulsive acceleration phases, remains inadequately understood [124]. Presently, the impulsive acceleration phase can be attributed to two primary mechanisms: magnetic reconnection and MHD instability.
Several studies have attempted to elucidate initiation mechanisms by interpolating the curvature in the kinematic profile with various functions (Schrijver et al., 2008 [105], Mierla et al., 2013 [74]). This approach can yield different results, shedding light on diverse processes at play, such as for example large-scale relaxation of the magnetic topology [74]. In this analysis, we explored erupting prominences characterized by distinct properties, primarily focusing on loop-like events, with the exception of a jet-like eruption. Additionally, we investigated cases of radial propagation or deflection ranging from weak to strong.

Data points for each of the six events studied here, are presented within a unified graph in Figure 4.47, including best-fit curves for the slow-rise and acceleration phases.

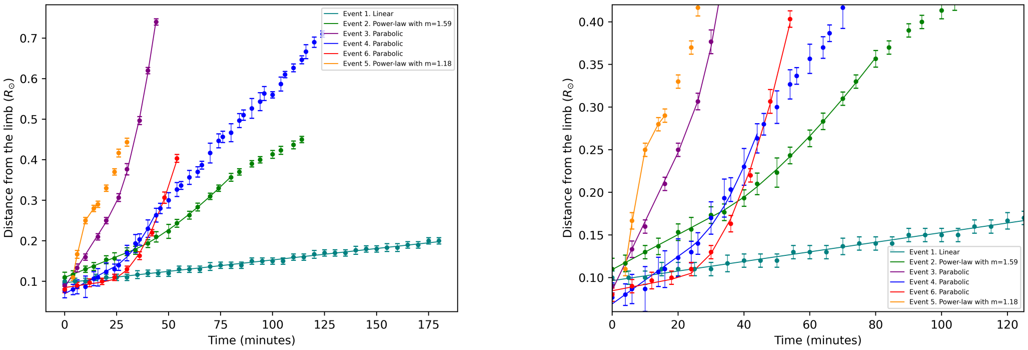

Figure 4.47: Height-time plot depicting all six events analyzed in this study. The heights over time for each event are represented using distinct colors. The best-fit functions are displayed, capturing only the early phase of the eruptions, i.e. the slow rise and the acceleration phases (*left*). The same plot zoomed up to 0.42 $R_\odot$ to emphasize the early phase data (*right*).

The graph reveals significant variability among the events. While some prominences persist for extended durations with a constant velocity (Event 1), others exhibit a parabolic profile marked by varying initial velocities and accelerations (Events 3, 4, 6). For certain events (Event 2, Event 5), it was challenging to associate them with previously reported initiation mechanisms models from the literature. The identification of the initiation mechanisms is strongly related to the magnetic environment in the low corona where these phenomena occur. Indeed, understanding the intricate dynamics of the magnetic field at the eruption site is crucial. It allows us to predict which acceleration mechanism will influence the prominence, subsequently enabling us to estimate its velocity and, consequently, the rate at which a potential CME may propagate into the heliosphere, possibly reaching Earth. These insights offer valuable predictive capabilities for estimating the timing and intensity of geomagnetic storms that can impact our planet.

However, it is worth noting that several factors have been observed to influence the outcomes of our analysis, introducing some discrepancies and challenges in associating initiation mechanisms with the observed height-time plots. Firstly, non-radial propagation has been a significant factor. It is evident that additional lateral forces acted upon prominences, causing them to deviate from their expected radial direction. This deviation was particularly noticeable in events 4 and 5, primarily associated with the presence of CHs in the southern hemisphere of the Sun and ARs. Both of these factors can act as barriers, driving the prominence or CMEs to propagate away from them and leading to non-radial propagation. This underscores the importance of considering the surrounding corona's role, alongside the eruption mechanism. While the eruption mechanism can provide information on how the prominence erupts, it doesn't determine its trajectory. Understanding under what conditions these events can be deflected is crucial. Predicting whether a prominence will be deflected, along with information on the extent and direction of CME deflection, is vital in assessing the potential impact of such events on Earth.

Another limitation pertains to the projection effect, where if the prominence does not propagate in the plane of the sky, it can become a primary source of error, especially when the prominence is not observed directly on the solar limb but slightly behind or in front of it. The discrepancy between the actual height of the prominence and what we measure increases as the direction of propagation deviates from the limb. For several events, we recognized that the prominences were situated less than 20° away from the plane of the sky, resulting in a discrepancy of about 6% (confirmed for events 3, 4, 5, and 6). While this is comparable to other sources of uncertainty, it can increase significantly if the angle varies during the measurement and the event is further deflected during its propagation. Additionally, if the prominence is behind the Sun, crucial information about the start of the eruption, including the slow phase, the beginning of the acceleration phase, and in the worst-case scenario, the entire acceleration phase, can be missed.

Additionally, a noteworthy correlation has been suggested through the comparison of different data cadence analyses. A study conducted by Byrne et al., (2013) [18] delved into the influence of sampling cadence on deriving kinematics from coronal mass ejections (CMEs) and coronal waves. Their findings underscored the importance of higher cadence data and a larger sample size for achieving precise estimations of velocity and acceleration. Furthermore, a recent study by Vashishtha et al. (2023) [124] corroborated these observations. It demonstrated that while the calculated average velocity of CMEs exhibits limited dependence on imaging cadence, the average acceleration is notably affected, decreasing with lower frequency data. The reduced cadence also has implications for estimating the onset time of acceleration.

In this work, the most significant observation in this sense was made for Event 2 and Event 4. In both cases, cadence influenced the accurate detection of curvature in the height-time plots, particularly in estimating the m parameter of the power-law. Low cadence analysis sometimes provided partial information, such as the transitions between different velocity regimes, resulting in the loss of curvature information. This is of paramount importance, as it has the potential to lead researchers to select a different profile and, consequently, an entirely different initiation mechanism associated with the eruption. Both a larger dataset and higher data recording frequency are crucial not only for determining the kinematics of these events but also for exploring their initiation mechanisms. Therefore, a higher observation frequency can offer advantages in data analysis and in characterizing the kinematics of eruptive phenomena.

To summarize, four out of six within the studied events are consistent with a parabolic profile. Lynch et al., 2004 [68] associated such a trajectory with a Breakout-type instability scenario. In this model proposed by Antiochos et al., 1999 [8], CMEs and their precursors, including erupting prominences, undergo acceleration through magnetic reconnection in a quadrupolar-type structure. The intersection point of these flows can deform, leading to the formation of a current sheet. This process eliminates higher magnetic loops confining the eruption, facilitating its expansion. Furthermore, the rise of the central flux-rope results in the formation of a second current sheet below the prominence, causing a second reconnection event which actually drives the prominence eruption, ejecting the flux rope into the heliosphere, and forming the CME. These findings align well with the existing literature. Several studies (e.g. D'Huys et al. 2014 [31], and Cheng et al., 2020 [24]) aimed to associate profiles obtained from height-time plots for numerous CMEs. Chen et al., 2020 [24] studied 12 CMEs finding that in all the cases the initial phase aligns with a linear fit (slow rise) and an exponential profile (indicative of MHD instability). D'Huys et al., 2014 [31] conducted another study with a larger sample of 40 CMEs, demonstrating that height-time plots could be fitted with both exponential (MHD instability) and parabolic profiles (breakout model). This research proposes that the breakout instability could serve as a plausible mechanism for at least some prominence eruptions associated with coronal mass ejections. However, since nonlinear models are sensitive to the specifics of boundary and initial conditions, further exploration is required to assess how alternative models for erupting prominences align with the observed data. Additionally, it is essential to enhance the fidelity of different models and data before drawing definitive conclusions about the mechanism(s) responsible for prominence eruptions in general.

Limitations of the observations

While the FSI field of view (FOV) allows us to observe the prominence at higher positions in the corona, it wasn't always feasible to track the same feature all the way to the end of the FOV. This could happen due to various factors, such as changes in the shape of the prominences, their faintness, or becoming indistinguishable from the image noise. As a result, the number of points available for the height-time analysis was limited.

In addition, it was also observed that the obtained values for the reduced chi-square were generally very small (much less than 1). This indicates that the discrepancy between the model and the data is much smaller than the uncertainties associated with the measurements. This phenomenon typically occurs for two reasons. The first reason is *overfitting.* This arises when a statistical model starts to capture random errors in the data rather than focusing on the relationships between variables. It could happens for several reasons, e.g., the model is overly complex to describe the data. This can impede the model's ability to generalize and predict outcomes for new data. This phenomenon was noticed, especially in Event 1, where all models featuring a second-degree term seemed to fit the data nicely. However, they were essentially behaving like a linear model because the coefficients for the second-order terms were close to zero. Moreover, across all six events, it was consistently observed that the exponential function resulted in a low chi-square value, but at the same time, the exponent was nearly zero.

The second reason is frequently associated with an overestimation of the measurement variance. In this study, measurement uncertainty depends on several factors, including the resolution of the FSI images and how frequently the images were taken. In the study of Schrijver et al. in 2008 [105], the authors relied on a combination of various instruments, which allowed them to observe the Sun with a spatial resolution of 1 arcsec (1/10th of that offered by FSI) and at a higher cadence, with images captured every 20 seconds. This approach led to smaller uncertainties in height measurements and resulted in reduced chi-square values that hovered around 1. This implies that enhancing the precision of measurements could lead to statistically more significant results, making it clearer which model or models best represent the data.

Future improvements

Improvements in this type of data analysis can be achieved through the combination of various instruments. Solar features in different images can then be combined through three-dimensional reconstruction using the triangulation technique [52]. For instance, it has been observed that in the case of Event 5, images obtained from AIA 304 were able to capture the event before it was recognizable by FSI 304. In this particular scenario, using only the images from FSI 304 proved insufficient to gather information about the curvature of the event and infer an initiation mechanism by comparing it with numerical simulations. Additionally, observations from different perspectives can better constrain the shape of the prominences. Future observations from Solar Orbiter, taken at different latitudes, will provide new insights into the morphology and propagation of erupting prominences in three dimensions. Therefore, combining data from multiple instruments also enables us to observe eruptions with higher frequency, leading to more precise measurements. As previously mentioned, relying solely on FSI data failed to clarify the eruption site. Understanding the eruption site is crucial as it can constrain the initiation mechanisms responsible for the eruption and provide insights into the occurrence of magnetic reconnection based on its observational signatures. However, a comprehensive investigation is necessary to validate the occurrence of magnetic reconnection. This entails conducting a deeper analysis, considering the orientation of the magnetic field and its changes before and after the eruption. This specific aspect has not been explored in the current study, but it has the potential to significantly enhance our understanding of the observed phenomena. Furthermore, to identify a common pattern among different eruptions, it is essential to expand the sample size to include a more extensive range of events. Ideally, these observations should be conducted at a high cadence to maximize the available data points for analysis.

Appendix

Raw data and averaged values

Below, I provide the values of the measurements performed for the prominence's feature tracked during its eruption: the distance from the Sun's center and the angle relative to the Sun's North. Additionally, I include the average values and their associated uncertainties. For a comprehensive explanation of how these values were calculated, please refer to Section 3.2.1.

time	d	θ	d	θ	d	θ	$\langle d \rangle$	$\langle \theta \rangle$
15:10:20	1.09	132.00	1.09	131.89	1.09	131.64	1.090 ± 0.008	131.8 ± 0.2
16:15:20	1.10	131.74	1.10	131.56	1.10	131.27	1.100 ± 0.008	131.5 ± 0.2
16:20:20	1.10	131.77	1.10	131.53	1.10	131.23	1.100 ± 0.008	131.5 ± 0.3
16:25:20	1.11	131.67	1.11	131.39	1.11	131.28	1.110 ± 0.008	131.4 ± 0.2
16:30:20	1.11	131.59	1.11	131.39	1.11	131.01	1.110 ± 0.008	131.3 ± 0.3
16:35:20	1.11	131.57	1.11	131.47	1.11	130.83	1.110 ± 0.008	131.3 ± 0.4
16:40:20	1.11	131.55	1.11	131.37	1.11	130.92	1.110 ± 0.008	131.3 ± 0.3
16:45:20	1.11	131.61	1.12	131.38	1.12	130.97	1.117 ± 0.010	131.3 ± 0.3
16:50:20	1.12	131.62	1.12	131.31	1.12	130.83	1.120 ± 0.008	131.3 ± 0.4
16:55:20	1.12	131.60	1.12	131.32	1.12	130.87	1.120 ± 0.008	131.3 ± 0.4
17:00:20	1.12	131.64	1.12	131.39	1.12	130.97	1.120 ± 0.008	131.3 ± 0.3
17:05:20	1.13	131.60	1.13	131.56	1.13	131.02	1.130 ± 0.008	131.4 ± 0.3
17:10:20	1.13	131.66	1.13	131.64	1.13	131.02	1.130 ± 0.008	131.4 ± 0.4
17:15:20	1.13	131.56	1.13	131.81	1.13	131.03	1.130 ± 0.008	131.5 ± 0.4
17:20:20	1.13	131.59	1.14	131.81	1.14	131.01	1.14 ± 0.01	131.5 ± 0.4
17:25:20	1.14	131.60	1.14	131.82	1.14	130.98	1.140 ± 0.008	131.5 ± 0.4
17:30:20	1.14	131.56	1.14	131.68	1.14	131.10	1.140 ± 0.008	131.4 ± 0.3
17:35:20	1.14	131.49	1.14	131.58	1.14	131.07	1.140 ± 0.008	131.4 ± 0.3
17:40:20	1.15	131.45	1.15	131.69	1.15	131.04	1.150 ± 0.008	131.4 ± 0.3
17:45:20	1.15	131.53	1.15	131.63	1.15	131.01	1.150 ± 0.008	131.4 ± 0.3
17:50:20	1.15	131.43	1.15	131.49	1.15	130.91	1.150 ± 0.008	131.3 ± 0.3
17:55:20	1.15	131.43	1.15	131.43	1.15	131.00	1.150 ± 0.008	131.3 ± 0.2
18:00:20	1.16	131.66	1.16	131.44	1.16	131.04	1.160 ± 0.008	131.4 ± 0.3
18:05:20	1.16	131.67	1.16	131.63	1.16	131.13	1.160 ± 0.008	131.5 ± 0.3
18:10:20	1.17	131.68	1.16	131.64	1.16	131.25	1.17 ± 0.01	131.5 ± 0.2
18:15:20	1.17	131.61	1.17	131.66	1.17	131.19	1.170 ± 0.008	131.5 ± 0.3
18:20:20	1.17	131.67	1.17	131.84	1.17	131.16	1.170 ± 0.008	131.6 ± 0.4
18:25:20	1.17	131.66	1.17	131.87	1.17	131.24	1.170 ± 0.008	131.6 ± 0.3
18:30:20	1.18	131.66	1.18	131.96	1.18	131.19	1.18 ± 0.01	131.6 ± 0.4
18:35:20	1.18	131.60	1.18	131.98	1.18	131.27	1.180 ± 0.008	131.6 ± 0.4
18:40:20	1.18	131.57	1.18	132.03	1.18	131.31	1.180 ± 0.008	131.6 ± 0.4
18:45:20	1.18	131.61	1.19	132.19	1.19	131.32	1.18 ± 0.01	131.7 ± 0.4
18:50:20	1.18	131.61	1.19	132.27	1.19	131.32	1.18 ± 0.01	131.7 ± 0.5
18:55:20	1.19	131.67	1.19	132.23	1.19	131.32	1.190 ± 0.008	131.7 ± 0.5
19:00:20	1.19	131.63	1.19	132.21	1.19	131.41	1.190 ± 0.008	131.8 ± 0.4
19:05:20	1.20	131.50	1.20	132.07	1.20	131.46	1.200 ± 0.008	131.7 ± 0.3

Table 4.7: Event 1 Raw data and averaged values. For different times, d is the distance of the feature from the centre of the sun in solar radius ($R_\odot$), θ is the angular position of the feature in degree. $\langle\rangle$ values represents the averaged ones. The data used for the low cadence analysis is highlighted in blue.

$time$	d	θ	d	θ	d	θ	$\langle d\rangle$	$\langle\theta\rangle$
02:00:20	1.11	313.18	1.1	313.34	1.12	312.24	1.110 ± 0.013	312.9 ± 0.6
02:04:20	1.12	312.82	1.11	313.30	1.12	312.13	1.117 ± 0.010	312.8 ± 0.6
02:10:20	1.13	312.53	1.13	312.22	1.13	312.14	1.130 ± 0.008	312.3 ± 0.2
02:14:20	1.14	312.35	1.13	312.81	1.14	312.04	1.137 ± 0.010	312.4 ± 0.4
02:20:20	1.15	312.01	1.15	312.68	1.16	312.15	1.153 ± 0.010	312.3 ± 0.4
02:24:20	1.15	312.02	1.15	312.68	1.17	312.17	1.157 ± 0.014	312.3 ± 0.3
02:30:20	1.17	311.92	1.17	312.72	1.18	312.20	1.173 ± 0.010	312.3 ± 0.4
02:34:20	1.18	311.66	1.17	312.78	1.18	312.34	1.177 ± 0.010	312.3 ± 0.6
02:40:20	1.19	311.51	1.19	312.91	1.2	312.42	1.193 ± 0.010	312.3 ± 0.7
02:44:20	1.21	311.49	1.2	312.93	1.22	312.65	1.210 ± 0.013	312.4 ± 0.8
02:50:20	1.22	311.51	1.21	313.00	1.24	312.80	1.223 ± 0.017	312.4 ± 0.8
02:54:20	1.24	311.48	1.24	313.28	1.25	312.94	1.243 ± 0.010	312.6 ± 1.0
03:00:20	1.26	311.45	1.26	313.74	1.27	313.19	1.263 ± 0.010	312.8 ± 1.2
03:04:20	1.28	311.31	1.28	313.89	1.29	313.36	1.283 ± 0.010	312.9 ± 1.4
03:10:20	1.31	311.16	1.31	313.91	1.31	313.47	1.310 ± 0.008	312.8 ± 1.5
03:14:20	1.33	311.31	1.33	313.71	1.33	313.53	1.330 ± 0.008	312.9 ± 1.3
03:20:20	1.35	311.13	1.36	313.61	1.36	313.52	1.357 ± 0.010	312.8 ± 1.4
03:24:20	1.37	311.31	1.37	313.36	1.37	313.33	1.370 ± 0.008	312.7 ± 1.2
03:30:20	1.39	311.56	1.39	313.09	1.39	312.96	1.390 ± 0.008	312.5 ± 0.8
03:34:20	1.40	311.41	1.4	312.64	1.4	312.89	1.400 ± 0.008	312.3 ± 0.8
03:40:20	1.41	311.43	1.41	312.49	1.42	312.66	1.413 ± 0.010	312.2 ± 0.7
03:44:20	1.42	311.43	1.42	312.51	1.43	312.39	1.423 ± 0.010	312.1 ± 0.6
03:50:20	1.43	311.47	1.44	312.41	1.44	312.32	1.437 ± 0.010	312.1 ± 0.5
03:54:20	1.45	311.75	1.45	312.46	1.45	312.38	1.450 ± 0.008	312.2 ± 0.4

Table 4.8: Event 2 Raw data and averaged values. For different times, d is the distance of the feature from the centre of the sun in solar radius ($R_\odot$), θ is the angular position of the feature in degree. $\langle\rangle$ values represents the averaged ones. The data used for the low cadence analysis is highlighted in blue.

$time$	d	θ	d	θ	d	θ	$\langle d\rangle$	$\langle\theta\rangle$
23:16:21	1.06	238.86	1.06	238.94	1.05	238.95	1.06 ± 0.01	238.92 ± 0.05
23:20:20	1.06	238.98	1.06	238.78	1.06	238.74	1.060 ± 0.008	238.8 ± 0.1
23:26:20	1.07	239.03	1.07	238.79	1.07	238.64	1.070 ± 0.008	238.8 ± 0.2
23:30:20	1.09	238.84	1.09	238.60	1.09	238.67	1.090 ± 0.008	238.7 ± 0.1
23:36:20	1.13	238.95	1.13	238.69	1.14	238.76	1.13 ± 0.01	238.8 ± 0.1
23:40:20	1.16	239.11	1.16	238.71	1.16	238.71	1.160 ± 0.008	238.8 ± 0.2
23:46:20	1.21	239.70	1.21	239.16	1.21	239.16	1.210 ± 0.008	239.3 ± 0.3
23:50:20	1.25	239.73	1.25	239.49	1.25	239.63	1.250 ± 0.008	239.6 ± 0.1
23:56:20	1.31	240.21	1.31	240.16	1.3	240.12	1.307 ± 0.010	240.16 ± 0.05

Table 4.9: Event 3 Raw data and averaged values. For different times, d is the distance of the feature from the centre of the Sun in solar radius ($R_\odot$), θ is the angular position of the feature in degree. $\langle\rangle$ values represents the averaged ones.

time	d	θ	d	θ	d	θ	$\langle d \rangle$	$\langle \theta \rangle$	
00:30:20	1.09	232.56	1.08	232.75	1.06	232.84	1.08 ± 0.02	1.09 ± 0.04	232.7 ± 0.1
00:34:20	1.09	232.64	1.08	233.25	1.07	232.83	1.08 ± 0.01	1.09 ± 0.02	232.9 ± 0.3
00:36:20	1.10	233.01	1.09	233.78	1.07	233.20	1.09 ± 0.02	1.10 ± 0.03	233.3 ± 0.4
00:40:20	1.11	232.72	1.09	234.11	1.06	233.71	1.09 ± 0.03	1.11 ± 0.03	233.5 ± 0.7
00:44:20	1.12	233.04	1.11	234.27	1.09	234.11	1.11 ± 0.02	1.13 ± 0.07	233.8 ± 0.7
00:46:20	1.11	233.23	1.13	234.02	1.09	234.45	1.11 ± 0.02	1.13 ± 0.02	233.9 ± 0.6
00:50:20	1.14	234.47	1.13	235.14	1.10	234.72	1.12 ± 0.02	1.15 ± 0.05	234.8 ± 0.3
00:54:20	1.14	234.80	1.13	236.54	1.12	234.92	1.13 ± 0.01	1.17 ± 0.03	235 ± 1
00:56:20	1.14	235.96	1.15	236.53	1.13	235.90	1.14 ± 0.01	1.18 ± 0.04	236.1 ± 0.3
01:00:20	1.18	237.62	1.18	237.57	1.15	236.91	1.17 ± 0.02	1.22 ± 0.10	237.4 ± 0.4
01:04:20	1.21	237.28	1.20	237.57	1.17	237.06	1.19 ± 0.02	1.25 ± 0.08	237.3 ± 0.3
01:06:20	1.21	238.34	1.21	238.35	1.19	238.11	1.20 ± 0.02	1.27 ± 0.04	238.3 ± 0.1
01:10:20	1.25	239.63	1.23	239.20	1.21	238.58	1.23 ± 0.02	1.30 ± 0.10	239.1 ± 0.5
01:14:20	1.26	240.63	1.28	240.62	1.25	240.15	1.26 ± 0.02	1.35 ± 0.13	240.5 ± 0.3
01:16:20	1.28	240.86	1.29	240.92	1.27	240.69	1.28 ± 0.01	1.36 ± 0.07	240.8 ± 0.1
01:20:20	1.31	241.09	1.31	241.28	1.28	240.88	1.30 ± 0.02	1.38 ± 0.08	241.1 ± 0.2
01:24:20	1.34	241.10	1.33	241.34	1.31	241.18	1.33 ± 0.02	1.41 ± 0.11	241.2 ± 0.1
01:26:20	1.34	241.25	1.34	241.59	1.33	241.29	1.34 ± 0.01	1.42 ± 0.04	241.4 ± 0.2
01:30:20	1.36	241.90	1.37	241.85	1.34	241.17	1.36 ± 0.02	1.44 ± 0.08	241.6 ± 0.4
01:34:20	1.37	242.88	1.38	242.45	1.36	241.89	1.37 ± 0.01	1.47 ± 0.06	242.4 ± 0.5
01:36:20	1.39	242.89	1.39	243.19	1.38	242.60	1.39 ± 0.01	1.49 ± 0.07	242.9 ± 0.3
01:40:20	1.43	243.71	1.43	243.73	1.39	242.74	1.42 ± 0.03	1.52 ± 0.13	243.4 ± 0.6
01:44:20	1.46	243.96	1.45	244.08	1.43	243.84	1.45 ± 0.02	1.55 ± 0.13	244.0 ± 0.1
01:46:20	1.47	244.07	1.45	244.21	1.45	244.04	1.46 ± 0.02	1.56 ± 0.05	244.1 ± 0.1
01:50:20	1.49	244.80	1.46	244.94	1.45	244.26	1.47 ± 0.02	1.58 ± 0.05	244.7 ± 0.4
01:54:20	1.51	245.22	1.50	245.14	1.48	244.84	1.50 ± 0.02	1.61 ± 0.14	245.1 ± 0.2
01:56:20	1.52	245.37	1.51	245.46	1.50	245.31	1.51 ± 0.01	1.63 ± 0.06	245.4 ± 0.1
02:00:20	1.54	245.94	1.54	245.89	1.50	245.63	1.53 ± 0.03	1.65 ± 0.08	245.8 ± 0.2
02:04:20	1.56	246.33	1.55	246.63	1.52	246.09	1.54 ± 0.02	1.67 ± 0.08	246.4 ± 0.3
02:06:20	1.58	246.07	1.56	246.60	1.55	246.51	1.56 ± 0.02	1.69 ± 0.10	246.4 ± 0.3
02:10:20	1.56	247.15	1.56	247.12	1.56	246.55	1.56 ± 0.01	1.70 ± 0.02	246.9 ± 0.3
02:14:20	1.59	247.23	1.60	247.39	1.57	247.00	1.59 ± 0.02	1.73 ± 0.13	247.2 ± 0.2
02:16:20	1.61	247.42	1.61	247.55	1.61	247.12	1.61 ± 0.01	1.76 ± 0.12	247.4 ± 0.2
02:20:20	1.63	247.71	1.63	247.87	1.62	247.07	1.63 ± 0.01	1.77 ± 0.08	247.6 ± 0.4
02:24:20	1.65	247.71	1.64	248.06	1.65	247.81	1.65 ± 0.01	1.80 ± 0.10	247.9 ± 0.2
02:26:20	1.68	247.35	1.65	248.38	1.67	247.69	1.67 ± 0.02	1.82 ± 0.10	247.8 ± 0.5
02:30:20	1.70	247.73	1.68	248.50	1.69	248.07	1.69 ± 0.01	1.84 ± 0.12	248.1 ± 0.4

Table 4.10: EVENT 4 RAW DATA AND AVERAGED VALUES. For different times, d is the distance of the feature from the centre of the Sun in solar radius ($R_\odot$), and θ is the angular position of the feature in degree. $\langle \rangle$ values represents the averaged ones. The data used for the low cadence analysis is highlighted in blue.

time	d	θ	d	θ	d	θ	$\langle d\rangle$	$\langle\theta\rangle$
02:10:20	1.01	263.28	1.01	263.27	1.01	263.28	1.010 ± 0.008	263.277 ± 0.006
02:14:20	1.11	267.49	1.11	267.50	1.11	267.47	1.110 ± 0.008	267.49 ± 0.02
02:16:20	1.16	269.67	1.17	269.67	1.17	269.60	1.17 ± 0.01	269.65 ± 0.04
02:20:20	1.25	270.64	1.25	270.83	1.25	270.77	1.250 ± 0.008	270.75 ± 0.10
02:24:20	1.28	270.46	1.28	270.44	1.28	270.46	1.280 ± 0.008	270.45 ± 0.01
02:26:20	1.29	270.93	1.29	270.92	1.29	270.99	1.290 ± 0.008	270.95 ± 0.04
02:30:20	1.33	271.67	1.33	271.67	1.33	271.79	1.330 ± 0.008	271.71 ± 0.07
02:34:20	1.37	271.91	1.37	271.89	1.37	271.90	1.370 ± 0.008	271.90 ± 0.01
02:36:20	1.42	272.23	1.41	272.05	1.42	272.23	1.42 ± 0.01	272.2 ± 0.1
02:40:20	1.44	272.19	1.45	272.35	1.44	272.19	1.44 ± 0.01	272.24 ± 0.09
02:44:20	1.53	272.95	1.53	272.95	1.53	272.96	1.530 ± 0.008	272.953 ± 0.006
02:46:20	1.57	273.39	1.55	273.26	1.56	273.35	1.56 ± 0.01	273.33 ± 0.07
02:50:20	1.66	274.73	1.65	274.79	1.65	274.58	1.65 ± 0.01	274.7 ± 0.1
02:54:20	1.73	275.92	1.73	275.91	1.73	275.92	1.730 ± 0.008	275.917 ± 0.006
02:56:20	1.75	276.55	1.76	276.71	1.74	276.50	1.75 ± 0.01	276.6 ± 0.1
03:00:20	1.79	277.34	1.85	278.03	1.84	278.00	1.83 ± 0.03	277.8 ± 0.4
03:04:20	1.90	279.08	1.90	279.05	1.90	279.08	1.900 ± 0.008	279.07 ± 0.02
03:06:20	1.92	279.48	1.92	279.56	1.92	279.64	1.920 ± 0.008	279.56 ± 0.08
03:10:20	1.93	280.03	1.95	280.20	1.94	280.22	1.94 ± 0.01	280.2 ± 0.1
03:14:20	2.00	281.02	2.00	281.04	2.00	281.00	2.000 ± 0.008	281.02 ± 0.02
03:16:20	2.01	281.05	2.02	281.15	2.01	281.09	2.01 ± 0.01	281.10 ± 0.05
03:20:20	2.01	281.38	2.04	281.62	2.04	281.64	2.03 ± 0.02	281.5 ± 0.1

Table 4.11: Event 5 Raw data and averaged values. For different times, d is the distance of the feature from the centre of the Sun in solar radius ($R_\odot$), θ is the angular position of the feature in degree. $\langle\rangle$ values represents the averaged ones.

time	d	θ	d	θ	d	θ	$\langle d\rangle$	$\langle\theta\rangle$
21:00:25	1.07	308.36	1.07	308.86	1.07	308.75	1.070 ± 0.008	308.7 ± 0.3
21:06:25	1.08	308.43	1.08	308.91	1.08	309.08	1.080 ± 0.008	308.8 ± 0.3
21:12:25	1.09	308.67	1.09	308.76	1.09	308.93	1.090 ± 0.008	308.8 ± 0.1
21:18:25	1.10	308.50	1.1	308.99	1.09	308.97	1.10 ± 0.01	308.8 ± 0.3
21:24:25	1.10	308.88	1.1	308.82	1.1	309.29	1.100 ± 0.008	309.0 ± 0.3
21:30:25	1.11	308.88	1.11	309.26	1.11	309.26	1.110 ± 0.008	309.1 ± 0.2
21:36:25	1.13	309.15	1.13	309.06	1.13	309.15	1.130 ± 0.008	309.1 ± 0.1
21:42:25	1.17	309.71	1.16	309.33	1.16	308.87	1.16 ± 0.01	309.3 ± 0.4
21:48:25	1.22	309.44	1.22	309.78	1.22	309.36	1.220 ± 0.008	309.5 ± 0.2
21:54:25	1.30	309.94	1.3	310.51	1.32	309.59	1.31 ± 0.01	310.0 ± 0.5
22:00:25	1.40	310.44	1.4	310.30	1.41	310.54	1.40 ± 0.01	310.4 ± 0.1
22:06:25	1.49	311.00	1.49	310.81	1.47	311.02	1.48 ± 0.01	310.9 ± 0.1

Table 4.12: Event 6 Raw data and averaged values. For different times, d is the distance of the feature from the centre of the Sun in solar radius ($R_\odot$), θ is the angular position of the feature in degree. $\langle\rangle$ values represents the averaged ones.

The chi square distribution

Below, the critical values associated with the chi-square variable for various degrees of freedom are shown. Specifically, these values are linked to significance levels ranging from 0.4 to 0.001. Refer to Section 3.4.3 for more details.

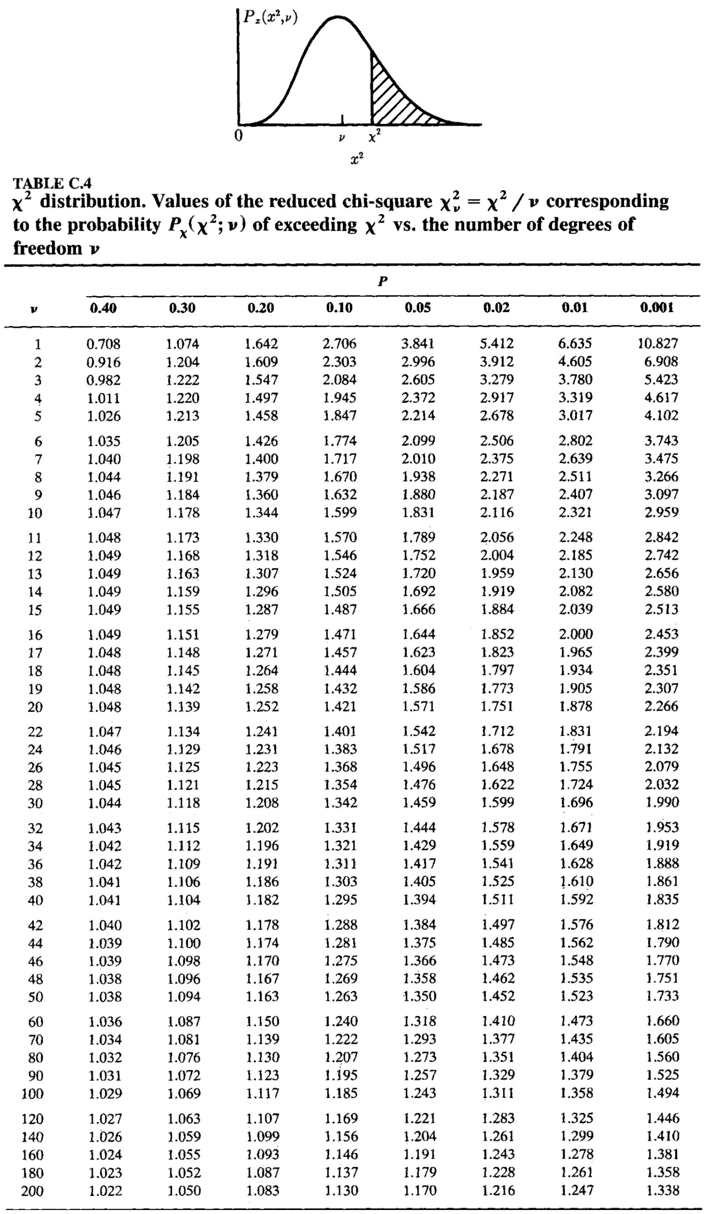

TABLE C.4
χ^2 distribution. Values of the reduced chi-square $\chi^2_\nu = \chi^2/\nu$ corresponding to the probability $P_\chi(\chi^2;\nu)$ of exceeding χ^2 vs. the number of degrees of freedom ν

	P							
ν	0.40	0.30	0.20	0.10	0.05	0.02	0.01	0.001
1	0.708	1.074	1.642	2.706	3.841	5.412	6.635	10.827
2	0.916	1.204	1.609	2.303	2.996	3.912	4.605	6.908
3	0.982	1.222	1.547	2.084	2.605	3.279	3.780	5.423
4	1.011	1.220	1.497	1.945	2.372	2.917	3.319	4.617
5	1.026	1.213	1.458	1.847	2.214	2.678	3.017	4.102
6	1.035	1.205	1.426	1.774	2.099	2.506	2.802	3.743
7	1.040	1.198	1.400	1.717	2.010	2.375	2.639	3.475
8	1.044	1.191	1.379	1.670	1.938	2.271	2.511	3.266
9	1.046	1.184	1.360	1.632	1.880	2.187	2.407	3.097
10	1.047	1.178	1.344	1.599	1.831	2.116	2.321	2.959
11	1.048	1.173	1.330	1.570	1.789	2.056	2.248	2.842
12	1.049	1.168	1.318	1.546	1.752	2.004	2.185	2.742
13	1.049	1.163	1.307	1.524	1.720	1.959	2.130	2.656
14	1.049	1.159	1.296	1.505	1.692	1.919	2.082	2.580
15	1.049	1.155	1.287	1.487	1.666	1.884	2.039	2.513
16	1.049	1.151	1.279	1.471	1.644	1.852	2.000	2.453
17	1.048	1.148	1.271	1.457	1.623	1.823	1.965	2.399
18	1.048	1.145	1.264	1.444	1.604	1.797	1.934	2.351
19	1.048	1.142	1.258	1.432	1.586	1.773	1.905	2.307
20	1.048	1.139	1.252	1.421	1.571	1.751	1.878	2.266
22	1.047	1.134	1.241	1.401	1.542	1.712	1.831	2.194
24	1.046	1.129	1.231	1.383	1.517	1.678	1.791	2.132
26	1.045	1.125	1.223	1.368	1.496	1.648	1.755	2.079
28	1.045	1.121	1.215	1.354	1.476	1.622	1.724	2.032
30	1.044	1.118	1.208	1.342	1.459	1.599	1.696	1.990
32	1.043	1.115	1.202	1.331	1.444	1.578	1.671	1.953
34	1.042	1.112	1.196	1.321	1.429	1.559	1.649	1.919
36	1.042	1.109	1.191	1.311	1.417	1.541	1.628	1.888
38	1.041	1.106	1.186	1.303	1.405	1.525	1.610	1.861
40	1.041	1.104	1.182	1.295	1.394	1.511	1.592	1.835
42	1.040	1.102	1.178	1.288	1.384	1.497	1.576	1.812
44	1.039	1.100	1.174	1.281	1.375	1.485	1.562	1.790
46	1.039	1.098	1.170	1.275	1.366	1.473	1.548	1.770
48	1.038	1.096	1.167	1.269	1.358	1.462	1.535	1.751
50	1.038	1.094	1.163	1.263	1.350	1.452	1.523	1.733
60	1.036	1.087	1.150	1.240	1.318	1.410	1.473	1.660
70	1.034	1.081	1.139	1.222	1.293	1.377	1.435	1.605
80	1.032	1.076	1.130	1.207	1.273	1.351	1.404	1.560
90	1.031	1.072	1.123	1.195	1.257	1.329	1.379	1.525
100	1.029	1.069	1.117	1.185	1.243	1.311	1.358	1.494
120	1.027	1.063	1.107	1.169	1.221	1.283	1.325	1.446
140	1.026	1.059	1.099	1.156	1.204	1.261	1.299	1.410
160	1.024	1.055	1.093	1.146	1.191	1.243	1.278	1.381
180	1.023	1.052	1.087	1.137	1.179	1.228	1.261	1.358
200	1.022	1.050	1.083	1.130	1.170	1.216	1.247	1.338

Figure 4.48: THE CHI SQUARE DISTRIBUTION. χ^2_ν are the values of the reduced chi-square, *df* the degrees of freedom, P the probability of exceeding the corresponding chi value. In this work the confidence level is set at 0.05. See Section 3.4.3 for more details. Imaged adapted from didattica INFN [67]

Bibliography

[1] A. Alexandrova, S. A. (No date). In situ evidence of firehose instability in multiple magnetic reconnection. https://presentations.copernicus.org/EGU2020/EGU2020-18188_presentation.pdf.

[2] Academy, S. (2012). Introductory statistics:chi-square tests and f-tests. https://saylordotorg.github.io/text_introductory-statistics/s15-chi-square-tests-and-f-tests.html.

[3] Alfvén, H. (1942). Existence of electromagnetic-hydrodynamic waves. *Nature*, 150(3805):405–406.

[4] Aly, J. (1991). How much energy can be stored in a three-dimensional force-free magnetic field? *Astrophysical Journal, Part 2-Letters (ISSN 0004-637X), vol. 375, July 10, 1991, p. L61-L64.*, 375:L61–L64.

[5] Aly, J. J. (1990). Quasi-static evolution of a force-free magnetic field. *Computer Physics Communications*, 59(1):13–20.

[6] Amari, T., Luciani, J., Aly, J., Mikic, Z., and Linker, J. (2003). Coronal mass ejection: initiation, magnetic helicity, and flux ropes. ii. turbulent diffusion-driven evolution. *The Astrophysical Journal*, 595(2):1231.

[7] Antiochos, S., Dahlburg, R., and Klimchuk, J. (1994). The magnetic field of solar prominences. *Astrophysical Journal, Part 2-Letters (ISSN 0004-637X), vol. 420, no. 1, p. L41-L44*, 420:L41–L44.

[8] Antiochos, S., DeVore, C., and Klimchuk, J. (1999). A model for solar coronal mass ejections. *The Astrophysical Journal*, 510(1):485.

[9] Aschwanden, M., Wuelser, J., Nitta, N., and Lemen, J. (2009). Solar flare and cme observations with stereo/euvi. *Solar Physics*, 256:3–40.

[10] Aulanier, G. and Démoulin, P. (1998). 3-d magnetic configurations supporting prominences. i. the natural presence of lateral feet. *Astronomy and Astrophysics, v. 329, p. 1125-1137 (1998)*, 329:1125–1137.

[11] Aulanier, G., DeVore, C. R., and Antiochos, S. K. (2006). Solar prominence merging. *The Astrophysical Journal*, 646(2):1349.

[12] Ballester, J. L. (2006). Seismology of prominence-fine structures: Observations and theory. *Space science reviews*, 122:129–135.

[13] Barnes, C. and Sturrock, P. (1972). Force-free magnetic-field structures and their role in solar activity. *Astrophysical Journal, vol. 174, p. 659*, 174:659.

[14] Bateman, M. (1978). Instabilities mit press. *Cambridge, Massachusetts.*

[15] Bertolucci, S., Zioutas, K., Hofmann, S., and Maroudas, M. (2017). The sun and its planets as detectors for invisible matter. *Physics of the dark universe*, 17:13–21.

[16] Brueckner, G., Howard, R., Koomen, M., Korendyke, C., Michels, D., Moses, J., Socker, D., Dere, K., Lamy, P., Llebaria, A., et al. (1995). The large angle spectroscopic coronagraph (lasco) visible light coronal imaging and spectroscopy. *The SOHO mission*, pages 357–402.

[17] Brueckner, G. E., Howard, R. A., Koomen, M. J., Korendyke, C. M., Michels, D. J., Moses, J. D., Socker, D. G., Dere, K. P., Lamy, P. L., Llebaria, A., Bout, M. V., Schwenn, R., Simnett, G. M., Bedford, D. K., and Eyles, C. J. (1995). The Large Angle Spectroscopic Coronagraph (LASCO). *Solar Physics*, 162(1-2):357–402.

[18] Byrne, J., Long, D., Gallagher, P., Bloomfield, D., Maloney, S., McAteer, R., Morgan, H., and Habbal, S. R. (2013). Improved methods for determining the kinematics of coronal mass ejections and coronal waves. *Astronomy & Astrophysics*, 557:A96.

[19] Cécere, M., Sieyra, M. V., Cremades, H., Mierla, M., Sahade, A., Stenborg, G., Costa, A., West, M., and D'Huys, E. (2020). Large non-radial propagation of a coronal mass ejection on 2011 january 24. *Advances in Space Research*, 65(6):1654–1662.

[20] Chae, J. (2001). Observational determination of the rate of magnetic helicity transport through the solar surface via the horizontal motion of field line footpoints. *The Astrophysical Journal*, 560(1):L95.

[21] Chen, J. (1989). Effects of Toroidal Forces in Current Loops Embedded in a Background Plasma. *The Astrophysical Journal*, 338:453.

[22] Chen, P. (2011). Coronal mass ejections: models and their observational basis. *Living Reviews in Solar Physics*, 8(1):1–92.

[23] Cheng, J.-X., Fang, C., Chen, P.-F., and Ding, M.-D. (2005). Two sympathetic homologous cmes on 2002 may 22. *Chinese Journal of Astronomy and Astrophysics*, 5(3):265.

[24] Cheng, X., Zhang, J., Kliem, B., Török, T., Xing, C., Zhou, Z., Inhester, B., and Ding, M. (2020). Initiation and early kinematic evolution of solar eruptions. *The Astrophysical Journal*, 894(2):85.

[25] Chitta, L., Zhukov, A., Berghmans, D., Peter, H., Parenti, S., Mandal, S., Aznar Cuadrado, R., Schühle, U., Teriaca, L., Auchère, F., et al. (2023). Picoflare jets power the solar wind emerging from a coronal hole on the sun. *Science*, 381(6660):867–872.

[26] Chouduri, A. R. (1998). *The Physics of Fluids and Plasmas. An Introduction for Astrophysicists.* Cambridge University Press.

[27] Cremades, H., Bothmer, V., and Tripathi, D. (2006). Properties of structured coronal mass ejections in solar cycle 23. *Advances in Space Research*, 38(3):461–465.

[28] de la Cruz Rodriguez, J. and Socas-Navarro, H. (2011). Are solar chromospheric fibrils tracing the magnetic field? *Astronomy & Astrophysics*, 527:L8.

[29] Delaboudiniere, J.-P., Artzner, G., Brunaud, J., Gabriel, A. H., Hochedez, J.-F., Millier, F., Song, X., Au, B., Dere, K., Howard, R. A., et al. (1995). Eit: extreme-ultraviolet imaging telescope for the soho mission. *The SOHO Mission*, pages 291–312.

[30] DeVore, C. R. and Antiochos, S. K. (2000). Dynamical formation and stability of helical prominence magnetic fields. *The Astrophysical Journal*, 539(2):954.

[31] D'Huys, E., Seaton, D., Poedts, S., and Berghmans, D. (2014). Observational characteristics of coronal mass ejections without low-coronal signatures. *The Astrophysical Journal*, 795(1):49.

[32] ESA (No date). The structure of the suns. cesar's booklet.

[33] Eto, S., Isobe, H., Narukage, N., Asai, A., Morimoto, T., Thompson, B., Yashiro, S., Wang, T., Kitai, R., Kurokawa, H., et al. (2002). Relation between a moreton wave and an eit wave observed on 1997 november 4. *Publications of the Astronomical Society of Japan*, 54(3):481–491.

[34] Fan, Y. and Gibson, S. (2006). On the nature of the x-ray bright core in a stable filament channel. *The Astrophysical Journal*, 641(2):L149.

[35] Fan, Y. and Gibson, S. (2007). Onset of coronal mass ejections due to loss of confinement of coronal flux ropes. *The Astrophysical Journal*, 668(2):1232.

[36] Fan, Y. and Low, B. (2003). Dynamics of cme driven by a buoyant prominence flux tube. In *Current Theoretical Models and Future High Resolution Solar Observations: Preparing for ATST*, volume 286, page 347.

[37] Filippov, B. and Koutchmy, S. (2008). Causal relationships between eruptive prominences and coronal mass ejections. *Annales Geophysicae*, 26(10):3025–3031.

[38] Forbes, T. (2000). A review on the genesis of coronal mass ejections. *Journal of Geophysical Research: Space Physics*, 105(A10):23153–23165.

[39] Forbes, T., Linker, J., Chen, J., Cid, C., Kóta, J., Lee, M., Mann, G., Mikić, Z., Potgieter, M., Schmidt, J., et al. (2006). Cme theory and models: Report of working group d. *Space Science Reviews*, 123:251–302.

[40] Forbes, T. and Priest, E. (1995). Photospheric magnetic field evolution and eruptive flares. *The Astrophysical Journal*, 446:377.

[41] Forbes, T., Priest, E., and Isenberg, P. (1994). On the maximum energy release in flux-rope models of eruptive flares. *Solar physics*, 150:245–266.

[42] Fu-gang, L. and Jian, W. (2013). Relations of the planets revolution, sun tidal force and gravitation deriving from the planets with the solar activity periodicity. *Progress in Geophysics*, 28(5):2229–2240.

[43] Gold, T. and Hoyle, F. (1960). On the origin of solar flares. *Monthly Notices of the Royal Astronomical Society*, 120(2):89–105.

[44] Gopalswamy, N., Mäkelä, P., Xie, H., Akiyama, S., and Yashiro, S. (2009). Cme interactions with coronal holes and their interplanetary consequences. *Journal of Geophysical Research: Space Physics*, 114(A3).

[45] Gopalswamy, N., Shimojo, M., Lu, W., Yashiro, S., Shibasaki, K., and Howard, R. (2003). Prominence eruptions and coronal mass ejection: a statistical study using microwave observations. *The Astrophysical Journal*, 586(1):562.

[46] Handy, B., Acton, L., Kankelborg, C., Wolfson, C., Akin, D., Bruner, M., Caravalho, R., Catura, R., Chevalier, R., Duncan, D., et al. (1999). The transition region and coronal explorer. *Solar Physics*, 187:229–260.

[47] Hood, A. and Priest, E. (1981). Critical conditions for magnetic instabilities in force-free coronal loops. *Geophysical & Astrophysical Fluid Dynamics*, 17(1):297–318.

[48] House, L., Wagner, W., Hildner, E., Sawyer, C., and Schmidt, H. (1981). Studies of the corona with the solar maximum mission coronagraph/polarimeter. *The Astrophysical Journal*, 244:L117–L121.

[49] Howard, R. A., Moses, J., Vourlidas, A., Newmark, J., Socker, D. G., Plunkett, S. P., Korendyke, C. M., Cook, J., Hurley, A., Davila, J., et al. (2008). Sun earth connection coronal and heliospheric investigation (secchi). *Space Science Reviews*, 136:67–115.

[50] Hung, C.-C. (2007). Apparent relations between solar activity and solar tides caused by the planets. Technical report, NASA.

[51] Ji, H., Wang, H., Schmahl, E. J., Moon, Y.-J., and Jiang, Y. (2003). Observations of the failed eruption of a filament. *The Astrophysical Journal*, 595(2):L135.

[52] Joshi, A. and Srivastava, N. (2010). Three-dimensional reconstruction of solar features using triangulation technique. *38th COSPAR Scientific Assembly*, 38:3.

[53] Joshi, V. and Srivastava, N. (2007). On the study of kinematics of eruptive quiescent prominences observed in he 304 å. *Bull. Astron. Soc. India*, 35:447–455.

[54] Kahler, S., Moore, R., Kane, S., and Zirin, H. (1988). Filament eruptions and the impulsive phase of solar flares. *Astrophysical Journal, Part 1 (ISSN 0004-637X), vol. 328, May 15, 1988, p. 824-829.*, 328:824–829.

[55] Kay, C., Opher, M., and Evans, R. (2015). Global trends of cme deflections based on cme and solar parameters. *The Astrophysical Journal*, 805(2):168.

[56] Kippenhahn, R. and Schlüter, A. (1957). Eine theorie der solaren filamente. mit 7 textabbildungen. *Zeitschrift für Astrophysik, Vol. 43, p. 36*, 43:36.

[57] Kliem, B. and Török, T. (2006). Torus instability. *Physical Review Letters*, 96(25):255002.

[58] Kumar, P. and Cho, K.-S. (2013). Simultaneous euv and radio observations of bidirectional plasmoids ejection during magnetic reconnection. *Astronomy & Astrophysics*, 557:A115.

[59] Kuperus, M. and Raadu, M. A. (1974). The support of prominences formed in neutral sheets. *Astronomy and Astrophysics, Vol. 31, p. 189 (1974)*, 31:189.

[60] Labrosse, N. and McGlinchey, K. (2012). Plasma diagnostic in eruptive prominences from sdo/aia observations at 304 å. *Astronomy & Astrophysics*, 537:A100.

[61] Lang, K. R. (2008). *The Sun from space.* Springer Science & Business Media.

[62] Lemen, J. R., Title, A. M., Akin, D. J., Boerner, P. F., Chou, C., Drake, J. F., Duncan, D. W., Edwards, C. G., Friedlaender, F. M., Heyman, G. F., et al. (2012). The atmospheric imaging assembly (aia) on the solar dynamics observatory (sdo). *Solar Physics*, 275:17–40.

[63] Liewer, P., Panasenco, O., Vourlidas, A., and Colaninno, R. (2015). Observations and analysis of the non-radial propagation of coronal mass ejections near the sun. *Solar Physics*, 290:3343–3364.

[64] Lin, J., Ko, Y.-K., Sui, L., Raymond, J., Stenborg, G., Jiang, Y., Zhao, S., and Mancuso, S. (2005). Direct observations of the magnetic reconnection site of an eruption on 2003 november 18. *The Astrophysical Journal*, 622(2):1251.

[65] Liu, T. and Su, Y. (2021). Tether-cutting and overlying magnetic reconnections in an mhd simulation of prominence-cavity system. *The Astrophysical Journal*, 915(1):55.

[66] Low, B. (1994). Magnetohydrodynamic processes in the solar corona: Flares, coronal mass ejections, and magnetic helicity. *Physics of Plasmas*, 1(5):1684–1690.

[67] Lunardon, M. (No date). Tavolechi2. https://userswww.pd.infn.it/ lunardon/didattica/docsper2/-TavoleChi2.pdf.

[68] Lynch, B., Antiochos, S., MacNeice, P., Zurbuchen, T., and Fisk, L. (2004). Observable properties of the breakout model for coronal mass ejections. *The Astrophysical Journal*, 617(1):589.

[69] Mackay, D., Karpen, J., Ballester, J., Schmieder, B., and Aulanier, G. (2010). Physics of solar prominences: Ii—magnetic structure and dynamics. *Space Science Reviews*, 151:333–399.

[70] Majumdar, S., Pant, V., Patel, R., and Banerjee, D. (2020). Connecting 3d evolution of coronal mass ejections to their source regions. *The Astrophysical Journal*, 899(1):6.

[71] Martens, P. and Kuin, N. (1989). A circuit model for filament eruptions and two-ribbon flares. *Solar physics*, 122:263–302.

[72] McKenzie, D. E. and Savage, S. L. (2011). Distribution functions of sizes and fluxes determined from supra-arcade downflows. *The Astrophysical Journal Letters*, 735(1):L6.

[73] Mierla, M., Cremades, H., Andretta, V., Chifu, I., Zhukov, A. N., Susino, R., Auchère, F., Vourlidas, A., Talpeanu, D.-C., Rodriguez, L., et al. (2023). Three eruptions observed by remote sensing instruments onboard solar orbiter. *Solar Physics*, 298(3):42.

[74] Mierla, M., Seaton, D., Berghmans, D., Chifu, I., De Groof, A., Inhester, B., Rodriguez, L., Stenborg, G., and Zhukov, A. (2013). Study of a prominence eruption using proba2/swap and stereo/euvi data. *Solar Physics*, 286:241–253.

[75] Moore, R. L. (1988). Evidence that magnetic energy shedding in solar filament eruptions is the drive in accompanying flares and coronal mass ejections. *The Astrophysical journal*, 324:1132–1137.

[76] Moore, R. L. and Roumeliotis, G. (1992). Triggering of Eruptive Flares - Destabilization of the Preflare Magnetic Field Configuration. In Svestka, Z., Jackson, B. V., and Machado, M. E., editors, *IAU Colloq. 133: Eruptive Solar Flares*, volume 399, page 69.

[77] Möstl, C., Rollett, T., Frahm, R. A., Liu, Y. D., Long, D. M., Colaninno, R. C., Reiss, M. A., Temmer, M., Farrugia, C. J., Posner, A., et al. (2015). Strong coronal channelling and interplanetary evolution of a solar storm up to earth and mars. *Nature Communications*, 6(1):7135.

[78] Müller, D., Cyr, O. S., Zouganelis, I., Gilbert, H. R., Marsden, R., Nieves-Chinchilla, T., Antonucci, E., Auchère, F., Berghmans, D., Horbury, T., et al. (2020). The solar orbiter mission-science overview. *Astronomy & Astrophysics*, 642:A1.

[79] Müller, D., Nicula, B., Felix, S., Verstringe, F., Bourgoignie, B., Csillaghy, A., Berghmans, D., Jiggens, P., García-Ortiz, J., Ireland, J., et al. (2017). Jhelioviewer-time-dependent 3d visualisation of solar and heliospheric data. *Astronomy & Astrophysics*, 606:A10.

[80] NASA (No date). The heliospheric current sheet.

[81] NSO (No date). Virtual solar observatoy. https://docs.virtualsolar.org/.

[82] NSO/GONG (No date). Potential-field source-surface models for the global coronal magnetic field. https://gong.nso.edu/science/gongpfss/gongpfss.html.

[83] Okamoto, T. J., Nakai, H., Keiyama, A., Narukage, N., UeNo, S., Kitai, R., Kurokawa, H., and Shibata, K. (2004). Filament oscillations and moreton waves associated with eit waves. *The Astrophysical Journal*, 608(2):1124.

[84] Panasenco, O. and Velli, M. (2013). Coronal pseudostreamers: Source of fast or slow solar wind? In *AIP Conference Proceedings*, volume 1539, pages 50–53. American Institute of Physics.

[85] Parenti, S. (2014). Solar prominences: observations. *Living Reviews in Solar Physics*, 11:1–88.

[86] Patel, R., Pant, V., Chandrashekhar, K., and Banerjee, D. (2020). A statistical study of plasmoids associated with a post-cme current sheet. *Astronomy & Astrophysics*, 644:A158.

[87] Patsourakos, S., Vourlidas, A., and Török, T. (2020). Decoding the pre-eruptive magnetic field configurations of coronal mass ejections. *Space Sci Rev*, 216:131.

[88] Petrakou, E. (2021). Planetary statistics and forecasting for solar flares. *Advances in Space Research*, 68(7):2963–2973.

[89] Pettit, E. (1932). Characteristic features of solar prominences. *Astrophysical Journal, vol. 76, p. 9*, 76:9.

[90] Pneuman, G. (1981). Two-ribbon flares-/post/-flare loops. *Solar Flare Magnetohydrodynamics*, pages 379–428.

[91] Pneuman, G. (1983). The formation of solar prominences by magnetic reconnection and condensation. *Solar physics*, 88:219–239.

[92] Priest, E. (2007). *"Solar Atmosphere", in Handbook of the solar-terrestrial environment by Kamide, Yohsuke and Chian, Abraham*. Springer.

[93] Priest, E. and Forbes, T. (1990). Magnetic field evolution during prominence eruptions and two-ribbon flares. *Solar Physics*, 126:319–350.

[94] Priest, E. and Forbes, T. (2002). The astron. astrophys. *Rev*, 10:313.

[95] Priest, E., Hood, A., and Anzer, U. (1989). A twisted flux-tube model for solar prominences. i-general properties. *The Astrophysical Journal*, 344:1010–1025.

[96] Raouafi, N. E., Stenborg, G., Seaton, D. B., Wang, H., Wang, J., DeForest, C. E., Bale, S. D., Drake, J. F., Uritsky, V. M., Karpen, J. T., et al. (2023). Magnetic reconnection as the driver of the solar wind. *The Astrophysical Journal*, 945(1):28.

[97] Rochus, P., Halain, J.-P., Renotte, E., Berghmans, D., Zhukov, A., Hochedez, J.-F., Appourchaux, T., Auchère, F., Harra, L., Schühle, U., et al. (2009). The extreme ultraviolet imager (eui) onboard the solar orbiter mission. In *60th International Astronautical Congress*.

[98] Rochus, P., Auchère, F., Berghmans, D., Harra, L., Schmutz, W., and et al., S. (2020). The solar orbiter eui instrument: The extreme ultraviolet imager. *A&A*, 642.

[99] Roudier, T., Schmieder, B., Filippov, B., Chandra, R., and Malherbe, J.-M. (2018). Horizontal photospheric flows trigger a filament eruption. *Astronomy & Astrophysics*, 618:A43.

[100] Rouillard, A. P., Pinto, R., Vourlidas, A., De Groof, A., Thompson, W., Bemporad, A., Dolei, S., Indurain, M., Buchlin, E., Sasso, C., et al. (2020). Models and data analysis tools for the solar orbiter mission. *Astronomy & Astrophysics*, 642:A2.

[101] Rust, D. and Kumar, A. (1994). Helical magnetic fields in filaments. *Solar physics*, 155:69–97.

[102] Sachdeva, N., Subramanian, P., Vourlidas, A., and Bothmer, V. (2017). Cme dynamics using stereo and lasco observations: the relative importance of lorentz forces and solar wind drag. *Solar Physics*, 292:1–17.

[103] Savage, S. L., McKenzie, D. E., Reeves, K. K., Forbes, T. G., and Longcope, D. W. (2010). Reconnection outflows and current sheet observed with hinode/xrt in the 2008 april 9 "cartwheel cme" flare. *The Astrophysical Journal*, 722(1):329.

[104] Scafetta, N. and Bianchini, A. (2022). The planetary theory of solar activity variability: a review. *Frontiers in Astronomy and Space Sciences*, 9:937930.

[105] Schrijver, C. J., Elmore, C., Kliem, B., Török, T., et al. (2008). Observations and modeling of the early acceleration phase of erupting filaments involved in coronal mass ejections. *The Astrophysical Journal*, 674(1):586.

[106] Schuster, A. (1911). The influence of planets on the formation of sun-spots. *Proceedings of the Royal Society of London. Series A, Containing Papers of a Mathematical and Physical Character*, 85(579):309–323.

[107] Seaton, D., Berghmans, D., Nicula, B., Halain, J.-P., De Groof, A., Thibert, T., Bloomfield, D., Raftery, C., Gallagher, P., Auchère, F., et al. (2013). The swap euv imaging telescope part i: instrument overview and pre-flight testing. *Solar Physics*, 286:43–65.

[108] Seaton, D. B., Mierla, M., Berghmans, D., Zhukov, A. N., and Dolla, L. (2010). Swap–secchi observations of a mass-loading type solar eruption. *The Astrophysical Journal Letters*, 727(1):L10.

[109] Secchi, A. (1877). *Le soleil.* Gauthier-Villars.

[110] Seker, I. (2013). Are planetary tides on the sun and the birthplace of sunspots related? *Solar Physics*, 286:303–314.

[111] Sieyra, M. V., Cécere, M., Cremades, H., Iglesias, F. A., Sahade, A., Mierla, M., Stenborg, G., Costa, A., West, M. J., and D'Huys, E. (2020). Analysis of large deflections of prominence–cme events during the rising phase of solar cycle 24. *Solar Physics*, 295:1–29.

[112] SKYbrary (No date). Impact of space weather on aviation. https://skybrary.aero/articles/impact-space-weather-aviation.

[113] Sturrock, P. A. (1991). Maximum Energy of Semi-infinite Magnetic Field Configurations. *The Astrophysical Journey*, 380:655.

[114] Sun, X. (No date). Notes on pfss extrapolation. http://wso.stanford.edu/words/pfss.pdf.

[115] Tandberg-Hanssen, E. (1974). *Solar Prominences*, volume 12. D. Reidel Publishing Co, Dordrecht.

[116] Taylor, J. R. and Thompson, W. (1982). *An introduction to error analysis: the study of uncertainties in physical measurements*, volume 2. Springer.

[117] Temmer, M., Rollett, T., Möstl, C., Veronig, A. M., Vršnak, B., and Odstrčil, D. (2011). Influence of the ambient solar wind flow on the propagation behavior of interplanetary coronal mass ejections. *The Astrophysical Journal*, 743(2):101.

[118] Thompson, W. T. (2006). Coordinate systems for solar image data. *Association of American Physicians*, 449(2):791–803.

[119] Titov, V. and Démoulin, P. (1999). Basic topology of twisted magnetic configurations in solar flares. *Astronomy and Astrophysics*, 351:707–720.

[120] Török, T. and Kliem, B. (2005). Confined and ejective eruptions of kink-unstable flux ropes. *The Astrophysical Journal*, 630(1):L97.

[121] Török, T., Kliem, B., and Titov, V. (2004). Ideal kink instability of a magnetic loop equilibrium. *Astronomy & Astrophysics*, 413(3):L27–L30.

[122] van Ballegooijen, A. A. and Martens, P. (1989). Formation and eruption of solar prominences. *Astrophysical Journal, Part 1 (ISSN 0004-637X), vol. 343, Aug. 15, 1989, p. 971-984.*, 343:971–984.

[123] Van Tend, W. and Kuperus, M. (1978). The development of coronal electric current systems in active regions and their relation to filaments and flares. *Solar Physics*, 59:115–127.

[124] Vashishtha, N., Majumdar, S., Patel, R., Pant, V., and Banerjee, D. (2023). Exploring the impact of imaging cadence on inferring cme kinematics. *arXiv preprint arXiv:2308.11944*.

[125] Vial, J.-C. and Engvold, O. (2015). *Solar prominences*. Springer.

[126] Wang, R., Liu, Y. D., Dai, X., Yang, Z., Huang, C., and Hu, H. (2015). The role of active region coronal magnetic field in determining coronal mass ejection propagation direction. *The Astrophysical Journal*, 814(1):80.

[127] Wang, Y. M. (2015). Pseudostreamers as the Source of a Separate Class of Solar Coronal Mass Ejections. *The Astrophysical Journal Letters*, 803(1):L12.

[128] Wu, S., Zhang, T., Tandberg-Hanssen, E., Liu, Y., Feng, X., and Tan, A. (2004). Numerical magnetohydrodynamic experiments for testing the physical mechanisms of coronal mass ejections acceleration. *Solar Physics*, 225:157–175.

[129] Wülser, J.-P., Lemen, J. R., and Nitta, N. (2007). The stereo secchi/euvi euv coronal imager. In *Solar Physics and Space Weather Instrumentation II*, volume 6689, pages 19–27. SPIE.

[130] Yang, J., Dai, J., Chen, H., Li, H., and Jiang, Y. (2018). Filament eruption with a deflection of nearly 90 degrees. *The Astrophysical Journal*, 862(1):86.

[131] Zhang, J. and Dere, K. (2006). A statistical study of main and residual accelerations of coronal mass ejections. *The Astrophysical Journal*, 649(2):1100.

[132] Zhou, G., Wang, J., Zhang, J., Chen, P., Ji, H., and Dere, K. (2006). Two successive coronal mass ejections driven by the kink and drainage instabilities of an eruptive prominence. *The Astrophysical Journal*, 651(2):1238.

[133] Zirin, H. (1988). Astrophysics of the sun. *Cambridge: University Press.*